Experimental Study and Analytical Approaches to Avoid Matrix Defects during Composites Manufacturing

by

Seyyed Mohammad Mohseni

B.A.Sc. Materials Science and Engineering, Sharif University of Technology, 2013

M.A.Sc. Mechanical Engineering, The University of British Columbia, 2015

A THESIS SUBMITTED IN PARTIAL FULFILLMENT
OF THE REQUIREMENTS FOR THE DEGREE OF

Doctor of Philosophy

in

THE FACULTY OF GRADUATE AND POSTDOCTORAL STUDIES

(Materials Engineering)

The University of British Columbia

(Vancouver)

April 2020

The following individuals certify that they have read, and recommend to the Faculty of Graduate and Postdoctoral Studies for acceptance, the thesis entitled:

Experimental Study and Analytical Approaches to Avoid Matrix Defects during Composites Manufacturing

submitted by **Seyyed Mohammad Mohseni** in partial fulfillment of the requirements for the degree of **Doctor of Philosophy** in **Materials Engineering**.

Examining Committee:

Göran Fernlund, Associate Professor, Materials Engineering, University of British Columbia
Supervisor

Daan Maijer, Professor, Materials Engineering, University of British Columbia
Supervisory Committee Member

Chad Sinclair, Professor, Materials Engineering, University of British Columbia
Supervisory Committee Member

Anoush Poursartip, Professor, Materials Engineering, University of British Columbia
University Examiner

Mark Martinez, Professor, Chemical and Biological Engineering, University of British Columbia
University Examiner

Véronique Michaud, Associate Professor, School of Engineering, École polytechnique fédérale de Lausanne
External Examiner

Abstract

Resin matrix defects are common during the manufacture of composite parts. These defects lead to rework or part rejection which ultimately lead to increased manufacturing cost. This study investigates different sources of such defects, the underlying physics, and proposes several analytical models for their mitigation. The goal of this work is to develop a comprehensive and practical analytical approach for process design to avoid matrix defects during processing.

Prior to gelation, the resin can release volatiles which may lead to porosity formation. An experimental study was conducted to investigate the conditions under which moisture dissolved in the resin lead to bubble growth and porosity. The experimental setup uses accurate temperature readings and time-lapse micrographs of bubbles. Subsequent data analysis and image processing validated the application of existing bubble dynamics models to predict the onset of moisture-induced bubble growth. These models, together with cure kinetics models for the resin, were used to develop an analytical approach to suppress moisture-driven porosity through cure cycle design (temperature and pressure).

Other sources of porosity include gas entrapment and incomplete resin infiltration. The interaction between these two mechanisms was investigated using a novel experimental design that isolates the effect of vacuum and applied pressure. Results showed that resin infiltration influences gas transport out of the laminate by reducing the available transport pathways. A fully coupled transport model was developed that explicitly includes this interaction during processing of

partially-impregnated prepregs. It was shown that the model can predict the measured porosity using material parameters from the literature.

The resin microstructure after gelation suppresses bubble growth and resin infiltration. However, continuing cure in a constrained geometry leads to internal stress development and potential defects. An experimental setup was used which allows direct observation of the resin behavior after gelation and the formation/propagation of defects. It was found that post-gelation defect formation is hydrostatic stress-driven and the defect morphology is cure rate-dependent. An analytical approach was proposed, and experimentally validated, to avoid post-gelation defects based on comprehensive material characterization and internal stress evolution calculations.

Lay summary

Carbon fiber-reinforced polymeric composites are a common material in high-performance structural applications. Their use will see continued growth as concerns about reducing weight and fuel consumption in transport applications increases.

The performance of these materials is sensitive to defects in the resin matrix. The main sources of matrix defects during processing are volatile release, entrapped gas and incomplete resin infiltration, and internal stresses.

This thesis investigates each of the mentioned defect sources, their underlying physics, proposes corresponding analytical models and their application in process design. Novel experiments were designed to evaluate the important mechanisms. Analytical and numerical models provided insight for developing approaches to prevent defect formation during processing. The developed models and approaches are components of a larger analytical approach for cure cycle design to enable defect-free part manufacturing.

Preface

This thesis presents research conducted by Seyyed Mohammad Mohseni while under the supervision of Professor Göran Fernlund at The University of British Columbia.

All experiments in Chapter 4 were designed and conducted by Seyyed Mohammad Mohseni under the supervision of Professor Göran Fernlund. Part of the experimental setup was designed and assembled by Malcolm Lane at Convergent Manufacturing Technologies. The analytical approach for suppressing moisture-driven bubble growth was developed and validated by Seyyed Mohammad Mohseni under the supervision of Professor Göran Fernlund. A paper based on this chapter has been published. **Mohseni SM**, Fernlund G, Lane M. (2018) "Cure cycle design to suppress moisture-driven bubble growth in polymer composites", *Journal of Composite Materials*. All parts of the paper were prepared and written by Seyyed Mohammad Mohseni while under the supervision of Professor Göran Fernlund. Part of the experimental setup was designed and assembled by Malcolm Lane.

All experiments in Chapter 5 were designed and conducted by Seyyed Mohammad Mohseni under the supervision of Professor Göran Fernlund. Verification repeat tests were partly conducted by co-op student Stefan Hauser while under the supervision of Seyyed Mohammad Mohseni. The fully-coupled transport model was developed, discretized, and implemented by Seyyed Mohammad Mohseni. A paper based on this chapter has been published. **Mohseni M**, Zobeiry N, Fernlund G. (2019) "Experimental and numerical study of coupled gas and resin transport and its effect on

porosity", *Journal of Reinforced Plastics and Composites*. All parts of the paper were prepared and written by Seyyed Mohammad Mohseni while under the supervision of Dr. Navid Zobeiry and Professor Göran Fernlund. A numerical study based on Chapter 5 was presented at the 11th Canadian-International Conference on Composites (CANCOM), 2019. A paper was published in the conference proceedings. **Mohseni** M, Fernlund G."Numerical Study of the Effect of Processing Parameters on Porosity" *11th Canadian-International Conference on Composites*, Kelowna, Canada, 2019. All parts of the paper were prepared and written by Seyyed Mohammad Mohseni while under the supervision of Professor Göran Fernlund.

All experiments in Chapter 6 were designed and conducted by Seyyed Mohammad Mohseni under the supervision of Professor Göran Fernlund. The cure shrinkage characterization experiments were conducted by co-op student Yeedo Chun under the supervision of Seyyed Mohammad Mohseni and Dr. Christophe Mobuchon at Composites Research Network. All other material characterization were conducted by Seyyed Mohammad Mohseni. Development of cure kinetics and modulus models was partly performed by Alastair McKee at Convergent Manufacturing Technologies. The analytical approach for suppressing post-gelation defects was developed and validated by Seyyed Mohammad Mohseni.

Table of contents

List of tables

List of figures

Symbols

Note: Units are not defined for material coefficients and fitting parameters.

Symbol	Description	Unit
A, B, C	Material constants	–
A_f	Resin–fiber interface area/unit volume of matrix	1/m
b	Klinkenberg parameter	Pa
C	Solute concentration	mol/m^3
C_i	Hydrostatic component of the stiffness tensor	Pa
C_s	Solute concentration at bubble/resin interface	mol/m^3
C_{inf}	Equilibrium solute concentration	mol/m^3
Ca^*	Capillary number	–
CTE	Coefficient of thermal expansion	1/°C
D	Diffusion coefficient	m^2/S
E	Young's modulus	Pa
G	Shear modulus	Pa
h	Uncured prepreg thickness	m
K	Permeability (isotropic)	m^2
K	Bulk modulus	Pa
K_1	Solubility coefficient	–

Symbol	Description	Unit
K_b	Boltzmann constant	$\frac{m^2 kg}{s^2 K}$
K_{eff}	Effective permeability	m^2
K_r	Permeability for resin flow	m^2
$K_{r,resin}$	Relative permeability of resin flow	m^2
K_{gas}	Permeability for gas flow	m^2
$K_{r,gas}$	Relative permeability of gas flow	m^2
K_ξ	Permeability along ξ axis	m^2
m	Mass variable	kg
$\dot{m}$	Source term for gas generation	$\frac{kg}{m^3 s}$
M_g	Molar weight of gas	kg/mol
P	Pressure	Pa
P_a	Applied pressure	Pa
P_b	Bag pressure (gas pressure under vacuum bag)	Pa
P_c	Capillary pressure	Pa
P_g	Gas pressure	Pa
P_n	Net pressure	Pa
P_r	Resin pressure	Pa
P_w	Partial pressure of water	Pa
P_w^*	Partial pressure of water in standard condition	Pa
r^*	Critical nucleation radius	m
R	Gas constant	J/K/mol
R_b	Bubble radius	m
$R_{b,0}$	Initial bubble radius	m
Re	Reynolds number	–

Symbol	Description	Unit
RS	Relative saturation	–
RH	Relative humidity	–
RH_0	Relative humidity of the conditioning environment	–
S	Solubility	–
S_w	Porosity fraction occupied by wetting phase	–
t	Time variable	s
T	Temperature variable	K
T_g	Glass transition temperature	K
$T_{g\infty}$	Glass transition temperature of fully-cured resin	K
T_{g0}	Glass transition temperature of uncured resin	K
V	Volume variable	m^3
V_f	Fiber volume fraction	–
x	Degree of cure	–
x, y, z	Components of Cartesian coordinate system	–
x_g	Degree of cure at gelation	–
W_r	Resin molecular weight	kg/mol
α_a	Molar fraction of air	–
α_w	Molar fraction of water	–
γ_{rg}	Surface tension	N/m
ΔG	Free energy	N.m
ΔG^*	Nucleation free energy	N.m
ΔV_{Total}	Total volumetric shrinkage ratio	–
Δv_{cure}	Volumetric cure shrinkage	m^3
$\varepsilon_{cure,free}$	Cure shrinkage free strains	–

Symbol	Description	Unit
$\varepsilon_{T,free}$	Thermal free strains	–
θ	Angle variable	rad
λ	DeBenedetto parameter	–
μ	Viscosity	Pas
μ_g	Gas viscosity	Pas
v	Velocity	m/s
$v_{actual,\xi}$	Actual fluid velocity in porous media	m/s
$\hat{v}_{r,z}$	Resin flow front velocity	m/s
v_ξ	ξ^{th} component of superficial velocity	m/s
ξ	Spatial component	–
ρ_{exp}	Experimentally measured density	kg/m^3
ρ_g	Density	kg/m^3
ρ_g	Gas density	kg/m^3
ρ_r	Resin density	kg/m^3
ρ_{th}	Theoretical density of a porosity-free laminate	kg/m^3
σ	Fiberbed compaction	Pa
σ	Hydrostatic stress	Pa
φ	Porosity	–
υ	Poisson ratio	–
ω_0	Nucleation rate coefficient	1/s
ω_{ss}	Steady state rate of nucleation	1/s

Abbreviations

ASTM	American society for testing and materials
CFRP	carbon-fiber reinforced polymeric composites
CHILE	cure hardening instantaneously linear elastic
CTE	coefficient of thermal expansion
DMA	dynamic mechanical analysis
DOC	degree of cure
DSA	drop shape analysis
DSC	differential scanning calorimetry
FBG	fiber Bragg grating
FEP	Fluorinated Ethylene Propylene
IAP	increased applied pressure
RBP	reduced bag pressure
RH	relative humidity
RS	relative saturation
RVE	representative volume element
SI	international system of units
TGA	thermogravimetric analysis
TMA	thermomechanical analysis

Acknowledgments

This work has been made possible only with the support and contributions of many great people. My sincere gratitude goes to the following.

My PhD supervisor Professor Göran Fernlund whose insight, patience, and persistence not only shaped my attitude toward research but also taught me how to think clearer in general.

Professor Anoush Poursartip for giving me the opportunity to be part of the CRN, and for taking me under his wings while my PhD supervisor was on leave.

My inspiring mentors and great friends Dr. Kamyar Gordnian, Dr. Andrew Stewart, Professor Navid Zobeiry, Dr. Alireza Forghani, and Dr. Sina Amini Niaki. It has been a true privilege to enjoy the technical and moral support from such an intelligent and amiable group of people.

Colleagues who provided invaluable insight and support: Dr. Janna Fabris, Professor Sardar Malek, Professor Hannes Reiner, Martin Roy, Malcolm Lane, Alastair McKee, and Cheng Chen.

CRN's professional staff Dr. Casey Keulen, Dr. Christophe Mobuchon, Roger Bennett, and Suzana Topic who made sure all the resources are available for my research, and truly accelerated my progress.

Last but not least, my father Vali-o-lah, my mother Mojgan, my brother Ali, and my sister-in-law Parisa for making sure I always feel the warmth of a loving family despite the physical distance, and for inspiring me to keep moving forward.

Chapter 1

Introduction

Carbon fiber-reinforced polymer composites (CFRP) offer high stiffness and strength-to-weight ratios, which are desirable properties for manufacturing light-weight aerial structures. The ease of manufacturing with this material system allows manufacturing complex geometries as monolithic parts. Part count reduction significantly reduces the costs associated with design and assembly.

Despite these advantages and the notable progress in raw materials development, the adoption of CFRP in large-scale manufacturing has been slow. The Boeing 787 Dreamliner and Airbus A350 aircraft were introduced as the first large composite-intensive products in 2011 and 2013, respectively. Introducing a new material system into a manufacturing line requires additional measures to address uncertainties and overcome manufacturability challenges.

Effective manufacturing process design requires understanding of the physics active during processing and the governing parameters. Uncertainties arise due to lack of this knowledge and/or analytical models that connect the existing knowledge to manufacturing practice [1]. As a result, the cost of product development is high since manufacturing engineers rely on trial-and-error approaches. Boeing and Airbus invested about $32 billion [2] and $15 billion [3], respectively, on their development programs for the new composite-intensive aircraft. The considerable product de-

velopment cost overshadows CFRP composite's potential cost efficiency with respect to design and assembly.

Processing defects are a manifestation of uncertainties in processing. A defect is defined as an outcome that does not conform to the design, e.g. misaligned fibers and composite matrices locally devoid of resin. The present work is focused on addressing resin matrix-related defects and presents experimental studies and analytical approaches to eliminate them.

In a two-phase system of carbon-fiber-reinforced resin, the fibers provide structural strength and stiffness. The resin is responsible for binding the fibers together, and transmitting and distributing the load between fibers. Therefore, any discontinuity or defect in the resin matrix compromises the composite structure's performance. Another critical role of the resin matrix is to avoid crack propagation. Matrix defects undermine crack arrest, and they are a favorable location for crack initiation when the composite part is subject to loading.

Matrix defects can be classified into two categories based on their origin, porosity and stress-induced defects, Figure 1.1. Porosity is a processing defect defined as the absence of resin in locations expected to be occupied with resin. Entrapped air, volatile degassing, and poor resin infiltration are among known causes of porosity [4]. This defect dramatically reduces the composite structure's performance especially at locations where resin has an important role in load transfer such as interlaminar regions. It is shown that a porosity content of 2vol% causes a $10-20\%$ reduction in interlaminar strength, depending on the fiber volume fraction [5]. Porosity can also act as a stress concentrator stimulating matrix cracking [6]. Consequently, strict rules are imposed on the allowable level of porosity in parts being used in primary aerospace structures, typically $\leq 2\%$.

Stress-induced defects form due to local stress build-up in the resin. A major difference compared to porosity is that stress-induced defects arise due to structural failure of the resin matrix. With regards to matrix strength along the fiber, such defects typically form transverse to the fiber axis [9]. Resin-rich regions are also weak spots with high propensity for stress-induced defects

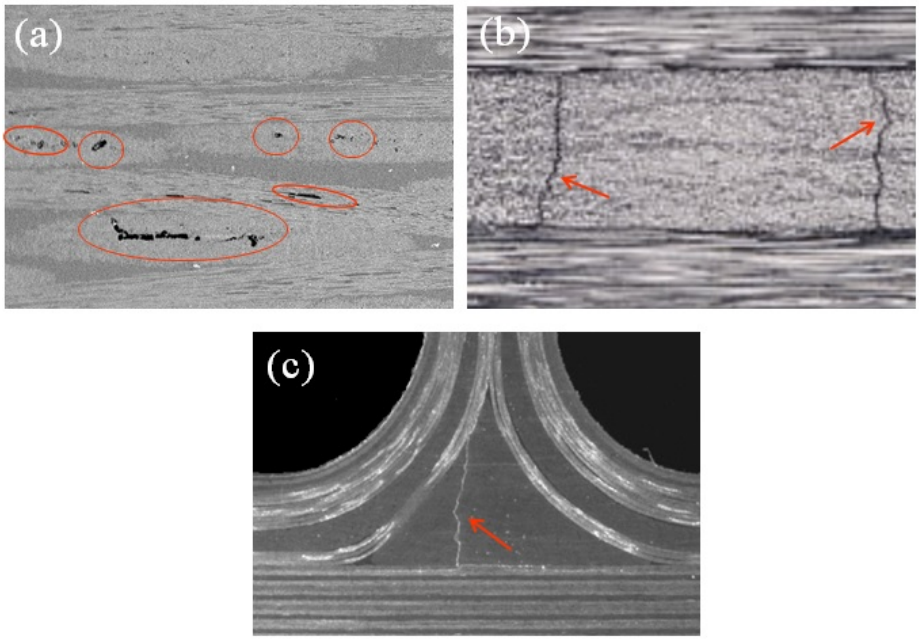

Figure 1.1: Examples of defects forming in a resin matrix: a) porosity, b) transverse matrix cracking[7], c) matrix cracking in resin-rich noodle area[8]

[10]. Matrix cracking is the most frequently reported manifestation of stress-induced defects and it is highly dependent on cure history [7] and processing conditions [11].

The underlying mechanisms leading to matrix defect, porosity and stress-induced defects, are complicated by multiple influencing processing parameters. Additionally, the evolving properties of the resin during cure further complicate the development of an analytical framework for defect prediction and prevention. As a result, manufacturing process design in this area is largely trial-and-error oriented.

The present study is focused on understanding the mechanisms causing matrix defects. The key objective is to establish analytical models and frameworks that deploy the developed knowledge in a practical manufacturing setting. Furthermore, the composite community has traditionally studied process design and optimization considering the post-cure state of the composite part, i.e. when the resin is in a glassy state. The present study aims to investigate defect formation throughout the

processing, from the beginning of cure when resin is in the viscous liquid state, to the rubbery and up to the glassy state when resin behaves as a solid.

Chapter 2

Background and literature review

2.1 Prepreg-based composites manufacturing

Among methods available for composites manufacturing, prepreg-based processing is favored for manufacturing high-performance structures, especially in the aerospace industry. This interest stems from advantages offered by this material system such as ease of handling, and a high level of control over the resin/fiber ratio and fiber alignment [12]. In view of its importance to the industry, porosity control in prepreg-based manufacturing is the focus of the present thesis. Nonetheless, the fundamental physics whereupon the present study is established are common between different processing methods.

Figure 2.1 shows the cross-section of a single ply of prepreg consisting of woven fiber tows, referred to as a fiberbed, that is partially infiltrated (pre-impregnated) with epoxy resin. Depending on the prepreg design, resin is placed on one or both sides of the fiberbed as a film. For the sake of handling, the resin in the prepreg is partially cured, referred to as "B-stage" cure, and has gel-like tacky solid characteristic [13]. The un-infiltrated region, or dry fiberbed, is a key feature of many prepregs providing an interconnected network of channels for gas transport throughout the laminate. This region is initially occupied with normal pressure air. The top view of a prepreg ply

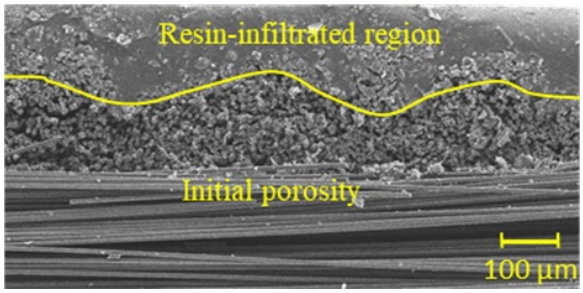

Figure 2.1: Micrograph (SEM image in secondary electron mode) showing the the initial state of the prepreg. The yellow line highlights the boundary between the resin-infiltrated region and the dry fiberbed region.

in Figure 2.2 shows the interconnected channels. These channels extend to the edges of the laminate and facilitate gas extraction during processing [14–16].

The fiberbed has a non-linear compressive stress-strain response [17], and eventually reaches a steady-state of compression for a given net pressure [14]. In processes such as out-of-autoclave manufacturing where the applied pressure on the part is relatively low and constant throughout the process, it is reasonable to ignore fiberbed compression. In other applications that involve high applied pressure on the part, the pressure sharing between gas, resin, and fiber phases can be accounted for using Biot's effective stress model [18].

After fabrication, prepregs are rolled, sealed and kept frozen in inventory. The sealing minimizes the contact between the resin and the ambient environment and lowers the risk of moisture absorption by the resin. The cold temperature prevents pre-mature polymerization of the resin prior to processing the composite part.

Composite manufacturing processes start with removing the prepreg from the freezer and allowing the material to thaw at room temperature. Subsequently, the prepreg is cut to smaller pieces based on the part design and geometry, and stacked onto a tool to achieve the desired thickness. This process is referred to as the layup step. Based on part size and geometrical complexity, the layup step may last hours to days during which the prepreg is exposed to the ambient air. Due to

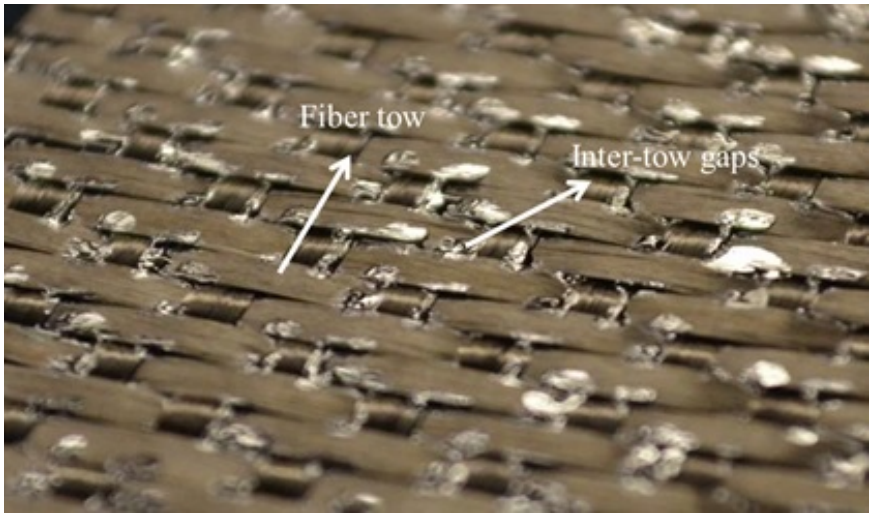

Figure 2.2: Structure of the fiberbed in a woven prepreg.

this exposure, the moisture content of the epoxy resin [19] equilibrates with the humidity in the ambient air. Air entrapment is also possible at inter-ply regions while prepreg plies are being stacked during layup. The layup step is completed by sealing the part using a vacuum bag. The use of other consumables such as breather and dry fiber tows placed at the edges of the part ensures there is an open passage for gas transport between the part and the vacuum port [20].

After layup, the manufacturing process is continued by subjecting the part to a cure cycle consisting of a sequence of temperature ramps and holds. Figure 2.3 shows a simple cure cycle with the corresponding simulation of resin properties. The graphs are related to kinetics simulation of the MTM45-1 epoxy resin [21] implemented in the Raven software [22].

Stage 1 in Figure 2.3 displays a debulk step during which the vacuum bagged part is connected to a vacuum source at room temperature. The application of vacuum during debulk causes a pressure gradient between the gas phase initially residing inside the dry fiberbed and the reduced gas pressure under the vacuum bag, that promotes gas extraction from the part. Due to the resin's high viscosity at room temperature, resin infiltration during debulk is minimal. The reduced pressure inside the dry fiberbed promotes volatile desorption from the adjacent resin. Volatiles are species such as air,

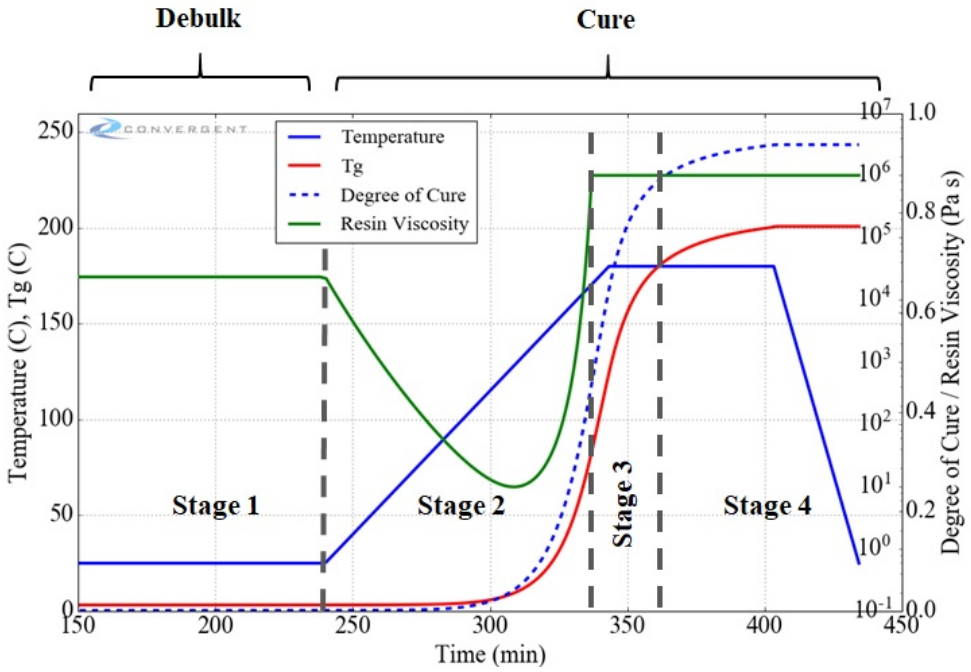

Figure 2.3: An example of a simple cure cycle and the corresponding cure simulation related to MTM45-1 resin system [22].

moisture, and chemical compounds that are dissolved in the epoxy resin [23]. Later in the process and driven by the increased temperature, volatiles can come out of solution as gas. In summary, the goal of the debulk step is to remove the existing gas inside the fiberbed and reduce the volatile content of the resin.

Stage 2 marks the initiation of the temperature ramp and cure. First, the resin viscosity drops due to the increasing temperature. Then, the initiation and progress of crosslinking between molecular chains in the thermosetting resin cause the viscosity to build up. The cure progress is demonstrated by the rise of the degree of cure in Figure 2.3. Stage 2 is seen as the processing window for porosity control, since the resin at this stage exhibits viscous liquid behavior, and it can flow and infiltrate the fiberbed. Porosity forms if the gas phase is entrapped inside the part and/or any location of the fiberbed is not fully infiltrated with resin.

The remaining volatiles from the debulk step can potentially leave the resin prompted by the temperature increase during stage 2. The released volatiles diffuse through the resin either into the transport channels or into a bubble nucleation site. In either case, the bubble [24] or gas generated inside the channels [25] can be extracted given the continued application of vacuum and open transport channels. This also holds for any air remaining inside the dry fiberbed. Generally, gas removal during cure is contingent on the extent and rate of resin infiltration. Premature resin infiltration closes the interconnected channels for gas transport and leads to gas entrapment. Additionally, slow resin infiltration may leave regions of the fiberbed un-infiltrated. Resin infiltration kinetics is determined by the cure cycle and its effect on resin rheology.

The resin's ability to flow reduces as viscosity increases. At gelation, the resin has formed a three-dimensional structure, and viscosity increases by several orders of magnitude which is equivalent to no flow upon shearing [26]. In practice, any region of the fiberbed that has not been fully infiltrated with resin freezes inside the part as porosity after gelation.

After gelation, stage 3 in Figure 2.3, the resin has a rubbery nature and exhibits viscoelastic behavior [27]. As crosslinking proceeds during stage 3, the resin develops modulus and gradually approaches elastic-type behavior with increased relaxation time. Details of the mechanical property evolution due to cure are discussed in Section 2.4.1. After gelation, the resin is able to develop internal stress. This in addition to the resin's low strength immediately after gelation increases its propensity for internal stress-induced defects. Any defects carried forward to or formed during stage 3 cannot be removed since the gelled state of the thermosetting resin is not reversible. Crosslinking between polymer chains and the established resin structure reduces the free volume available for solute species to diffuse through [28]. Additionally, this structure suppresses volatile driven bubble growth, since high vapor pressure is required to disrupt it [29]. Therefore, volatiles are not a primary concern during stage 3.

Stage 3 finishes when the glass transition temperature of the resin exceeds the cure temperature. After glass transition, stage 4 in Figure 2.3, the glassy resin acts as an elastic solid. At this stage, the polymer chains' mobility is severely reduced. Despite the resin's ability to retain stress/strains immediately after gelation, internal stress formation and corresponding defects are often studied using observations based on the glassy resin, i.e. residual stresses [27].

The review of the prepreg structure, processing steps, and resin property evolution shows that porosity formation is not limited to a specific step of processing. Further, similar to the evolution of the resin properties, process-induced defects are highly path-dependent. Therefore, a comprehensive approach to defect-free part manufacturing should capture the basic mechanisms that are in effect throughout processing.

In the case of the fiber-reinforced polymeric composites, volatile diffusion, gas transport, and resin infiltration are the basic mechanisms involved in porosity formation before gelation. Therefore, the relationship between these mechanisms and process parameters should be studied. Process parameters include pressure and temperature during cure. Furthermore, internal stress development after gelation is a major source of process-induced defects. Unlike porosity forming before gelation, internal stress-induced defects are a result of structural resin failure. However, a complete recipe for defect-free manufacturing should also address post-gelation defects through process design. With this background, the rest of this section reviews the literature for each of the major mechanisms of porosity and defect formation along with the state of the art in manufacturing process design to address them. For this purpose, these mechanisms are classified into three groups based on the fundamental physics involved:

1. Volatile (moisture) induced porosity $\rightarrow$ diffusion-based mass transport;
2. Gas/resin transport induced porosity $\rightarrow$ advection-based mass transport;
3. Internal-stress induced defects $\rightarrow$ continuum mechanics.

2.2 Moisture-induced porosity

During processing of prepreg-based composites, volatiles can off-gas from the resin. Three main volatiles in the case of epoxy resins are: moisture, nitrogen, and chemical reaction by-products [23, 30, 31]. In modern prepregs, the hot-melt method is generally used to pre-impregnate the fiberbed. This method compared to solvent-based methods minimizes the dissolved volatile content. Farhang [14] analyzed MTM45-1 epoxy resin [32] using Thermogravimetric (TGA) analysis and confirmed that moisture is the major dissolved solute.

2.2.1 Fundamentals

Studies on the nature of the water-epoxy interaction [19, 28, 33] demonstrate that water molecules have a strong affinity to epoxy resins. This affinity originates from the polar regions of the epoxide molecule where water molecules can form van der Waals or hydrogen bonds. Even if these locations are saturated, water molecules can fill the micro-voids and free volume within the polymer structure. Kay [25] reported that by conditioning the MTM45-1 resin-based prepreg at 100% relative humidity, the resin is observed to absorb moisture continuously, even after 40 days of conditioning. The resin in this prepreg system is in a B-stage state, i.e. it is about 10% pre-cured. Therefore, a complete dissolution of the resin in water is not expected.

Generally, an epoxy-water mixture is a non-ideal mixture and the equilibrium concentration of moisture in the resin should be experimentally studied and fitted to a model [23]. Through such experiments, Brand et al. [34] found that water solubility, S, in the epoxy resin can be stated as:

$$S = K_1(RH)^2 = K_1 \times 10^4 (\frac{P_w}{P_w^*})^2 \tag{2.1}$$

Here, RH is the ambient relative humidity, K_1 is the solubility coefficient, P_w is the partial pressure of water, and the standard water vapor pressure is [23]:

$$P_w^* = 4.962 \times 10^5 \exp(\frac{-4892}{T}) \tag{2.2}$$

The solubility term can be converted to concentration (C) of moisture in the prepreg as:

$$C = \frac{S}{100}\frac{\rho_r}{W_r} \tag{2.3}$$

ρ_r is the resin density, W_r is the weight fraction of the resin in the prepreg. It is worth noting that assuming a standard pressure, the equilibrium solute concentration, C_∞, is:

$$C_\infty = \frac{K_1 \rho_r}{W_r}(RH_0)^2 \tag{2.4}$$

where, RH_0 is the relative humidity of the conditioning environment. Kay [25] confirmed that the equilibrium concentration of water in uncured MTM45-1 epoxy resin at typical relative humidity levels of 0 - 75%, consistently follows this equation, with a K_1 coefficient of 5.58×10^{-5}. A similar solubility coefficient was found by Kardos [23] while experimenting on another epoxy resin system, Narmco 5208.

Porosity due to the presence of moisture is typically studied as a problem of initiation and growth of a bubble in resin. Experimental work by Wells [35] showed that the existence of the micro-voids in a typical resin system used in composites manufacturing leads to heterogeneous initiation and growth of the water vapor bubbles. Similarly, much of the literature on porosity prediction is focused on growth of a preexisting bubble rather than the nucleation process.

2.2.2 Bubble dynamics

The fundamentals of solute-driven bubble growth have remained rather unchanged since the pioneering work of Epstein and Plesset [36]. In this study, the authors developed a model for bubble growth on the basis that solute influx from bubble interface causes its mass to increase. Given the

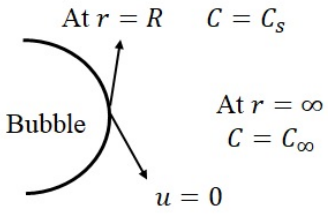

Figure 2.4: Basic assumptions in the conventional bubble growth theory; "u" is the velocity of the bubble interface which is equal to zero for a bubble stagnant in the fluid.

mass increase, the corresponding volume variation can be calculated by assuming a constant density for the gas inside the bubble. The basic assumption for developing this model is a stagnant spherical bubble with solute concentration of C_s at the resin/bubble interface, and a steady equilibrium solute concentration of, C_∞ (Equation 2.4), in the surrounding resin, Figure 2.4. C_s can be calculated using Equations 2.1− 2.3, for a bubble containing pure water vapor. If the processing condition changes such that C_s becomes smaller than C_∞, a concentration gradient forms toward the bubble. This consequently leads to solute diffusion toward the bubble and results in bubble growth when solute reaches the interface.

Based on the approach outlined above, the rate of radius change for a spherical bubble is:

$$\frac{dR_b}{dt} + \frac{DM}{\rho}\frac{\partial C}{\partial r} = 0 \tag{2.5}$$

R_b is bubble radius, D is the diffusion coefficient, M is solute molar mass, and ρ is solute density. Given the partial differential equation for the solute transfer through a spherical interface:

$$\frac{dC}{dt} = \frac{D}{r}\frac{\partial}{\partial r}(r\frac{\partial C}{\partial r}) \tag{2.6}$$

and the bubble assumptions above, Wood and Bader [37] derived the $\frac{\partial C}{\partial r}$ term as:

$$\frac{dC}{dr}_{r=R_b} = \frac{C_s - C_\infty}{R_b}(1 + \frac{R_b}{(\pi Dt)^{1/2}}) \tag{2.7}$$

Further, on the premise that the bubble is small and the diffusion coefficient of the liquid resin is high, the authors assumed that $\frac{R_b}{(\pi Dt)^{1/2}} \ll 1$. Using this assumption and combining Equations 2.5 and 2.7, an asymptotic solution for bubble size variation gives:

$$R_b^2 = R_{b,0}^2 - \frac{2DM}{\rho}(C_s - C_\infty)t \tag{2.8}$$

This is a classic solution for diffusion-driven bubble growth. However, various modifications have been proposed to improve growth predictions for specific applications. Ledru et al. [38] proposed a coupled model considering both viscous and diffusion effects. The basic bubble dynamics assumptions in this work are similar to the previous models. However, one major difference is that instead of assuming that the gas pressure inside the bubble (P_g) is equal to the resin pressure around it (P_r), the viscous and capillary effects are also included, giving:

$$P_g = P_r + \frac{4}{R_b}(\frac{\gamma_{rg}}{2} + \mu\dot{R}_b) \tag{2.9}$$

The transient bubble radius term on the right-hand side of the equation makes the final system of equations for bubble growth prediction highly non-linear, requiring special considerations for a stable and converging solution. Arefmanesh and Advani [39] further considered the effect of limited dissolved gas in their model for bubble growth in a viscous matrix. The principal author also studied models for bubble growth in a viscoelastic matrix [40].

To the best of the author's knowledge, an experimental validation for the models that consider viscous or viscoelastic effects in bubble growth has not been yet reported. However, several studies have tried to correlate the total porosity of a cured laminate with the predicted extent of bubble growth using such models [41].

Viscous effects become important around resin gelation when viscosity is high, so that the ($\frac{\mu\dot{R}_b}{R_b}$) term in Equation 2.9 becomes significant. In composites manufacturing, however, the processing

window of interest is when the resin viscosity is low, so it can flow and infiltrate into the fiberbed. Furthermore, the low viscosity allows bubbles in the resin to move and potentially be removed upon reaching the resin flow front. This effect is studied in the literature as bubble mobility [24]. Viscoelastic properties come into effect after gelation when the resin forms a 3D structure through covalent bonds. At this stage, the resin's structure does not allow for flow or stress-free local deformation, any feature inside the structure including preexisting bubbles will therefore be locked in.

Wood and Bader [31] extended their previous model of bubble dynamics, Equation 2.7, by including surface tension effects, while neglecting viscous effects. The authors compared the model predictions against experimental data from observing bubbles introduced in the resin using a syringe. Results showed that surface tension is important when the bubble is small. In the case of a growing bubble, this parameter becomes increasingly negligible as the bubble grows. Similar experimental observations in the literature confirmed a minimal effect of the viscous matrix and surface tension in predicting bubble dynamics in resin [30, 35].

2.2.3 Bubble dynamics application in composites processing

The literature shows that established bubble dynamics theories apply to the resin during composites processing. However, the goal in this area is to deploy the bubble dynamics theories to suppress bubble growth. According to Equations 2.1 $-$ 2.3, the equilibrium concentration at the bubble interface (C_s) decreases with ambient pressure. This results in concentration gradient toward the bubble and its growth according to Equation 2.8, hence porosity.

In processes such as resin transfer molding [42, 43] and autoclave-based manufacturing [15, 20], the application of increased pressure is typically used to suppress bubble growth and avoid porosity formation. However, in processes such as out-of-autoclave manufacturing where it is not convenient to change the resin pressure, other processing parameters should be manipulated for moisture-induced porosity control. Furthermore, even with the application of increased pressure,

some regions of the part may remain shielded from the applied pressure and this increases the risk of porosity formation.

According to Equation 2.8, lowering the equilibrium solute concentration, C_∞, in the resin also reduces the concentration gradient required for bubble growth. This parameter depends on the general initial condition of the resin [44]. Therefore, one approach to reduce C_∞ is to limit the humidity level at the layup room, i.e. RH_0 in Equation 2.4 [45, 46]. Nonetheless, the cost involved with changing the humidity level inside a large manufacturing facility makes this approach less practical.

Another approach is to extract the dissolved moisture, or reduce C_∞, in the resin prior to cure with the application of vacuum during a debulk stage [47]. Kay [25] conducted an extensive experimental study on the effect of debulk on moisture desorption and final porosity. The author's simplified transport model is shown in Figure 2.5. Before debulk, the moisture content of the resin is in equilibrium with the moisture content of the air inside the dry fiberbed, Equation 4. The application of vacuum during debulk reduces the gas pressure inside this zone, which is equivalent to reducing the equilibrium moisture concentration. This causes a concentration gradient between the moisture content of the resin and the moisture inside dry regions and consequently, moisture desorption. The continuous application of vacuum and the resulting gas flow transfers the extracted moisture out of the system.

Kay [25] further employed desorption models to estimate the moisture content of the resin as a function of the debulk step settings including vacuum pressure, temperature and duration. An analytical analysis showed that the required debulk time to reduce the moisture content significantly increases with the part size that determines the distance between the farthest region of the part to the vacuum port. Furthermore, a common problem in manufacturing facilities is that the vacuum system does not operate at full capacity due to issues such as line leaks [48]. Therefore, complete

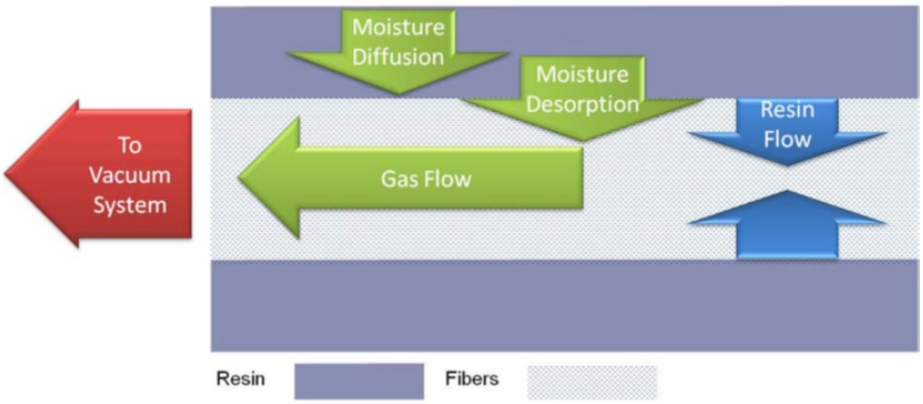

Figure 2.5: Transport mechanisms during debulking of a partially-impregnated prepreg, adapted from [25].

extraction of moisture during debulk is not practical, i.e. there will be remaining moisture content in the resin during cure.

Temperature is another processing parameter that can be controlled to avoid porosity. A common practice is that resin manufacturers recommend cure cycles based on their internal evaluations that have shown to reduce porosity [32]. The recommended cure cycles are typically developed based on trial-and-error and/or the staff's intuition based on previous experience. The lack of an analytical approach for cure cycle design to suppress moisture-driven porosity further complicates the extension of the manufacturer recommended cure cycles to applications in which part specifications, e.g. size, or ambient conditions, e.g. humidity level, significantly differ from standard conditions.

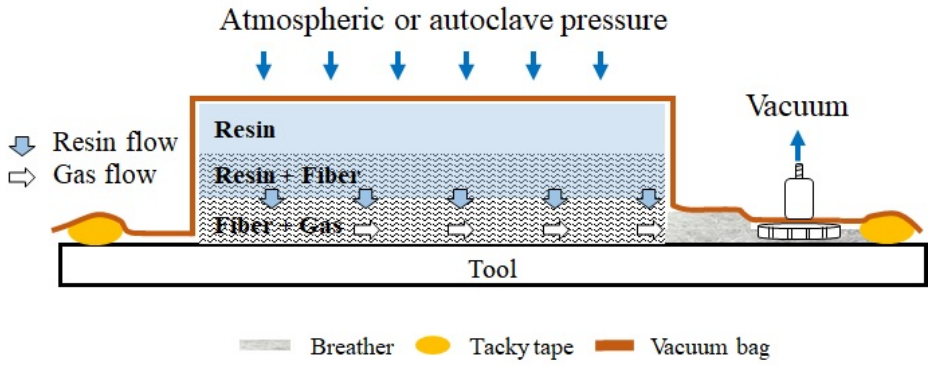

Figure 2.6: Schematic of the structure of a partially impregnated prepreg and the corresponding advection transport mechanisms active during cure.

2.3 Gas/resin transport-induced porosity

Partially impregnated prepregs are three-phase systems consisting of gas, resin, and fiber. Figure 2.6 shows a schematic of the simplified and homogenized morphology of such structure divided into three distinct regions of resin, resin + fiber, and fiber + gas. The transport mechanisms in this figure demonstrate gas and resin transport via advection. The diffusion transport mechanisms are omitted in this figure. According to Kay [25], the diffusion term related to moisture desorption can be included in the advection model for gas transport as a mass generation source term.

Gas molecules are removed from the fiber + gas region with the application of vacuum during debulk. At this step, resin infiltration at room temperature is negligible. During cure, the temperature increase results in lower resin viscosity and initiation of crosslinking between polymer molecules. A resin pressure gradient is caused by the difference between the applied pressure (atmospheric or autoclave pressure), and the reduced gas pressure inside the dry fiberbed. This is the driving force for resin infiltration. In real prepregs, there is often a small number of gas bubbles in the resin. These bubbles are isolated gas pockets that are entrapped in the resin during prepregs fabrication. The isolated voids are categorized as porosity. Thus, they should be distinguished with the micro-voids discussed in the previous section. The contribution of the isolated voids [24, 49]

to the total porosity is typically negligible ($< 0.2\%$ [50]). Further, the movement of the isolated voids in the resin is relative to the resin velocity itself [49, 51]. In the rest of the present document, isolated voids and their movement in the resin are neglected.

An accurate prediction of porosity due to gas entrapment and/or incomplete resin infiltration relies on good transport models. Gas and resin transport inside the fiberbed are problems of fluid flow in porous media. In the composite literature, these mechanisms are commonly explained using the empirical Darcy flow model [52, 53]:

$$\begin{aligned} v_\xi &= \frac{-K_\xi}{\mu_g}\frac{\partial P}{\partial \xi} \\ \xi &= x, y, z \end{aligned} \tag{2.10}$$

In this equation, v_ξ is the superficial fluid velocity, K_ξ is the ξ^{th} spatial component of the fiberbed permeability, and P is fluid pressure. The actual fluid velocity in porous media with porosity φ is:

$$v_{actual,\xi} = v_\xi / \varphi \tag{2.11}$$

The permeability term in Darcy flow model is an intrinsic property of the porous media. Analytical models exist to estimate permeability for idealized structures such as parallel cylinders [54–56]. In the composites processing literature, permeability is commonly evaluated through standard experiments and fitting the corresponding data against the Darcy flow model [57–59].

2.3.1 Gas transport

The Darcy flow model was originally developed for steady flow in a saturated porous media. However, vacuum-induced gas evacuation is a transient flow problem [60]. Therefore, various approaches and modifications were introduced to use Darcy flow model in the case of the transient gas flow. To this end, Arafath et al. [61] developed a model in which the gas phase is considered compressible. Accordingly, the continuity equation for the gas is:

$$\frac{\partial(\varphi\rho_g)}{\partial t} + \frac{\partial}{\partial \xi}(\rho_g v_\xi) = 0 \tag{2.12}$$

ρ_g is gas density and its time variation is representative of the transient gas flow. Additionally, the Darcy flow model was incorporated to explain the advection term, v_ξ. Fiberbed porosity was assumed constant, hence it does not appear in the original form of the Equation 2.12 employed in this study. This approach gives a simple transport model for gas and a timescale for estimating gas evacuation during debulk.

In Equations 2.11 and 2.12, a similar notation is used to express porosity (φ). However, porosity in Equation 2.11 refers to areal porosity, i.e. the fraction of the area at the flow front that is available for fluid flow. In Equation 2.12, φ refers to volumetric porosity that appears in the continuity equation for the fluid inside a unit volume of the porous media. A common assumption in the literature is that fiberbed is isotropic, hence areal and volumetric porosity are equivalent [52].

The Darcy flow model is valid in the viscous flow regime when there is a no-slip boundary condition between the fluid and the flow channel's wall. The viscosity in gasses is defined by the collision between the gas molecules. At low pressure where fewer gas molecules exist in a unit of volume of the fiberbed, the number of these collisions reduces. This continues until the mean-free-path of the gas molecule becomes comparable with the diameter of the transport channel. In this condition, the no-slip boundary condition will not hold [62], and the actual flow becomes faster than what the Darcy flow model would predict. Klinkenberg [63] introduced a correction to the Darcy flow model to account for this effect through an effective permeability term (K_{eff}) defined as:

$$K_{eff} = K_\xi(1 + \frac{b}{P}) \tag{2.13}$$

Here, P is gas pressure, and b is the Klinkenberg parameter. According to Equation 2.13, the Klinkenberg correction becomes important as gas pressure reduces to below the value of Klinken-

berg parameter. Kay [25] estimated a value of 11 kPa for this parameter in the case of the 5-harness MTM45-1 prepreg. The author adapted an empirical equation originally developed based on experiments on fluid flow in rockbeds [64]:

$$b = 0.112[Pa](\frac{K_\xi}{1\ m^2})^{-0.39} \tag{2.14}$$

Experimental validation supports the application of the corrected Darcy flow model in estimating the gas removal timescale during the processing [25, 65]. These studies are focused on the processing stage when resin infiltration is minimal, and it does not affect the gas flow.

Another assumption in the Darcy flow model is that fluid flow is in the laminar regime. This condition is expected to be valid when the permeability-based Reynolds number is below 1.0 [62]. Beyond this limit, the relationship between velocity and pressure diverges from linearity and flow enters into the turbulent regime [66]. The expression for permeability-based Reynolds number is:

$$Re = \frac{\rho v \sqrt{K}}{\mu} \tag{2.15}$$

In a typical MTM45-1 prepreg with a measured maximum in-plane permeability of 10^{-13} m^2 [57], and a corresponding maximum gas velocity of 0.02 m/s [25], the Reynold's number is about 10^{-3} for gas flowing inside the fiberbed. Since this number is orders of magnitude smaller than the criteria of unity, gas transport in fiberbed is expected to remain in the laminar flow region, i.e. the Darcy flow model will hold.

2.3.2 Resin transport

Considering the schematic in Figure 2.6, resin transport occurs through a geometry that includes a resin source on one side and dry fiberbed on the other side. Various studies have confirmed the application of the Darcy flow model in predicting the resin flow front progress in this unsaturated

structure [67–69]. Resin is a viscous liquid, therefore application of the Darcy flow model does not require the Klinkenberg modification.

Capillary pressure is a parameter that can considerably influence resin flow inside the fiberbed [70]. Mortensen and Wong [71] derived an equation for capillary pressure (P_c) based on thermodynamics:

$$P_c = -A_f \gamma_{rg} \cos\theta \tag{2.16}$$

where, A_f is the area of the resin–fiber interface per unit volume of the matrix, γ_{rg} is the surface tension between resin and gas, and θ is the wetting angle. The surface tension of polymers is in the range of 0.03-0.04 N/m [72]. For comparison, surface tension of liquid Aluminum (at 700°C) is about 0.87 N/m [73]. In general, the pressure drop due to capillary effect is negative in polymer composites, since the measured wetting angle, θ, is lower than 90°. The resulting effect is that capillary pressure generally enhances resin flow into the fiberbed. The contribution of capillary pressure to resin flow is implemented in the Darcy flow model as an addition to the pressure gradient term. Assuming the pressure gradient term in Equation 13 remains constant with distance, i.e. $dP_r = \Delta P_r$ [72]:

$$\Delta P_r = P_g + P_c - P_a \tag{2.17}$$

Equation 2.16 assumes a homogenized distribution of fibers. However, the common fiberbed architectures used in composites manufacturing are made of woven fiber tows, as shown in Figure 2.2. Therefore, the capillary effect is not even throughout the fiberbed, being negligible in inter-tow regions and comparatively significant in intra-tow regions where fiber spacing is much smaller, 5 -10 μm [70]. This motivated many studies on dual-scale characteristic of the woven prepregs [52, 54, 74].

Studies on dual-scale permeability commonly use a single ply of woven prepreg. This contrasts the real-world layups that include stacks of prepreg plies. Babu and Pillai [75] examined the nature of the dual-scale permeability in different fiberbed architectures in stacks. The authors tracked the pressure profile at the resin inlet during flow-rate-controlled in-plane infusion tests. In fiberbed architectures that maintain a dual-scale characteristic, a decrease in the inlet pressure curve is expected due to the delayed resin flow into the intra-tow regions. Surprisingly, results showed that the inlet pressure history of the woven fiberbed remains linear. This led to the conclusion that inter-tow regions need to form continuous uninterrupted macrochannels along the length of the mold for delayed infiltration to take place. Otherwise, despite the distinguishable inter and intra-tow regions of a single ply, the stack cannot be classified as dual scale [76].

The manifestation of the dual scale characteristic also depends on resin flow velocity. Experimental results showed that if resin flow is slow, intra-tow regions become infiltrated with resin earlier than the inter-tow gaps [77]. This causes porosity formation within the inter-tow region due to gas entrapment. In contrast, high resin velocity leads to porosity within intra-tow regions due to delayed resin infiltration. Hence, an optimal velocity should be used that leads to simultaneous resin infiltration into the inter and intra-tow regions. Multiple studies in the literature [78–81] associated the observed dual scale characteristics with the ratio of the viscous to capillary effects, scaled by a modified capillary number:

$$Ca^* = \frac{\mu v}{\gamma_{rg} \cos\theta} \tag{2.18}$$

In this equation, μ, v, and γ_{rg} are the viscosity, velocity, and surface tension of the infiltrating liquid, respectively. θ is the wetting angle. According to the experimental results in [78, 79], regardless of the type of the liquid, an optimal range of capillary number, 0.003 – 0.02, balanced the flow rate in inter and intra-tow regions and minimized porosity within both regions.

2.3.3 Coupled gas/resin transport

A good understanding of the independent mechanisms of gas and resin transport has been developed in the literature. The corresponding studies provided useful tools to estimate timescales for resin flow front progression or remaining gas after debulk, or they served as different approaches for characterizing the fiberbed permeability.

In an actual composite processing cycle, it is not possible to limit gas and resin transport to a specific stage of processing. Experimental evidence such as partial resin infiltration during hot debulk [47] or entrapped gas during cure [82] demonstrate situations where resin infiltration and gas flow occur simultaneously. Therefore, a representative model for porosity evolution should address the simultaneous flow of resin and gas in the fiberbed.

Gas entrapment during composite processing is a prime example of a process-induced defect due to unbalanced gas and resin transport. Yeager et al. [83] conducted an analytical study on the effect of the gas evacuation timescale on resin flow into a single fiber tow and the corresponding porosity evolution. The study was intended to determine how the time that a part is subject to vacuum influences resin infiltration and intra-tow porosity. For this purpose, the authors used a closed-form equation for gas transport [65] to explain internal gas pressure variation with distance from the vacuum port and the debulk time. An independent Darcy flow model is used for resin transport prediction in which gas pressure appears in the resin pressure gradient term. Nonetheless, gas pressure is calculated once as an initial state of the dry region of the fiber tow. In the subsequent time steps, gas pressure is updated based on the ideal gas law and the volume variation due to resin flow front progress.

The closed-form equation for gas pressure in this study assumes that gas transport is not affected by resin infiltration into the fiber tow. Therefore, the geometry and permeability of the gas transport channels remain constant. Moreover, this model does not account for transient gas pressure during

resin flow simulation. This is not a realistic assumption because the gas entrapment only happens if resin infiltration disconnects the gas transport channels from low gas pressure zones.

Helmus et al. [84] developed sequentially coupled models for air evacuation during the room-temperature hold, and resin infiltration during the elevated-temperature portion of the cure cycle. The authors used fiberbed compaction as an intermediate mechanism to connect these two stages of processing. During the room-temperature hold, the vacuum-assisted evacuation reduces the gas pressure inside the part. Subsequently, the reduced gas pressure leads to fiberbed compaction (σ), assuming:

$$P_a = P_g + \sigma \tag{2.19}$$

In this equation, the resin and its role in pressure sharing with gas and fiber has been neglected [17, 85]. Additionally, gas pressure is updated based on the remaining mass of the air after a certain debulk time [61]. For this, the authors use the ideal gas law and the assumption that permeability remains constant throughout the simulation. However, permeability variation is a natural consequence of the transient fiberbed compaction.

Given the calculated compaction, resin infiltration into the fiberbed during elevated-temperature cure is calculated assuming [86]:

$$\frac{\partial \sigma}{\partial x} = \frac{\partial P_r}{\partial x} \tag{2.20}$$

The resin pressure gradient from the equation above was then fed into the Darcy flow model to evaluate resin flow front progress. The physical interpretation of the Equation 2.20 is that fiberbed relaxation after the initial compaction leads to resin transport. Therefore, the gas pressure's direct contribution to resin infiltration is discarded. The evaluation of the developed model's performance showed that the thickness variation rate determined based on the experimental data decreased earlier

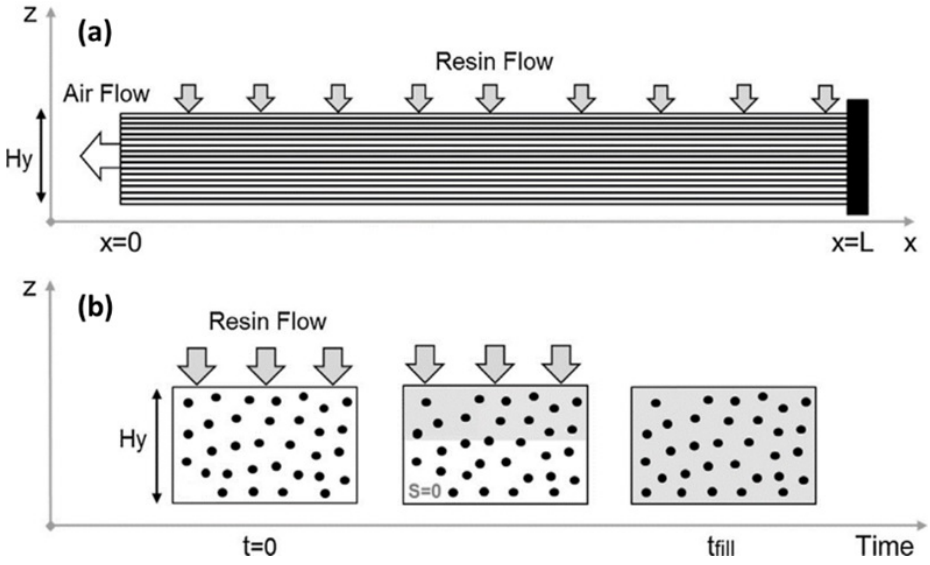

Figure 2.7: Schematic of Kourkoutsaki et al. model for coupled gas and resin transport during prepreg-based manufacturing, adapted from [87].

than what the model predicts. Helmus et al. [84] associated the observed discrepancy with the possibility that gas transport is occurring slower than predicted which in turn impedes resin infiltration.

Kourkoutsaki et al. [87] proposed a coupled gas/resin transport model to enhance the local resin infiltration prediction under the influence of the transient gas flow. Figure 2.7 demonstrates the basis of the model in which resin flow occurs through-thickness while air evacuates the fiberbed through in-plane gas transport.

The Darcy flow model for gas transport predicts the internal gas pressure throughout the length of the part. Gas flow is driven by the pressure gradient between the local gas pressure and the vacuum pressure applied to the edges of the part, location $x = 0$ in Figure 2.7. Resin infiltration is also explained by the Darcy flow model and is driven by the pressure gradient between the internal gas pressure and the constant atmospheric pressure on top of the laminate. The gas pressure term in the transport model for the resin is the basis of the coupling between resin and gas transport in this model.

A fundamental assumption made by Kourkoutsaki et al. [87] regarding gas transport was the openness of the channels for gas flow. As a result, the corresponding model would not account for entrapped gas compression due to continuing resin infiltration. Resin infiltration continues so long as the pressure gradient due to the reduced gas pressure or increased applied pressure is preserved [88]. In these cases, neglecting the gas compression would overestimate the resin infiltration advance.

Further, permeability and porosity in Darcy flow models for both gas and resin were assumed to remain constant. In the case that fiberbed is at its maximum compaction state, it is reasonable to consider constant geometry for the porous media channels wherein resin infiltration happens. However, resin flow progress changes the geometry of the fiberbed channels for in-plane gas transport. A smaller part of the initial dry fiberbed is available for gas transport as resin infiltration into the fiberbed advances. Therefore, the assumption of constant fiberbed geometry in the case of gas transport cannot be physically justified.

Another drawback with the independence of the gas transport model from resin transport is that resin infiltration into the fiberbed does not influence the local gas pressure. Experimental evidence by Centea and Hubert [89] suggests that for a constant applied pressure, final porosity remains relatively constant, even without vacuum applied under the bag. This indicates that applied pressure, and the resulting resin infiltration, can cause local gas compression, and eventually transport to low-pressure regions outside of the part.

A conventional approach to model the interaction between two fluids during simultaneous flow is based on how their flow progress changes the total permeability (K) of the porous media [90, 91]. According to this approach, a saturation term is defined as the volume fraction of the porous media occupied by the wetting phase, e.g. resin in simultaneous flow of resin and gas. Then, permeability for each fluid is defined as:

$$K_r = K_{r,resin} \cdot K$$
$$K_{gas} = K_{r,gas} \cdot K \tag{2.21}$$

$K_{r,resin}$ and $K_{r,gas}$ are relative permeabilities of resin and gas, respectively. In the oil and gas literature, relative permeabilities are found experimentally for specific porous media, porous media compaction, and groups of fluids. The drawback of this approach to composite processing applications is that the relationship between the relative permeability and porous media properties such as porosity, and fluid properties such as viscosity and surface tension are not established. The limited progress in this area has relied on case specific experimental characterization [76].

It is difficult to physically justify the concept of relative permeability. Assuming simultaneous flow of fluids A and B, the increasing saturation of the porous media with fluid A would not change the characteristics of the media in terms of the spacing between fibers or fiber diameter. However, the increasing saturation level reduces the space in the porous media that was initially available for fluid B's flow, i.e. porosity. This does not change the intrinsic permeability of the remaining un-infiltrated region.

The study by Shodja and Feldkamp [92] introduced an analytical framework for modeling the coupled flow of two fluids in the porous media. In this study, one of the fluids is categorized as wetting phase, e.g. resin, and the second one as non-wetting phase, e.g. gas. Similar to Kourkoutsaki et al.'s [87] model, the gas pressure is embedded into the transport model for the wetting phase through the pressure gradient term. However, an improvement to previous models is that the porous media's saturation with the wetting phase appears in the transport model for the gas. For this purpose, the authors consider the porosity term in the continuity equation for gas, Equation 2.12, to be a saturation-dependent variable:

$$\varphi = \varphi_0(1 - S_w(t)) \tag{2.22}$$

φ_0 is the initial porosity of the fiberbed and S_w is defined as the volume fraction of the initial porosity that is occupied by the wetting phase. The original model developed by Shodja and Feldkamp [92] is related to the natural flow of water and gas in soil. Although the associated mechanisms are similar to the gas/resin transport, modification and extension of this approach to composite processing application has not been investigated.

2.4 Internal stress-induced defects

2.4.1 Mechanical property evolution during cure

Historically, internal stress development received much attention as one of the main culprits in manufacturing of defect-free composite parts [93]. In thermoset resins, internal stress development can be traced back to the resin's mechanical property evolution due to crosslinking reactions. This evolution originates from the resin's transition during cure, i.e. from the initial viscous liquid state to a viscoelastic rubbery state, and finally to an elastic glassy solid state, Section 2.1.

Thorpe [94] characterized the shear modulus of the MTM45-1 toughened epoxy resin and its evolution with cure, Figure 2.8. This resin system is partially pre-cured, about 10%, and it is not a liquid at room temperature. Therefore, it shows a non-zero shear modulus at the beginning of the temperature ramp. Initially, the shear modulus undergoes an initial drop when the temperature ramp starts. The continuing temperature increase and the resulting crosslinking between polymer molecules causes the shear modulus to build up and balance out the temperature increase effect. This is followed by a jump after gelation where the shear modulus significantly increases. This is an example of the shear modulus evolution with cure observed in thermosetting resins.

Bulk modulus is another important property that becomes critical when studying hydrostatic stresses. Nawab et al. [95] used a dilatometry method to characterize bulk modulus of a Vinylester resin as a function of degree of cure. Results showed that the bulk modulus evolves from 0.25 GPa for the uncured resin to 2.5 GPa for the fully-cured resin, Figure 2.9. A key takeaway is that unlike the shear modulus, the bulk modulus is not equal to zero for the uncured, liquid resin, and it has a rather noticeable value at this state. When comparing with the shear modulus, the bulk modulus does not experience a sudden, and large increase during cure.

The studies mentioned above use specific resin systems and methods for shear and bulk modulus characterization. However, a survey of the literature [96–99] shows that regardless of the characterization method used, the following conclusions can be made:

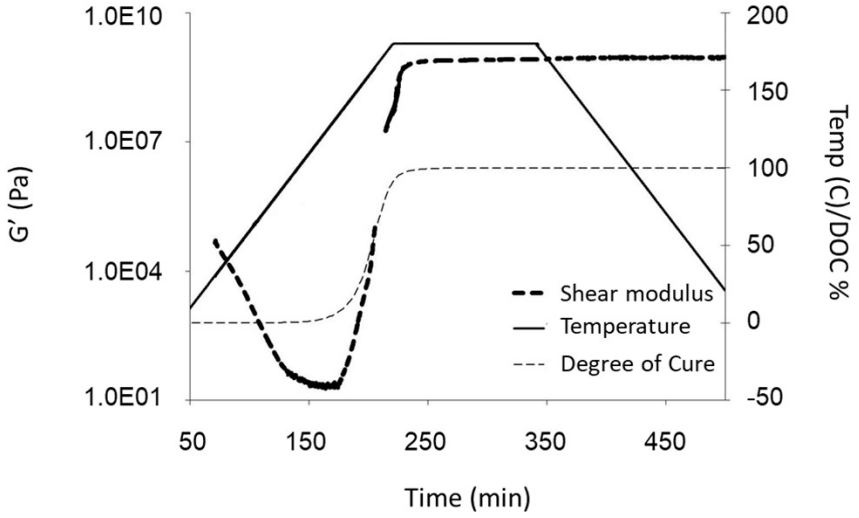

Figure 2.8: Shear storage modulus variation with cure progress for MTM45-1 resin, adapted from [94].

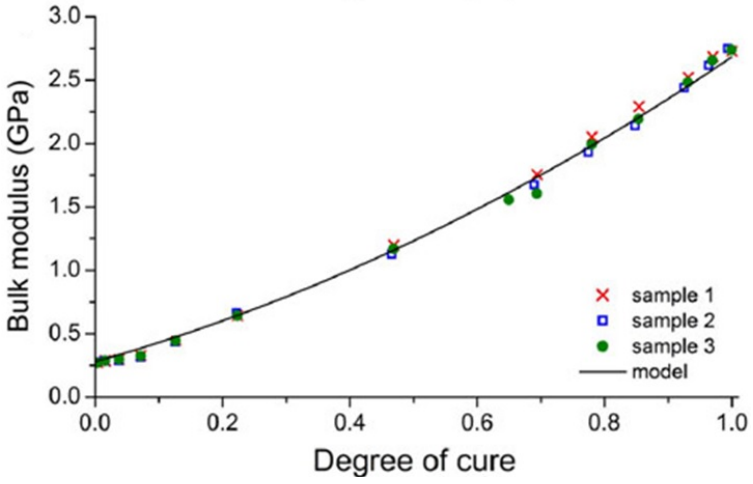

Figure 2.9: Bulk modulus variation with cure progress for MTM45-1 resin, adapted from [95].

- Shear modulus is negligible prior to gelation;
- Shear modulus increases multiple orders of magnitude after gelation;
- Uncured, viscous liquid resin has a notable bulk modulus;
- Bulk modulus increases about one order of magnitude throughout cure;
- The value of the bulk modulus reported in the literature ranges between 0.25 to 4 GPa, regardless of the chemistry of the resin system;
- In contrast, shear modulus values differ greatly between different resin systems.

2.4.2 Origins of internal stress

In composites processing, free strains are the root causes of internal stress formation [100]. Thermal strain and cure shrinkage are two main sources of free strains. The word free refers to that these strains do not form as a result of external applied stresses. Furthermore, free strains do not lead to stress development in a homogeneous and unconstrained body. Therefore, internal stress in the literature is studied after gelation when the resin forms a three-dimensional structure, withstands load, and cannot flow like in the liquid phase. In this condition, the bonding between resin and fiber, or any geometrical constraint on resin, accompanied by free strains, leads to stress development. Internal stress development before gelation, has been attributed to the interaction between fiberbed and tool without any influence from the resin [101, 102].

Thermal free strains, $\varepsilon_{T,free}$, can be calculated with the knowledge of the coefficient of thermal expansion (CTE) of the resin:

$$\varepsilon_{T,free} = \text{CTE} \times \Delta T \tag{2.23}$$

The CTE of the resin changes when the material goes from a rubbery to a glassy state. Inside each of these regions, the CTE varies with temperature, Figure 2.10 [100].

Characterization of the CTE before gelation is not common. Nonetheless, the experiments by Mobuchon and Poursartip [103] indicated a slight decrease in resin CTE with cure progress in this

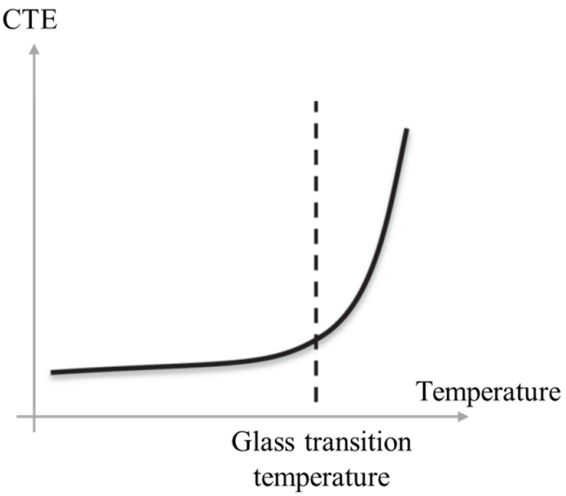

Figure 2.10: Variation of the coefficient of thermal expansion with temperature, before and after glass transition, adapted from [93]

region. Their results of testing toughened 8552 epoxy resin revealed about 12% CTE decrease throughout the viscous liquid and rubbery regions, $0 \leq DOC \leq 0.4$.

Volumetric shrinkage of the thermosetting resins originates from the formation of chemical bonds during cure. Due to crosslinking of the polymer chains, the weak intermolecular van der Waals forces are replaced with strong covalent bonds that have shorter bond length, hence volumetric shrinkage [104]. Therefore, measurements of chemical cure shrinkage are complementary to measurements of degree of cure and contribute to the understanding of the material behavior. Due to its importance in design and manufacturing various methods and tools have been investigated for cure shrinkage measurements.

Nawab et al. [105] examined cure shrinkage of Vinylester resin using dilatometry and found a final resin shrinkage of 7.1% at cure completion. The authors reported a linear relationship between cure shrinkage and degree of cure, throughout a complete cure cycle. A noteworthy observation was that final cure shrinkage reduced by adding fibers to the system. Specifically, the 7.1% final shrinkage of the neat resin reduced to 6.55 and 5.51% after incorporating 32 and 49 vol% of contin-

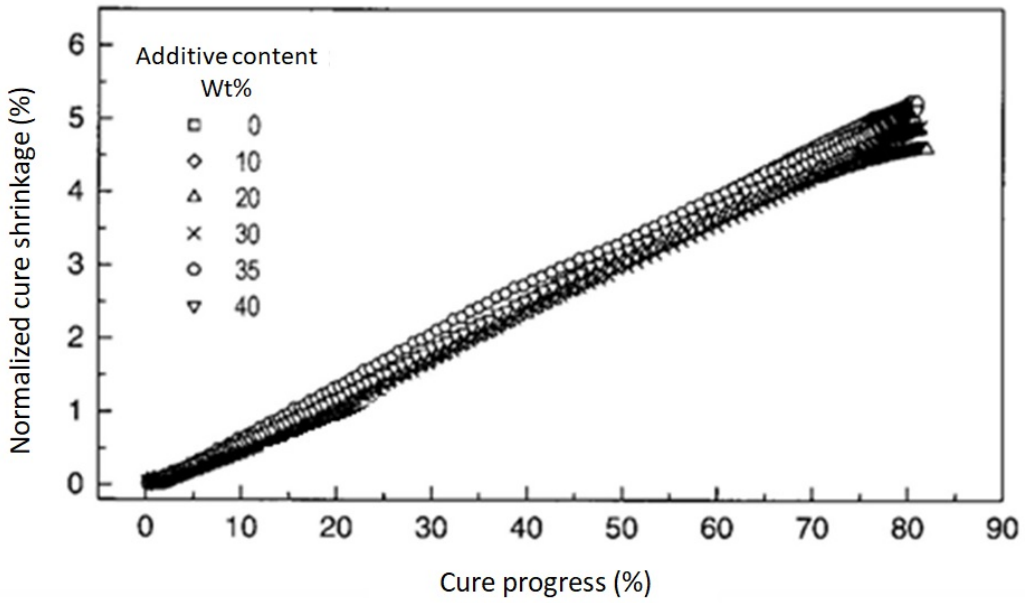

Figure 2.11: Variation of the cure shrinkage with cure progress for different amounts of additive in a model epoxy, adapted from [106].

uous fibers, respectively. This is interpreted as a direct influence of fibers in constraining stress-free shrinkage of the resin.

Holst et al. [106] used a Laser Scanning Dilatometer to examine cure shrinkage of a model epoxy resin with filler additives. Results showed that the additive content did not affect the linear trend of the cure shrinkage evolution normalized by the additive volume fraction, Figure 2.11.

The linear relationship between cure shrinkage and cure kinetics has been verified in multiple other studies, e.g. [103, 107]. This facilitates the calculation of the free shrinkage strain, $\varepsilon_{cure,free}$, as:

$$\varepsilon_{cure,free} = \Delta V_{Total} \times \mathrm{DOC} \tag{2.24}$$

where, ΔV_{Total} is the total volumetric shrinkage ratio at complete cure state, i.e. $\mathrm{DOC} = 1$.

2.4.3 Internal-stress-induced defects

The knowledge developed about the cure-dependency of the resin properties and free strains enabled the composite manufacturing community to understand internal stresses during processing [93]. This knowledge has traditionally been utilized to compensate dimensional changes of the final part due to residual stresses. Residual stresses are the internal stresses that remain in the matrix after processing [11, 108]. Dimensional changes are manifestations of the macro-level residual stresses that arise due to the stress discontinuity between prepreg plies in a stack. However, the study by Li et al. [7] on the cure cycle effect on matrix-cracking, also draws attention to micro-level residual stresses. This type of stress arises due to the mismatch between the free strains of the resin and fiber. Therefore, its systematic evaluation requires understanding of internal stresses evolving at the resin level vs prepreg (resin + fiber) level, and their effect on the overall performance of a composite structure.

In addition to the micro-level residual stress, the understanding of the internal stress effect at the resin level has practical advantages in preventing defect formation in resin-rich areas. Resin rich areas are common in composite parts and form at locations such as noodles in T-joint [8], inter-tow resin pockets [109, 110], interlaminar layers [111], and gaps formed at corner radii of angled parts [10, 112].

Studies on residual stresses focus on post-process part geometry deviations, since in the presence of fibers, the corresponding high strength prevents local failure of the resin. However, in the absence of fibers, neat resin will be highly prone to form internal stress-induced defects in the form of local failure of the matrix [113].

Different approaches have been taken in the literature to investigate internal stress development and defect formation during cure of neat resins. Generally, these approaches can be classified into three types: in-situ stress measurement, in-situ strain measurement, and off-line free-strain measurement coupled with in-situ resin behavior observations.

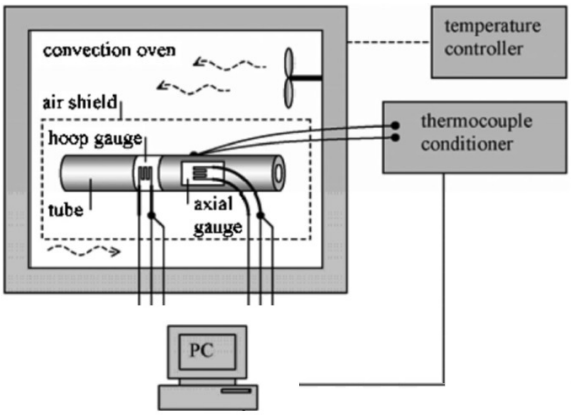

Figure 2.12: Apparatus used for in-situ internal stress measurement by Merzlyakov et al. [114], figure adapted with slight modifications.

Merzlyakov et al. [114] followed the in-situ stress measurement approach to investigate thermal and cure shrinkage induced stresses. For this purpose, stainless steel tubes were instrumented with strain gauges in both hoop and axial directions, Figure 2.12. The strain gauge readings were calibrated against temperature variations of the empty steel tube and its known CTE. In another calibration step, the stress readings of the apparatus were calibrated by pressurizing the steel tube using a pressure-transmitting oil, up to a certain value. Different uncertainties undermine the reliability of this approach for accurate cure-shrinkage induced internal stress measurements. These include multiple stages of calibration, the assumption of perfect adhesion between gauges and the instrument, and the CTE calibrations for the gauges. Furthermore, the steel tube is opaque so it did not allow in-situ observations of the resin behavior. For the sake of the tube's reusability, the cured resin was extracted destructively which eliminated the possibility of post-cure observations.

More importantly, the instrument used by Merzlyakov et al. [114] is calibrated for increased internal hydrostatic pressure. This rules out the accuracy of any hydrostatic tensile stress, readings that are expected due to cure shrinkage in the absence of thermal expansion. The researchers increased the internal pressure of the resin to up to 40 MPa and studied its variation during the cure cycle.

The in-situ strain measurement approach by Harsch et al. [115] used fiber Bragg grating (FBG) sensors to measure strain development by embedding the fiber sensors inside the curing resin. Fiber Bragg grating consists of distributed Bragg reflectors in the optical fiber that reflect a particular wavelength of light and transmit the rest. Any variation of the spacing between reflectors would influence the wavelength of the reflected light. This principle along with accurate calibration make FBG a precise strain gauge and justify its application in health monitoring of composite parts [115, 116]. By using such setup, Harsch et al. [115] reported that the gelation time indicated by the first detectable strain closely matches the value from rheometry. For the rest of the cure cycle, the authors qualitatively attributed variations in strain readings to resin evolution during cure. FBG inside the resin acts as continuous glass fiber and contributes to resin strengthening that in turn influences the stress-free cure shrinkage. Therefore, despite its common application as a strain gauge, a reliable quantitative assessment of the cure shrinkage progress is not possible. Technical challenges with the application of FBG include the precise calibrations required for thermal effect, the assumption of perfect adhesion between FBG and resin, and the difficulty of distinguishing between strain directions, e.g. hoop vs longitudinal.

The last two approaches mentioned above are focused on in-situ measurement of cure-induced stress/strain. An advantage is that in-situ methods are not geometry dependent, e.g. strain gauges can be attached to the surface of a steel tube as well as a spherical tool [117]. Although this is an advantage to the industry for in-line monitoring, the errors, calibration, and the associated technical uncertainties make these methods unsuitable for fundamental research. The direct readings of the stress/strain values eliminate the need for detailed materials characterization. For example, an alternative to the direct stress data acquisition through sensors is to characterize the mechanical properties and cure kinetics/shrinkage. Subsequently, for any arbitrary geometry and cure cycle, the shrinkage-induced free strains and the corresponding stresses can be calculated. Nevertheless,

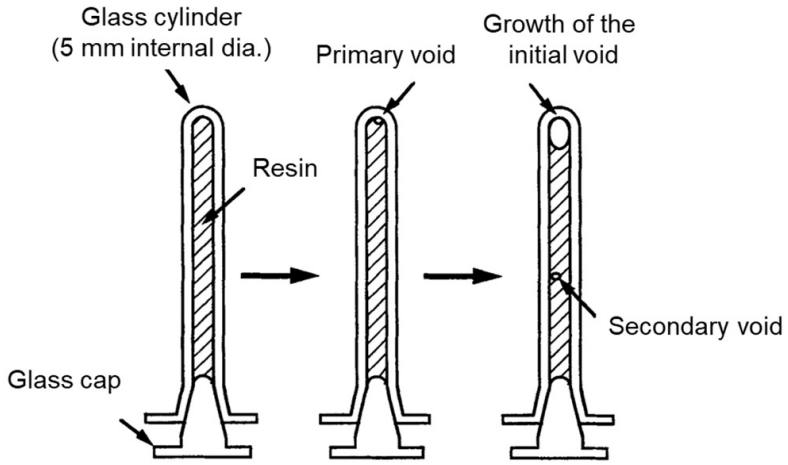

Figure 2.13: Experimental setup and observations regarding internal stress induced defect formation by Eom et al. [118], figure adapted with slight modifications.

recent advances in high fidelity characterization methods and tools promote the former approach over in-situ methods in the case of the fundamental research work.

Eom et al. [118] have previously used the approach of off-line free-strain measurement to study internal stress-induced defects in constrained neat resin. They injected epoxy resin into 9 cm long glass cylinders with 5 mm diameter to observe the resin behavior during cure, Figure 2.13. This geometry assisted in constraining the resin since epoxy has strong adhesion to glass. It is reported that after increasing the temperature and initiation of polymerization, a primary void appeared at the top of the vertically-standing cylinder. This void appeared when the resin was in the viscous liquid state, and due to the total volumetric shrinkage of the resin. Later in the cure, a secondary void formed after the resin reached the gelation point. Finally, the authors used the observed defect formation point as a criteria for internal stress-induced defect formation and calculated its value given the characterized shear modulus.

One of the challenges with the setup used is that due to the resin's transparency it cannot be confirmed whether at the point of defect formation the gelled resin was completely constrained. Additionally, there is no information about the morphology of the secondary defect. Therefore, it

is not possible to judge whether the observed void is a defect due to local resin failure, or if it is a preexisting small void that started expanding after gelation.

For stress calculations, Eom et al. [118] used the generalized stress resulting from the Boltzmann superposition integral with the hydrostatic component of the stiffness tensor defined as:

$$C_i = \frac{(1-\upsilon)E}{(1+\upsilon)(1-2\upsilon)} \tag{2.25}$$

where E, Young's modulus, is calculated based on shear modulus characterization and:

$$E = \frac{2G}{1+\upsilon} \tag{2.26}$$

with υ, Poisson ratio set to 0.33. The shear modulus is of the order of a few Pascals at the time resin reaches gelation. Therefore, the critical internal stress at the moment of secondary void formation were reported in the range of 10^{-5} – 10 Pa. Equations 2.25 and 2.26 assume that the material is fully-elastic. However, the resin is rubbery after gelation and Equation 2.25 should be substituted with [99]:

$$C_i = \frac{K}{3} \tag{2.27}$$

where, K is the bulk modulus. It should be noted that in contrast to the Young's modulus of the gelled resin, the bulk modulus is in the order of GPa.

In conclusion, the off-line free-strain measurement approach offers a robust way to observe and analyze internal stress-induced defects, if accompanied by high-fidelity materials characterization. However, the setup and analysis by Eom et al. [118] have some limitations.

A representative approach for cure-induced internal stress analysis and the corresponding defect formation mechanisms would allow studying process optimization to predict and avoid such defects.

The knowledge developed about defect control would enable minimizing micro-scale stresses during composite processing and avoid defects in resin-rich regions of the composite part.

In composite processing, resin pressure and temperature are the main process parameters that can be controlled. After gelation, when the resin forms a three-dimensional structure, it resists pressure transfer as opposed to its liquid-like behavior before gelation. Merzlyakov et al. [114] have previously shown that an initial hydrostatic pressure of about 140 MPa applied to resin in a constrained geometry is relieved during cure, due to the cure shrinkage. After gelation, resin rich areas of composite structures, e.g. noodles, act as such constrained geometries. The gelled resin surrounding the resin-rich regions would not allow stress relaxation and it blocks the transfer of any external pressure. Therefore, temperature control through cure cycle design should be examined with regards to internal stress control in constrained geometries. Such approaches have been previously noted in the literature [99, 119, 120]. However, a generalized analytical approach that addresses internal stress control throughout a complete cure cycle, and is validated through representative experiments has not been presented to date.

Chapter 3

Thesis objectives

A large body of literature is devoted to understanding the mechanisms of porosity formation in polymeric composites manufacturing. In this thesis, the goal is to investigate and address gaps in the current understanding and to lay the foundation for a validated and practical analytical approach to porosity management that covers the whole manufacturing process from the debulk stage up to the resin vitrification point. With this overall goal, three research objectives have been defined:

1. Develop an effective and practical method for suppression of moisture-driven bubble growth: It is expected that the classic bubble dynamics theories can be used to describe when bubbles will grow due to moisture diffusion. However, the appropriate analytical approach and the experimental evidence to validate it have not been investigated to date. The objective is to develop an analytical approach to suppress moisture-driven bubble growth and provide experimental validation of the approach.

2. Study and develop a mathematical model for the interaction between gas and resin flow during heat-up and cure: Gas transport during debulk has traditionally been treated as a single-phase flow in porous media. However, during cure, the resin viscosity drops due to temperature increase and it slowly infiltrates the same porous bed that gas transport is occurring within.

In the literature, gas and resin transport are studied independently through separate, and uncoupled Darcy flow models. The objective in the present study is to develop experiments to study and evaluate the interaction between gas and resin transport during cure and then to investigate extensions to current flow models to account for this interaction.

3. Study and develop an understanding of defect formation in the post-gelation stage: Post-gelation is one of the least studied stages of composites manufacturing in general. The conventional belief is that at this stage, the matrix is set and solidified and does not allow porosity to form or grow. The objective is to develop experiments that systematically evaluates the nature and mechanisms of defect formation at the post-gelation stage.

Chapter 4

Cure cycle design to suppress moisture-driven bubble growth

This section presents an analytical approach to suppress moisture-driven bubble growth and porosity during composites manufacturing. Conventional validated bubble dynamics theories are employed for this purpose. Before presenting the approach, the basic assumptions made concerning bubble dynamics theories are discussed. The main objective is to develop a validated approach that is practical in the context of manufacturing and process design. Therefore, representative experiments are conducted to validate the proposed approach.

4.1 Analytical approach

The problem of moisture-induced porosity is approached by considering a model system with a single air-water bubble in a representative volume element (RVE). A 2D presentation of the RVE is shown in Figure 4.1. This RVE has a resin pressure of P_r, temperature T and the contained resin has been conditioned in an environment with a relative humidity of RH_0. Because of the exposure to humid air, the resin has a uniform equilibrium concentration of water, C_∞, in the bulk and the

concentration of water at the bubble-resin interface is C_s. In this model, viscous and capillary effects at the resin/bubble interface are neglected. Therefore, the gas pressure inside the bubble, P_g, is equal to the resin pressure, P_r. The bubble is small compared to the RVE and the concentration in the bulk is assumed to be constant and not affected by any transport processes.

The main content of a preexisting bubble in the resin is air. At equilibrium, the water vapor concentration inside this bubble is equal to the humidity of the ambient air which is about 0.02wt%, at the standard condition [23]. The first part of the present chapter evaluates the effect of air inside the preexisting bubble on its dynamics during processing. Considering the molar fraction of water, α_w, and partial pressure of water, P_w, Dalton's law for a mixture of water and air gives:

$$P_w = \alpha_w P_g \tag{4.1}$$

Given Equations 2.2 and 2.3, water concentration at the bubble/resin interface at a specific temperature and partial pressure of moisture is:

$$C_s = 4.061 \times 10^{-8} \frac{K_1 \rho_r}{W_r} \exp(\frac{9784}{T}) P_w^2 \tag{4.2}$$

In this equation, ρ_r and W_r are resin density and its weight fraction in a prepreg system, respectively. K_1 is the solubility coefficient of moisture solution in the resin. With respect to the findings of Kay [25] for MTM45-1 5HS prepreg and of Kardos et al. [23] for T300/Narmco 5208, this coefficient is set to 5.58×10^{-5}. As a reminder from the Section 2.2.1, the equilibrium moisture concentration in the resin is:

$$C_\infty = \frac{K_1 \rho_r}{W_r} (RH_0)^2 \tag{4.3}$$

The ratio of the moisture concentration in the bulk of the resin to the saturation concentration at the bubble/resin interface is defined as the relative saturation [35]:

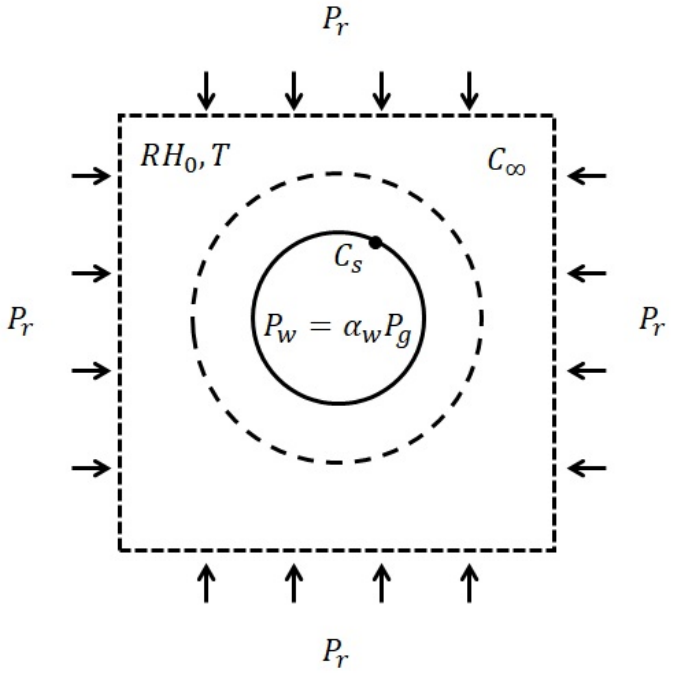

Figure 4.1: Two-dimensional representative volume element (RVE) of an air/water bubble in a resin matrix with dissolved water. T: temperature; RH_0: ambient relative humidity; P_g: gas pressure; P_r: resin pressure; P_w: partial vapor pressure; α_w: molar fraction of water in the air–water mixture; C_∞: equilibrium water concentration in the bulk; C_s: water concentration at the bubble/resin interface.

$$RS = \frac{C_\infty}{C_s} \tag{4.4}$$

When the relative saturation equals one ($C_s = C_\infty$), there is no driving force for solute diffusion and a relative saturation of greater than one will cause bubble growth. The former condition results in a concentration gradient driving the dissolved water molecules in the resin toward the bubble interface.

4.1.1 Stable and unstable bubble growth

At equilibrium, the relative saturation is equal to unity for a resin exposed to humid atmosphere. Equations 4.2 and 4.3 give for a bubble inside the resin at equilibrium:

$$C_s = C_\infty \rightarrow P_w = RH_0 P_w^* \tag{4.5}$$

If the partial pressure of water vapor inside the bubble, P_w, is less than given by the equation above, bubble growth occurs. The standard water vapor pressure at ambient temperature is only a few percents of atmospheric pressure. Therefore, the partial pressure of water vapor inside the bubble is very low at room temperature.

The standard water vapor pressure, P_w^*, increases exponentially with temperature, refer to Equation 2.2. Equilibrium can be restored if water diffuses into the bubble, thereby increasing α_w and P_w. This path toward equilibrium results in stable bubble growth. Stable bubble growth during heat-up and isobaric conditions continues until the molar fraction of water, α_w, approaches 1. When $\alpha_w = 1$, bubble growth becomes unstable or non-equilibrium.

By combining Equations 4.1 and 4.5, the relationship between the gas pressure inside the bubble, P_g, and the equilibrium state of water solution is:

$$P_g = \frac{RH_0}{\alpha_w} P_w^* \tag{4.6}$$

where, in the absence of viscous and capillary effects $P_g = P_r$, Section 2.2.2. Since resin pressure is an important processing parameter, the gas pressure inside the bubble is presented as resin pressure in the rest of the chapter. A plot of the resin pressure P_r versus temperature can be used to identify the regions of stable and unstable growth. Figure 4.2 shows an example of such a plot for a resin conditioned at a relative humidity of 75%. Three paths are marked in this figure to explain

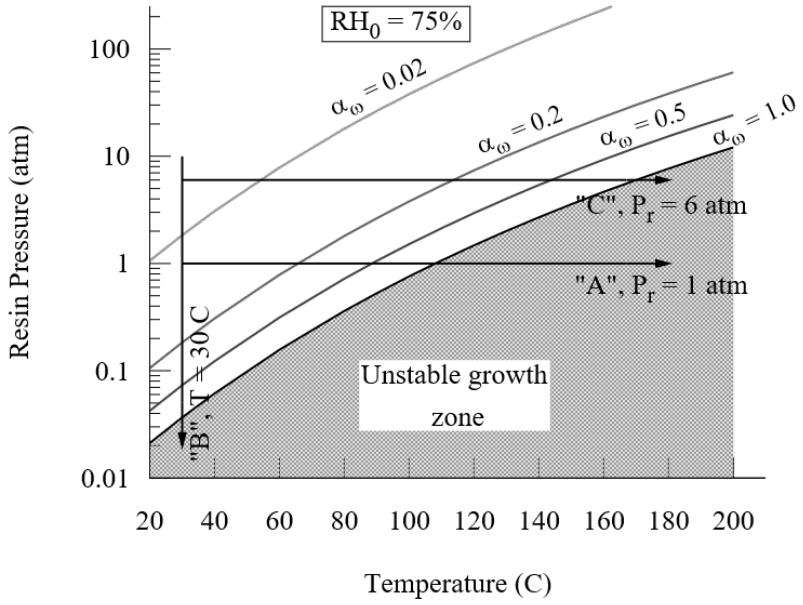

Figure 4.2: Equilibrium diagrams of water molar fraction (α_w) in a bubble with air content of ($1.0 - \alpha_w$) at different resin pressure and temperatures. This diagram is related to the resin conditioned at a relative humidity of 75%. Paths "A", "B", and "C" are used to explain the application of the diagram in the text, Section 4.1.1.

the application of a $P_r - T$ plot with respect to bubble growth control via manipulating process parameters.

Path "A" shows an example in which resin initially experiences 1 atm pressure at 30°C. By increasing the temperature under isobaric conditions, the equilibrium molar fraction of water increases. This drives the solute from the matrix into the bubble to increase the current molar fraction and restore the equilibrium state. Specifically, the relative saturation becomes greater than one and moisture diffuses into the bubble. The plot shows that this process causes an increase in molar fraction of water in the bubble and a stable bubble growth until a temperature of approximately 108°C. With temperature increase beyond this point, vapor pressure equilibrium cannot be established and unstable bubble growth will occur.

In the case of path "B", resin pressure reduces under isothermal condition. Similar to the previous case, the pressure drop results in moisture diffusion into the bubble to compensate for the increase in equilibrium water vapor molar fraction. This continues until a resin pressure of approximately 0.02 atm where bubble growth enters into the unstable zone. Path "C" shows how effective high resin pressure is to suppress moisture-driven bubble growth. In comparison with path "A", increasing the resin pressure from one to six atmosphere leads to bubble shrinkage through moisture diffusing out of the bubble. This is demonstrated by the decrease in water molar fraction inside the bubble. Furthermore, the solute diffusion-driven shrinkage is accompanied by a volume shrinkage due to ideal gas law. At this pressure, the bubble is expected to grow stably until a temperature of approximately 170°C. Practically, resin pressure can be controlled with the processing equipment such as an autoclave.

Previously, Wells [35] provided experimental evidence for both stable and unstable moisture-driven bubble growth in MTM45-1 epoxy resin. His results showed that by increasing temperature or decreasing pressure, bubble growth takes place. Furthermore, an interesting observation based on the reported results is that if temperature and pressure are not in the critical region of unstable growth, equilibrium can be restored and the growth is stable and limited.

The transition between stable and unstable bubble growth is given by Equation 4.6 and setting the molar fraction of water to 1. The plot in Figure 4.3 displays the boundary for this transition with resin pressure, P_r, divided by the initial relative humidity RH_0 on the y-axis versus temperature on the x-axis. By using this plot, the critical resin pressure or temperature that triggers unstable growth for any RH_0 can be determined graphically. For example, if the initial relative humidity is 75% and the resin pressure is 1 atm, the figure shows that stable bubble growth is expected until a critical temperature of approximately 108°C is reached.

In the case that cure temperature is 177°C, Figure 4.3 demonstrates that a P_r/RH_0 of approximately 10 atm is required to prevent unstable bubble growth. A process engineer can also consider

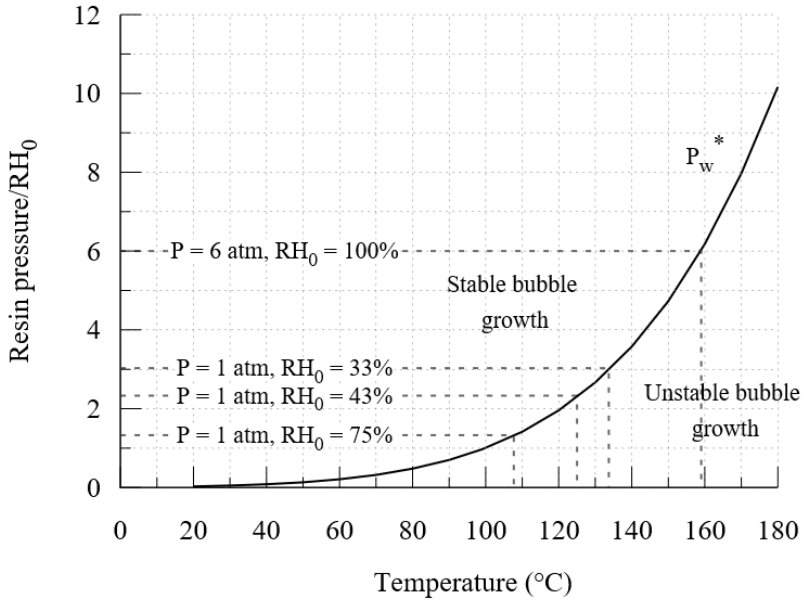

Figure 4.3: Plot used to determine pressure and temperature conditions for stable and unstable moisture-driven bubble growth according to Equation 4.6.

the availability of the required facility. For example, if the maximum autoclave pressure is 5 atm, the initial relative humidity must be less than 50%, to be able to ramp up the temperature to 177°C without concern for unstable moisture-driven bubble growth.

Since the initial composition of an air-water bubble entrapped in a resin matrix is mainly air, stable bubble growth with any temperature increase or pressure decrease is inevitable. The extent of the stable bubble growth can be determined by considering a bubble initially at equilibrium state and calculating the change in its size relative to the initial state.

Pressure or temperature variation disrupts the equilibrium and causes solute diffusion. The resulting solute transfer changes the partial pressure of the vapor inside the bubble. Using the ideal gas law, the variation of the air molar fraction, α_a, with temperature, resin pressure, and bubble radius R_b is:

$$\alpha_a = (1 - \alpha_w) = (1 - \alpha_{w,0}) \left(\frac{P_{r,0} T}{P_r T_0} \right) \left(\frac{R_{b,0}}{R_b} \right)^3 \tag{4.7}$$

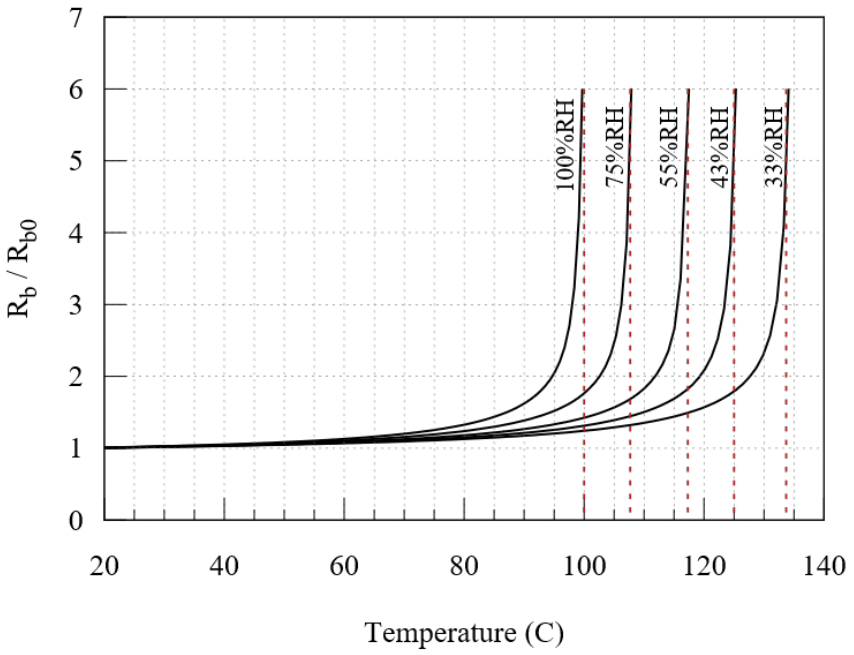

Figure 4.4: Calculated equilibrium bubble radius for a resin pressure $P_r = 1$ atm at different relative humidity levels. Vertical dashed lines show the critical temperatures for unstable bubble growth, Equation 4.5.

In this equation, the subscript "0" denotes the initial state of the corresponding variable. This equation includes the effect of both diffusion-induced and ideal gas law-driven bubble size variation. By incorporating Equation 4.6 into Equation 4.7:

$$\left(\frac{R_b}{R_{b,0}}\right)^3 = \frac{1-\alpha_{w,0}}{\left[1-\mathrm{RH}_0\frac{P_w^*}{P_r}\right]}\frac{P_{r,0}T}{P_rT_0} \tag{4.8}$$

Figure 4.4 illustrates the application of Equation 4.8 in predicting stable bubble growth as a result of temperature increase for different initial relative humidity levels. In this test case, the initial temperature is set to 20°C and the pressure is constant at 1 atm. The red dashed lines in this figure correspond to the calculated critical temperature for unstable bubble growth at each humidity level.

Important interpretations can be made using Figure 4.4 and with respect to manufacturing process design. Primarily, it can be understood that stable growth becomes significant when the temperature is very close to the unstable growth criteria. Generally, the initial bubbles grow only two times relative to their initial size when resin temperature is $\sim$5°C away from the critical temperature. Moreover, the maximum bubble growth in the stable growth zone is 6 times of the bubble's initial size. An example to put this statement in context is a large bubble with a radius of $50\mu m$ that would grow to a radius of $300\mu m$, prior to entering the unstable growth zone. With regards to the resin in prepregs, the initial bubble size is typically much smaller than $50\mu m$ [35]. Additionally, isolated voids in the resin contribute to less than 0.2% of the total porosity [50]. Therefore, stable bubble growth has negligible effect in the context of porosity control in composites manufacturing. This explains the trend in the literature that rarely discusses the growth of an initially-air-filled bubble.

The analytical approach discussed in this section provides a generalized and practical framework to calculate the critical temperature for unstable bubble growth. In the context of composites manufacturing, the process parameters can be optimized to avoid moisture-driven porosity by not exceeding the critical temperature. Another aspect of the application of the analytical approach in manufacturing is that bubble growth can take place while the resin is in the viscous liquid state. Therefore, bubble growth is not expected after resin reaches gelation, even with cure temperature exceeding the critical values calculated based on the moisture content of the resin. In the following section, an experimental investigation is presented to confirm the validity of the analytical approach for suppressing moisture-driven bubble growth and its application in composites manufacturing.

4.2 Experiments

4.2.1 Material

The experimental work for validation of the criteria for unstable bubble growth used coupons of Cytec MTM45-1 neat resin film. MTM45-1 is a toughened epoxy resin system [32]. The coupons

measured approximately 2000 mm^2, 0.19 mm thickness, and were moisture conditioned in accordance with the ASTM E104−2 standard [121] for five days and at an ambient temperature of 22±1°C. Four levels of initial relative humidity RH_0 were chosen for the experiments: 0, 33, 43 and 75%, and two repeat tests were performed at each humidity level.

To study the effect of fibers on bubble growth initiation criteria, prepreg coupons were used. Every experiment in this part used a single ply of a partially-impregnated woven prepreg, MTM45-1/5HS CF2426A by Cytec Solvay. This is a net resin, one-side-coated, out-of-autoclave-grade prepreg. Uncured prepreg plies have an initial thickness of 0.5±0.05 mm. The resin weight fraction is 36% giving a theoretical density of 1.495 g/cc for a porosity-free, cured prepreg [14]. Coupon size and the conditioning method were similar to the case of neat resin samples.

The material characterization and model development by Shahkarami and Van Ee [21] for MTM45-1 resin system were employed. MTM45-1 cure kinetics and viscosity models have been developed based on extensive DSC, TGA, and rheometry testing. The cure kinetics model used is:

$$\frac{dx}{dt} = \sum_{i=1}^{2} k_{eff,i}(1-x)^{l_i}\left(\frac{1}{r_i}-x\right)^{m_i}(x^{n_{2,i}}+b_i)^{n_i} \tag{4.9}$$

In this equation, all the parameters with subscript "*i*" are fitting parameters, x is the degree of cure, and t is time variable. The viscosity model has the form:

$$\mu = \mu_1(T) + \mu_2(T)\left(\frac{x_g}{x_g - x}\right)^{(A+Bx+Cx^2)} \tag{4.10}$$

In this equation, μ is dynamic viscosity, x is degree of cure, x_g is the degree of cure at gelation point, and the rest of the parameters are found by fitting the model against rheometry tests. These models are implemented in the commercial Raven software [22].

4.2.2 Experimental setup

Bubble growth tests were conducted by placing the samples on a 6 mm thick borosilicate glass tool to enable real-time in-situ visualization of the bubble behavior through the tool, Figure 4.5. Prior to every bubble growth test, the glass tool was cleaned and coated with a layer of FREKOTE 700-NC release agent. A Keyence VHX-1000 digital microscope at 50X magnification was used to capture and record the bubble behavior. The samples were heated using a HEATCON heating pad placed on top of the sample, controlled by a thermocouple placed on the glass tool, close to the edge of the sample.

Prior to heat up, tacky tape was placed along the perimeter of the sample to prevent resin flow. Subsequently, the sample was covered with a layer of release film, Non-perforated Fluorinated Ethylene Propylene (FEP) release-film (A5000 by Cytec). The release film placement aimed to minimize the amount of gas escaping from the sample to the vacuum system during cure. The amount of air entrapped during the sealing process was minimal. However, the as-received resin film contained some bubbles prior to cure. The amount of the initial air was more noticeable in the case of the prepreg coupons that included dry fiberbed regions. A 0.5mm thick caul-sheet, consisting of two layers of precured carbon/epoxy laminates, was placed on top of the release film to uniformly transfer the vacuum-bag-imposed pressure to the sample. The heating pad and vacuum bag were placed on top of this setup. A vacuum pressure of 0.1 kPa was applied during the entire test, resulting in a net pressure on the setup, and thereby resin pressure, very close to one atmosphere.

During the bubble growth tests, synchronized recordings of temperature and digital microscopy images, recorded at 15s intervals, provided information of resin temperature and bubble size during the heat-up and cure process. A magnification of 50X was used to cover a resin area of approximately 3mm$\times$3mm to be able to track several bubbles simultaneously.

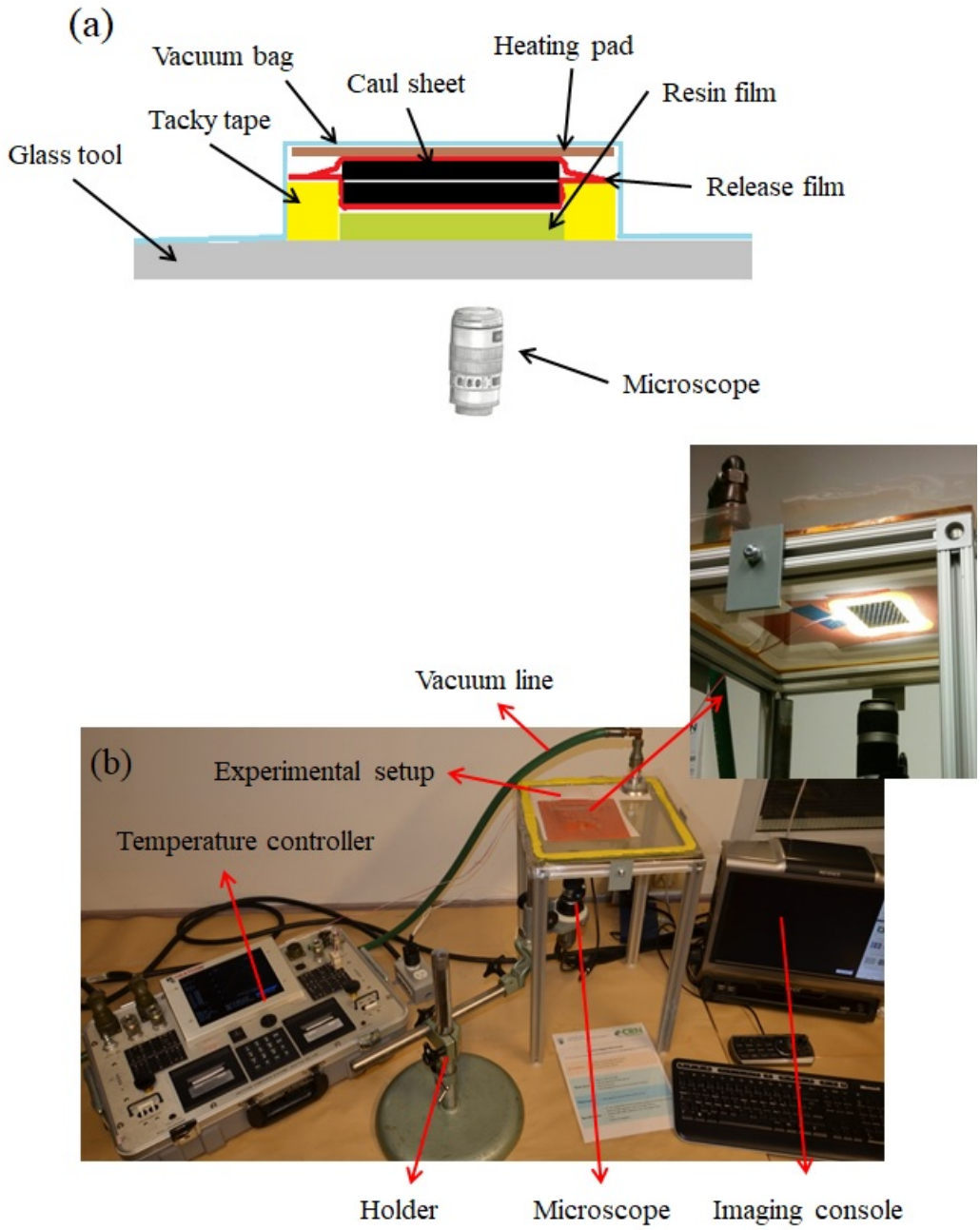

Figure 4.5: Experimental setup for in-situ monitoring of bubble behavior; a) Schematic of the test sample and bagging, b) Temperature control and digital microscopy setup.

4.2.3 Cure cycle design

Two types of cure cycles were used in the experiments. The first type, "standard cycle" was a straight heat-up ramp at 2.2°C/min to the final cure temperature of 180°C. This standard cycle was used to measure unstable bubble growth as a function of temperature at a constant resin pressure of one atmosphere.

The second type of cure cycle was a "designed cycle" that consisted of a temperature ramp at 2.2°C/min to a pre-calculated temperature. This temperature was set to the critical temperature for unstable bubble growth at any specific conditioning humidity level. Consequently, a cure cycle that remains below the critical temperature is expected to suppress moisture-induced bubble growth and porosity. The initial temperature ramp was followed by an intermediate hold. The duration of this hold was determined based on the time required to gel the resin at any specific cure temperature. Subsequently, the temperature was increased to the final hold temperature of 180°C to achieve full cure. Both sets of experiments used coupons from the same batch that were conditioned simultaneously in the same container.

In the case of the "designed cycles", the appropriate hold temperature to suppress unstable bubble growth was determined using Equation 4.6 with $\alpha_w = 1$, or equivalently Figure 4.3, for different initial relative humidity levels. The critical temperatures with a resin pressure P_r of 1 atm and initial relative humidity levels of 0, 33, 43, and 75%, are infinity (i.e. no unstable bubble growth expected), 134, 125, and 108°C, respectively. The three last temperatures were used as hold temperatures for the moisture conditioned samples.

Determination of the intermediate hold length requires knowledge about the resin's cure kinetics and rheology. Based on material characterization outlined in Section 4.2.1 for MTM45-1 resin system, the commercial software RAVEN [22] was used to determine the gelation time at any specific cure temperature. The results were 60, 95, and 260 min for hold temperatures of 134, 125, and

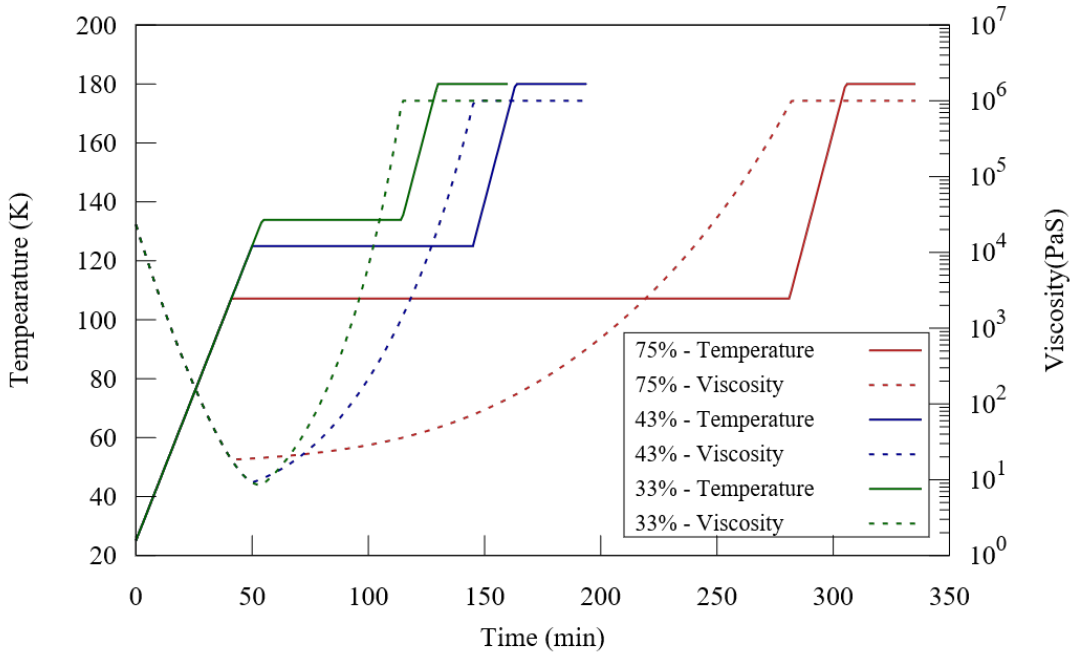

Figure 4.6: Designed cure cycles to suppress moisture-driven bubble growth. An intermediate hold is introduced below the critical temperature for unstable bubble growth. The length of the hold is designed to gel the resin prior to increasing the temperature.

108°C, respectively. Figure 4.6 shows a plot of the three designed cycles including temperature and viscosity graphs. The plateau in the viscosity graph represents the gelation point.

4.3 Results and discussion

4.3.1 Standard cycles

Standard cure cycles were used in order to confirm that the initiation of unstable bubble growth follows the analytically calculated values. Figure 4.7 shows an example of microscopy images from the test with the resin conditioned at 75% RH. In this case, initially, no traceable bubble exists in the frame captured by the camera. When the temperature reached about 113°C, small bubbles appeared in the resin. These small bubbles continued growing rapidly as a sign of unstable bubble growth.

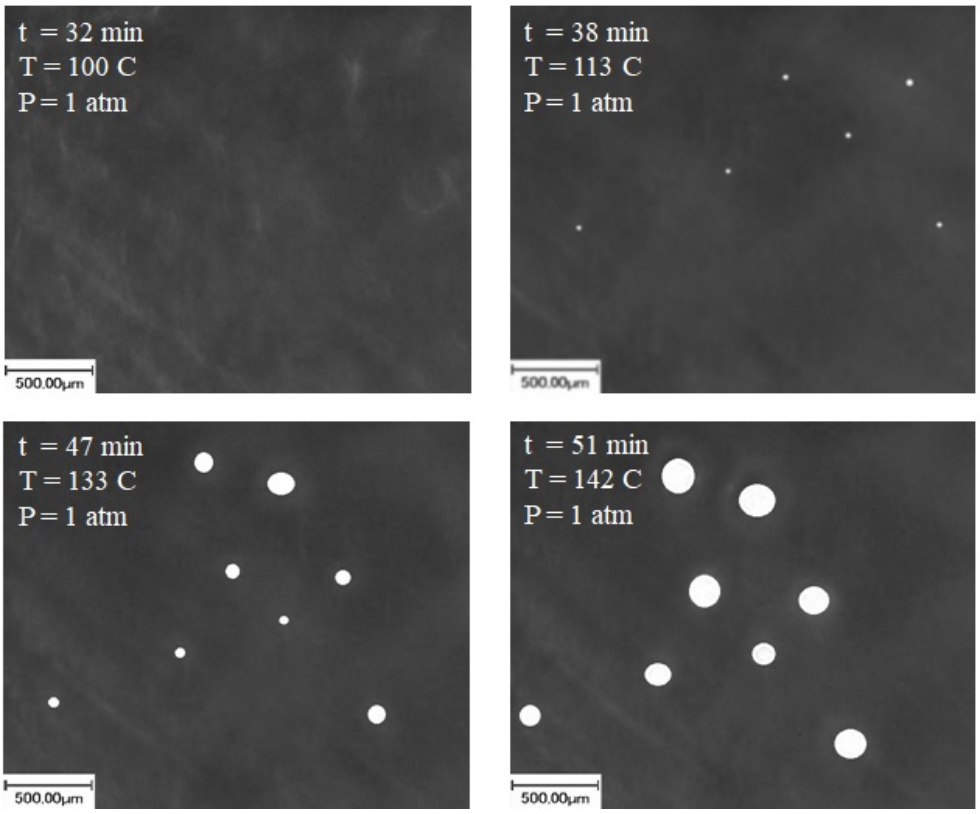

Figure 4.7: Time-lapse images during the cure cycle for a sample conditioned at RH_0 = 75%, cured by a straight heat-up ramp to 180°C. Bubbles are shown in white for improved clarity.

The calculated critical temperature for unstable bubble growth for a sample conditioned at $RH_0 =$ 75% is 108°C.

Figure 4.8 shows the movement of the bubbles inside the recorded image frame. This movement is due to the formation and growth of the bubbles inside a confined geometry accompanied by the low viscosity of the resin at increased temperatures. The present study investigates the arrest of any bubble growth. However, in a broader context, this observation demonstrates bubbles' ability to move inside the resin.

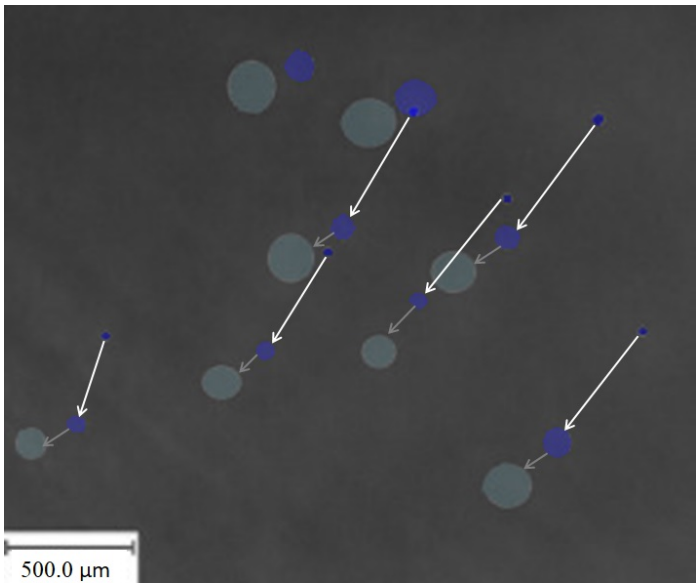

Figure 4.8: An overlay of the results in Figure 4.7 showing the relocation of the bubbles inside the resin upon reaching the critical temperature.

A general trend in the results is that before heat-up, small pre-existing bubbles were present within the resin, e.g. Figure 4.9. The volume fraction of these bubbles was much less than one percent. The preexisting bubbles ranged in size from about 30 to 100 μm in diameter. Furthermore, in the early stages of heat-up, no noticeable change in bubble size was observed from the microscopy images.

Figure 4.10 shows an example of time-lapse imaging related to the resin film conditioned at $RH_0 = 43\%$. In this test, two preexisting bubbles were detected, highlighted by blue and red arrows. The large bubble's diameter exceeds the thickness of the resin film that is about 0.19 mm, therefore, it has been discarded. The small preexisting bubble demonstrates the correlation between the critical temperature and initiation of bubble growth. When the temperature reached the critical value, initiation and rapid growth of the bubble was observed. Similar behavior was observed in other tests including preexisting bubbles, except the tests that used desiccated samples, i.e. $RH_0 =$

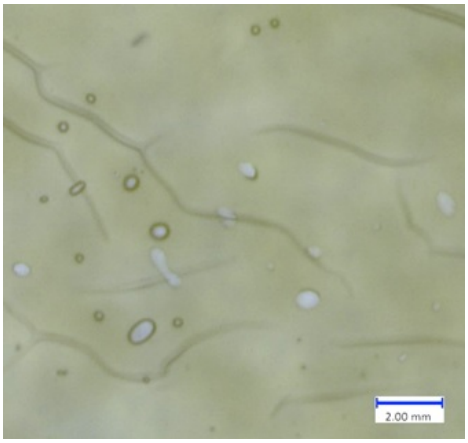

Figure 4.9: Initial state of the resin film before cure showing preexisting bubbles

0%. Table 4.1 summarizes the observed critical temperature for bubble growth versus the calculated values.

Table 4.1: Critical bubble growth temperature, calculated from the model (Equation 4.6), and observed in standard cycle experiments using neat resin film samples.

RH_0	75%	43%	33%	0%
Calculated (°C)	108	125	134	∞
Measured (°C)	113±2	128±2	134±2	N/A

4.3.2 Designed cycles

The designed cycles, Figure 4.6, were used to cure samples conditioned at 33, 43, and 75% relative humidity. No bubble growth was detected for any of the samples during or after the tests. This demonstrates several things. First, by not exceeding the calculated critical temperature during the intermediate hold, unstable bubble growth can be suppressed by holding the resin at an elevated temperature for an extended period. Second, gelation of the resin acts to suppress unstable bubble growth by mechanically constraining the bubbles from growing despite a high initial moisture con-

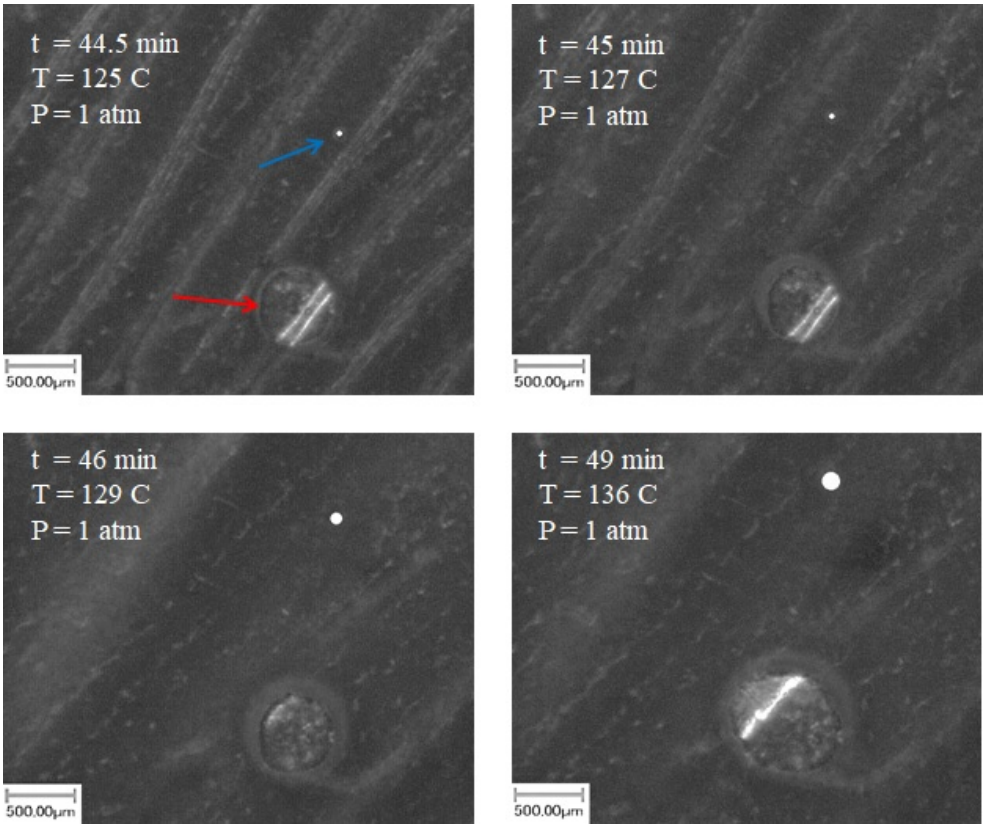

Figure 4.10: Time-lapse images during the cure cycle for a sample conditioned at RH_0 = 43%, cured by a straight heat-up ramp to 180°C. The parallel-line pattern in the background is only a reflection of the release film on which resin is placed on.

tent of the resin. Third, the experiments showed that we can design cure cycles to suppress bubble growth entirely by analytical means.

4.3.3 Porosity in cured samples

The initiation or arrest of bubble growth in the present study was examined through microscopy. However, after each test, the related samples were removed from the test setup and evaluated for the extent of porosity evolution throughout the whole sample. The objective was not to quantify the amount of porosity but to establish whether moisture driven bubble growth had occurred in the sample. In samples where no bubble growth was observed in-situ during cure, a limited number

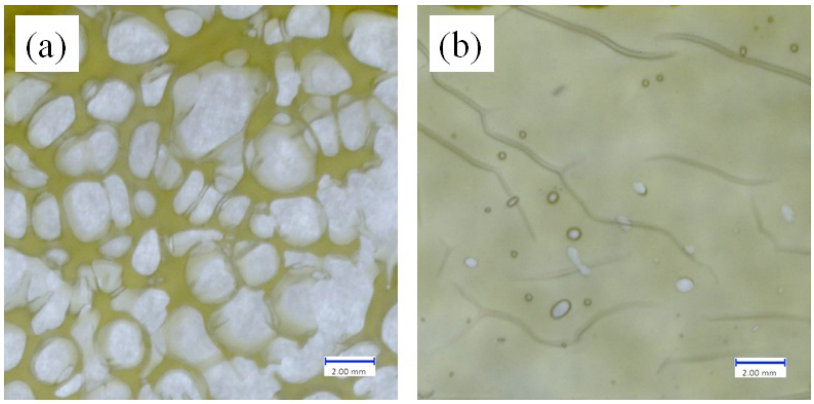

Figure 4.11: Images of cured samples conditioned at RH_0 = 75%. a) Standard cycle resulted in a highly porous test sample, b) The designed cycle resulted in no observable moisture-driven bubble growth. The voids seen in b) were pre-existing and did not grow appreciably during the test.

of voids are detected, similar to the initial state of the uncured resin samples. In samples where bubble growth was observed in-situ, large voids distributed throughout the sample were observed at a macroscopic scale. Figure 4.11 shows an image of two samples after cure, both conditioned at $RH_0 = 75\%$, one cured with a standard cycle and another with a designed cycle.

Note that the samples were bagged so that there was limited ability for any gas generated during cure to escape the samples. This exacerbates the amount of porosity found in the cured samples compared to the normal practice of curing prepreg-based laminates. When curing a prepreg laminate using the same resin and humidity conditioning, moisture can be extracted through transport out of the laminate prior to gelation of the resin. Moisture transport to the outside of the laminate lowers the moisture content in the resin, hence increases the critical temperature for unstable bubble growth.

The sample thickness was measured to qualitatively measure the porosity level. Given that the starting film thickness was the same for all samples, any thickness increase in the cured samples was approximately proportional to the level of porosity. The thickness increase also confirms that bubble growth in that specific experiment occurred. Table 4.2 shows the measured average cured sample thickness for the seven test conditions used in this study. The thickness of all samples cured

Table 4.2: Measured average sample thickness after cure for moisture conditioned samples cured using standard and designed cure cycles.

$\mathbf{RH_0}$	75%	43%	33%	0%
Standard cycle (mm)	1.22	1.49	1.11	0.38
Designed cycle (mm)	0.38	0.37	0.38	–

using designed cycles was within $\pm 2\%$ of the desiccated sample's thickness, supporting the visual observation of no porosity in any of these samples. In all other samples, the cured thickness was significantly greater, supporting the observation of significant porosity and affirming that bubble growth occurred.

4.3.4 Moisture conditioned prepreg experiments

Similar to the experiments using neat resin film coupons, two sets of experiments were conducted using conditioned prepreg samples. The intermediate hold temperature and time were set as presented in Figure 4.6. Figures 4.12 and 4.13 show time-lapse images in the case of prepreg coupons conditioned at $RH_0 = 75\%$, and cured using standard and designed cure cycles, respectively. It is observed that if the resin temperature exceeds the calculated critical temperature significant bubble growth occurs. However, introducing an intermediate temperature hold prevented moisture driven bubble growth.

A major difference between the prepreg and neat resin samples is that prepreg samples contain high level of initial entrapped air. Fundamentally, this is not expected to change the resin behavior with respect to bubble growth. However, entrapped air expansion due to heating and resin infusion into fiber tows obstructed detecting the critical point for moisture-driven bubble initiation. Nonetheless, the bubble growth progress was clearly traced, as shown in Figure 4.12, in the cases where it occurred.

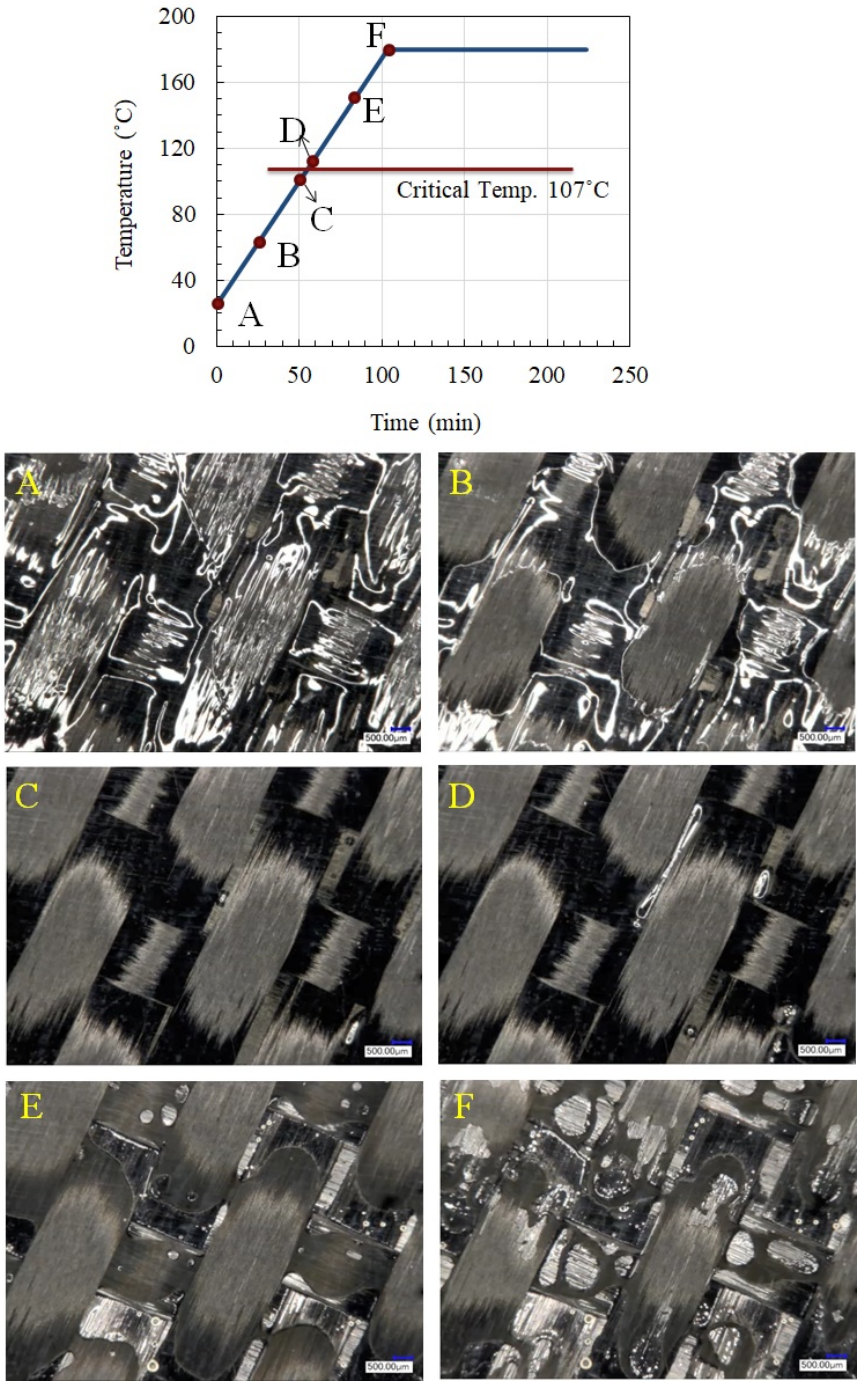

Figure 4.12: Time-lapse images of the prepreg ply conditioned at 75%RH and cured using a standard cure cycle. Images show appearance and growth of bubbles when the cure temperature exceeds the critical temperature for moisture-induced bubble growth.

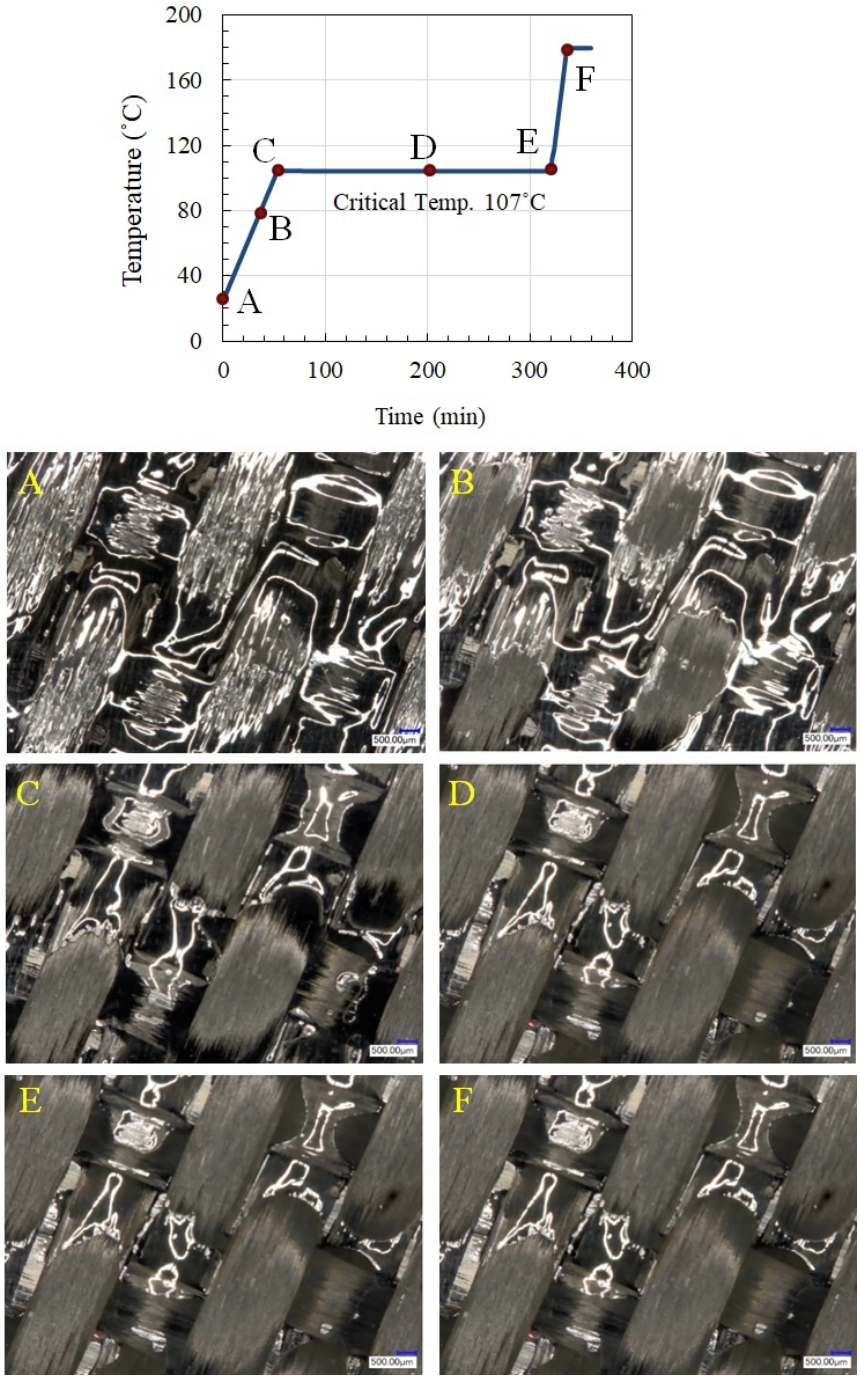

Figure 4.13: Time-lapse images of the prepreg ply conditioned at 75%RH and cured using a designed cure cycle. Moisture-induced bubble growth suppression is demonstrated by no bubble formation and growth observed in images C to F.

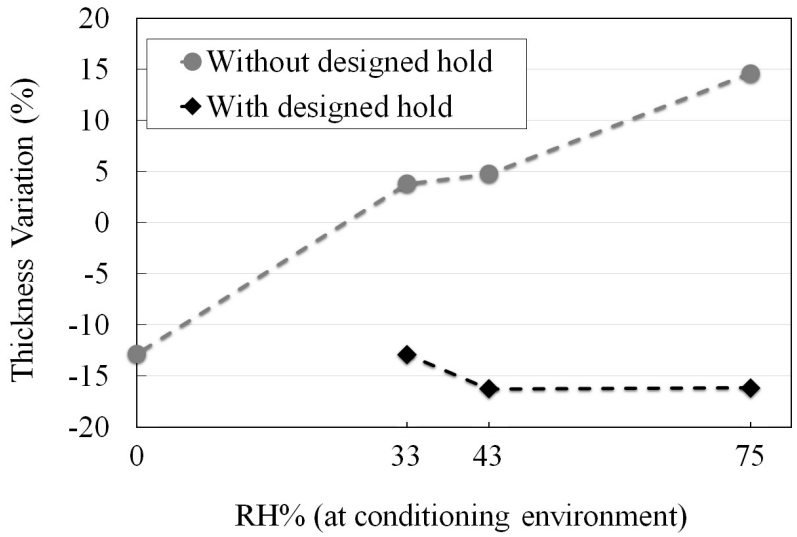

Figure 4.14: Variation of the prepreg ply thickness upon cure with and without designed intermediate hold. Initial thickness of the prepreg plies $= 0.55 \pm 0.02$mm.

The initial thickness of the prepreg plies was compared to the final thickness after cure to evaluate the ability of the designed cure cycles in preventing bubble growth in the presence of fibers. The initial prepreg ply thickness is similar in all tests, 0.55 ± 0.02mm. Figure 4.14 shows the variation of the initial thickness after cure. In the case that the prepreg is desiccated, i.e. $RH_0 = 0\%$, the final thickness reduces about 15%. This thickness reduction was not expected due to the experimental setup used that prevents gas transport to the outside of the system. However, partial infiltration of the resin into the dry fiberbed is a possible explanation for this thickness reduction. The partial resin infiltration is assisted by the pressure imposed on the sample through the vacuum bag as well as the low viscosity at increased temperatures.

A similar level of thickness reduction was observed in the case of samples conditioned at increased levels of humidity and cured using designed cure cycles. This shows that the intermediate hold neutralized the effect of dissolved moisture and eliminated bubble growth. In the case of samples cured without an intermediate hold, the final thickness increased. Thickness increase

was proportionate to the conditioning humidity level. This is evidence for initiation and growth of moisture-induced bubbles.

4.3.5 A note on diffusion timescale

Based on the discussion in Section 2.2.1, the moisture concentration in the resin is equal to the vapor (gaseous state of moisture) concentration in a preexisting bubble inside the resin, i.e. $C_s = C_\infty$, at the equilibrium state. A fundamental assumption with regards to bubble growth has been that any temperature-increase leading to $C_s < C_\infty$ would cause instantaneous bubble growth. Consequently, the cure temperature during experiments was set to the critical temperature above which this criteria holds.

Instantaneous bubble growth is equivalent to instantaneous moisture diffusion into the bubble. This is a conservative assumption since a diffusion timescale slower than the normal processing timescale delays bubble growth, or increases the temperature required to initiate bubble growth.

According to the Equation 2.7, the timescale for diffusion (t_d) around a spherical bubble is:

$$t_d = \frac{R^2}{\pi D} \tag{4.11}$$

where, R is radius and D is moisture diffusion coefficient in the resin. The moisture diffusion coefficient in the uncured resin is between 10^{-11} to 10^{-8} m^2s^{-1} in a temperature range of 0 to 120°C [122, 123]. Cure temperatures used in this chapter were between 100 to 140°C. Assuming a distance of 50 μm away from a bubble and a diffusion coefficient of 10^{-8} m^2s^{-1}, the timescale for moisture diffusion is about 0.08 s. This is much faster than the normal processing timescale, e.g. MTM45-1 resin gels after 100 min cure at 120°C. This simple check demonstrates that the assumption of instantaneous diffusion in the present experimental work is realistic.

Reports in the literature show moisture diffusivity in the resin reduces with cure progress [124], resulting in increased diffusion timescale. Cure progress and the resulting viscosity development

however, also constrains the bubble dynamics [39]. The interaction between diffusion, cure, and bubble dynamics mechanisms is beyond the scope of the present study.

4.4 Summary

The work presented in this section showed how simple and established theories for moisture saturation, diffusion and the behavior of air-water mixtures can be used to calculate the resin pressure and temperature conditions to avoid unstable moisture driven bubble growth. The criteria for unstable growth predicted the observed temperature for bubble growth within 5°C for a range of moisture conditions. The criteria used for unstable growth relies on simple equilibrium considerations. Therefore, time-dependent effects are not explicitly included such as surface tension, resin viscosity or moisture diffusivity. This makes the developed approach suitable to predict the onset of growth but not the time-dependent evolution.

Furthermore, it was found that an intermediate hold in the cure cycle at a temperature just below the critical temperature and until the resin is gelled can prevent bubble growth. In addition to its practical value, this observation confirms that moisture-induced bubble growth is suppressed by the three-dimensional structure of the resin after gelation.

Chapter 5

Coupled gas/resin transport during cure

5.1 Introduction

Gas and resin transport are important mechanisms with respect to porosity control in composites manufacturing. During cure, the resin viscosity initially drops due to the temperature increase. This allows the resin to become mobile and infiltrate into the fiberbed, hence reducing the porosity. A common assumption at this stage is that gas transport has been completed during the previous debulk stage. However, common scenarios such as deficient vacuum during debulk and remaining gas as well as volatile desorption during cure demonstrate that neglecting gas transport during cure is not always appropriate. Furthermore, pre-mature resin infiltration during elevated-temperature or extended debulk are situations where resin transport during debulk becomes critical. Therefore, a representative transport model should consider gas and resin transport as coupled mechanisms.

An important characteristic to be considered in modeling coupled gas/resin transport is that the geometry of the gas transport channels inside the fiberbed is changing with resin infiltration. During processing, the fiberbed is both saturating and deforming, due to resin infiltration and applied pressure variation during cure, respectively. A simplifying consideration in the present study is that

the applied pressure remains constant, hence the fiberbed does not exhibit deformation during the process.

In both the experimental and analytical parts of the present study, a homogenized model of the fiberbed is considered. This means that the effect of dual-scale permeability is assumed negligible and porosity is defined as the sum of inter-tow and intra-tow voids in the woven prepreg. Experimental measurements of porosity use the density method, which gives the total volume fraction of the voids in the bulk.

The nature of the interaction between resin and gas transport is initially investigated experimentally. Following that, a coupled transport model is developed, and the experimental data is used to validate the model. Finally, the utility of the developed model is examined through parametric test-cases.

5.2 Experiments

5.2.1 Design of experiments

Two sets of experiments were designed to investigate the interaction between gas and resin transport and the effect on porosity: 1) Reduced bag pressure (RBP) experiments, and 2) Increased applied pressure (IAP) experiments. In the RBP experiments, the applied pressure, P_a, on the laminate remains constant (equal to atmospheric pressure) and different levels of reduced bag pressures, P_b, are used. Bag pressure, P_b, is the gas pressure inside the vacuum bag and varies with the application of vacuum, from 1 atm for a vented part, i.e. no vacuum, to 0 atm with the application of perfect vacuum. In the IAP experiments, the bag pressure remains constant (equal to atmospheric pressure) and the applied pressure, P_a, is increased using an autoclave. The IAP experiments are intended to give a net pressure, $P_n = P_a - P_b$, similar to out-of-autoclave conditions without full-vacuum imposed under the bag.

5.2.2 Experimental setup and materials

For all experiments in this study, the partially-impregnated woven prepreg, MTM45-1/5HS CF2426A by Cytec Solvay, was used. The cure kinetics and viscosity models for MTM45-1 resin system are outlined in Section 4.2.1. Permeability of this prepreg system has also been characterized in multiple studies [14, 25, 45, 61] and is employed in the present thesis. The initial thickness of the uncured prepreg is 0.5 ± 0.05 mm. The theoretical density is 1.495 g/cc for the porosity-free, cured prepreg [14].

The main volatile leading to porosity formation in the current material system is dissolved moisture, Section 2.2. Therefore, all prepregs were placed in a silica gel environment for 5 days, prior to layup and cure, to eliminate the possibility of moisture-driven porosity. Cross-ply laminates consisting of four 6.4×30 cm^2 woven plies were laid-up on an aluminum tool. A brief 5-minute initial

debulk was used to compact the lay-up by connecting the vacuum bag to a vacuum source. The vacuum source was disconnected after 5 min and the bag was vented to atmospheric pressure.

The bagging scheme of the parts is shown in Figure 5.1. To promote a 1D gas transport, three edges of the laminates were sealed with tacky tape to avoid in-plane gas transport, except through the breathing edge connected to the vacuum port. Non-perforated FEP release-film (A5000 by Cytec) was placed on top and bottom of the laminates to limit through-thickness gas transport. Care was taken to avoid entrapment of air pockets between the laminate and the release film on top and bottom. Additionally, a strip of tacky tape was placed at 2 cm from the vacuum edge between the laminate and the release film on top of it, to promote gas transport through the laminate. A 5.5 mm thick cork dam wrapped with a breathing sheet (Bleeder Lease B by Airtech) was placed at the edge to avoid edge pinching. The entire setup was then vacuum bagged with Stretch-VAC 2000 nylon sheet.

For all experiments, a 4-hour room-temperature debulk was followed by a cure cycle consisting of a temperature ramp at 1.5°C/min to 120°C, a 4-hour hold, and finally cool-down to room-temperature at 5°C/min. For the regular out-of-autoclave cure cycles in RBP experiments, a Blue-M oven was used. For pressurized cure cycles in IAP experiments, an American Autoclave was used. Bag pressure was controlled using a pressure transducer and a vacuum bleeder, Figure 5.2.

After cure, each laminate was cut into 6 sections along the length of the laminate for porosity measurements. The first section that contains tacky tape close to the edge of the laminate was discarded. The average porosity of the 5 remaining sections was measured using the density method, following ASTM standards [125]:

$$\varphi = \left(1 - \frac{\rho_{exp}}{\rho_{th}}\right) \times 100 \tag{5.1}$$

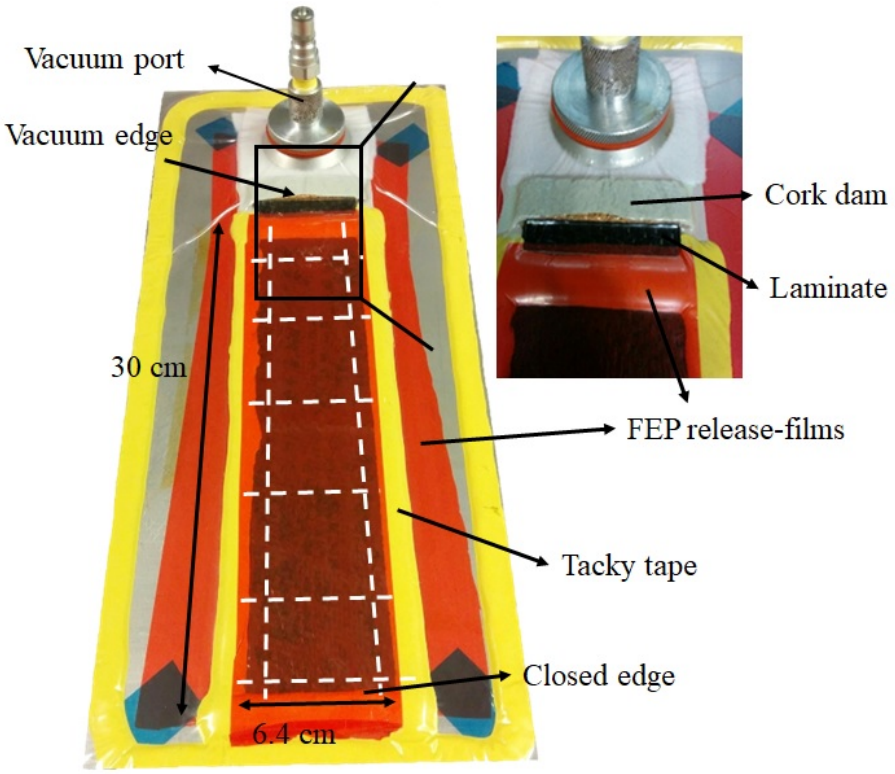

Figure 5.1: Layup and bagging used to promote 1D gas flow. White dashed lines show where samples were sectioned for porosity measurements.

ρ_{exp} is the measured density of the sample and ρ_{th} the theoretical density of a porosity-free laminate. Density was measured using Archimedes' principle, by weighing the sample in air and distilled water.

5.2.3 Experimental results

The experimental test conditions and corresponding measured porosity for RBP and IAP experiments are given in Table 5.1; pressure values are reported in atmospheres (atm), which equals 101.32 kPa in SI units. P_b the bag pressure, P_a the applied pressure, and other important parameters are schematically described in Figure 5.3. Pressure values reported throughout this chapter are the absolute pressure values. Porosity values in this table are average values of measurements based

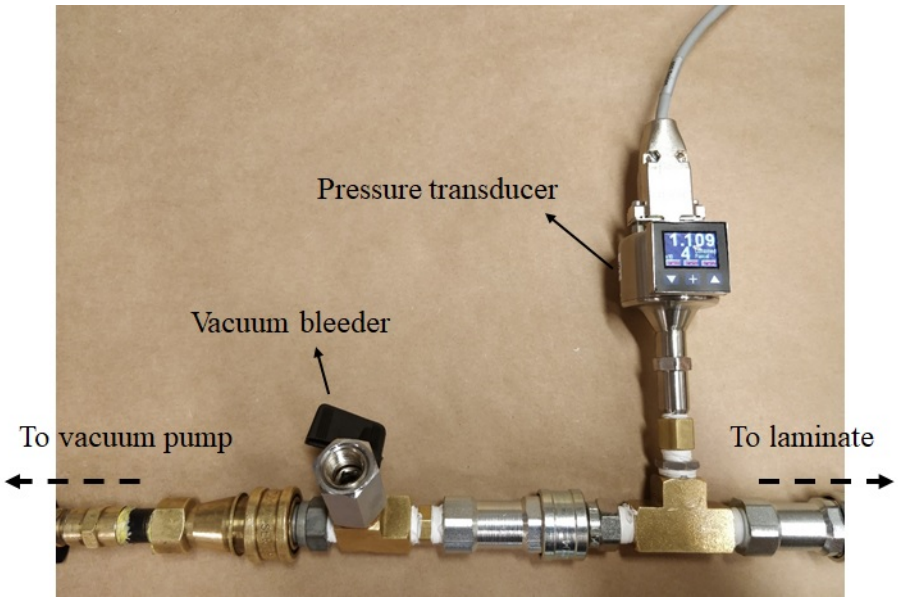

Figure 5.2: Bag pressure control setup for RBP experiments.

on five samples sectioned from each laminate, Section 5.2.2. RBP experiments at $P_b = 0.0$, 0.3, and 1 atm, and IAP experiments with debulk at $P_b = 0.2$ and 1 atm were repeated to confirm the variability of the results. For these repeats, the porosity reported in Table 5.1 is the average of all measurements. The highest density measured was 1.492 g/cc for samples debulked and cured under full-vacuum, i.e. $P_b = 0$, $P_a = 1$ atm. This density was set as the theoretical density of a porosity-free laminate, ρ_{th}, in Equation 5.1. Laminates with $P_a = P_b = 1$ atm during debulk and cure provide an estimate of the initial porosity of the laminates in the present study, 19.7%$\pm$1.2%.

Figure 5.4 shows cross-sectional micrographs of the samples cured under ($P_b = P_a = 1$ atm), ($P_b = 0.43$, P_a 1 atm), and ($P_b = 0$, $P_a = 1$ atm), with corresponding porosity levels of 19.7, 1.1, and 0.0%, respectively. No porosity was detected in the case of the sample debulked and cured under a full vacuum. This validates the use of the density of this sample as a reference for porosity calculation.

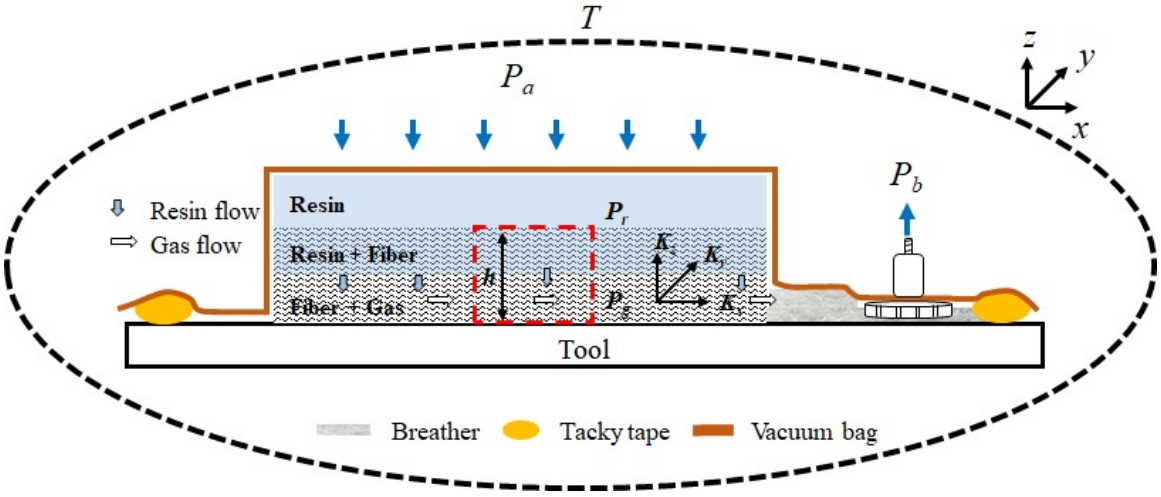

Figure 5.3: Schematic of the structure of a partially impregnated prepreg and the corresponding advection transport mechanisms active during cure. The red dashed line shows the representative volume element (RVE) used in the model development. T: temperature; P_a: applied pressure; P_b: bag pressure; P_r: resin pressure; P_g: gas pressure; K_z: through-thickness permeability (for resin); K_x and K_y: in-plane permeabilities (for gas); h: fiberbed thickness.

The results from the RBP experiments in Table 5.1 show that even with relatively high bag pressures during debulk and cure, i.e. $P_b > 0$, the final porosity is significantly lower than the initial porosity of 19.7%. For instance, the porosity of a sample debulked and cured using $P_b = 0.43$ is 1.1%. A simple analysis shows that this porosity reduction, from the initial 19.7%, is not likely to occur solely due to air removal during debulk. The initial (subscript 1) volume of the gas in the laminate is:

$$V_{g,1} = \varphi_1 V_{th} \tag{5.2}$$

where φ_1 is the initial porosity and V_{th} is the theoretical volume of a porosity-free laminate. After a long debulk, the gas pressure inside the fiberbed, fiber + gas region in Figure 5.3, is in equilibrium with the bag pressure, P_b. If there is no further gas flow out of the laminate after the room

Table 5.1: Experimental test conditions and porosity results for gas/resin experiments.

Test #	Test type	Bag pressure P_b-debulk	Bag pressure P_b-cure	Applied pressure P_a-cure	Density ρ_{exp} (g/cc)	Porosity φ (%)
1	Initial porosity	1	1	1	1.201	19.7±1.2
2	RBP experiments	0.88	0.88	1	1.417	4.8±0.3
3		0.70	0.70	1	1.456	2.4±0.3
4		0.43	0.43	1	1.475	1.1±0.2
5		0.31	0.31	1	1.482	0.7±0.2
6		0.23	0.23	1	1.484	0.5±0.1
7		0.0	0.0	1	1.492	0.0±0.2
8	IAP experiments	1	1	2	1.488	0.5±0.2
9		0.20	1	2	1.483	0.6±0.1
10		0.10	1	2	1.485	0.4±0.2
11		0.0	1	2	1.475	0.5±0.2

temperature debulk, resin flow during heat-up and cure will compress the entrapped gas inside the laminate until the internal gas pressure, $P_{g,2}$, equilibrates with the applied pressure (i.e. $P_{g,2} = P_a$). Consequently, the porosity after cure is:

$$\varphi_2 = \frac{V_{g,2}}{V_{th}} = \varphi_1 \frac{P_b}{P_a} \tag{5.3}$$

In this simplified scenario, we would expect porosity in all laminates that do not have perfect vacuum, $P_b = 0$ atm, under the bag. Comparison of measured porosity for the RBP experiments and the porosity estimated using the simplified analysis above, dashed line in Figure 5.5, shows that porosity estimates are much higher than experimentally measured values. This indicates that additional gas transport occurs after the room-temperature debulk.

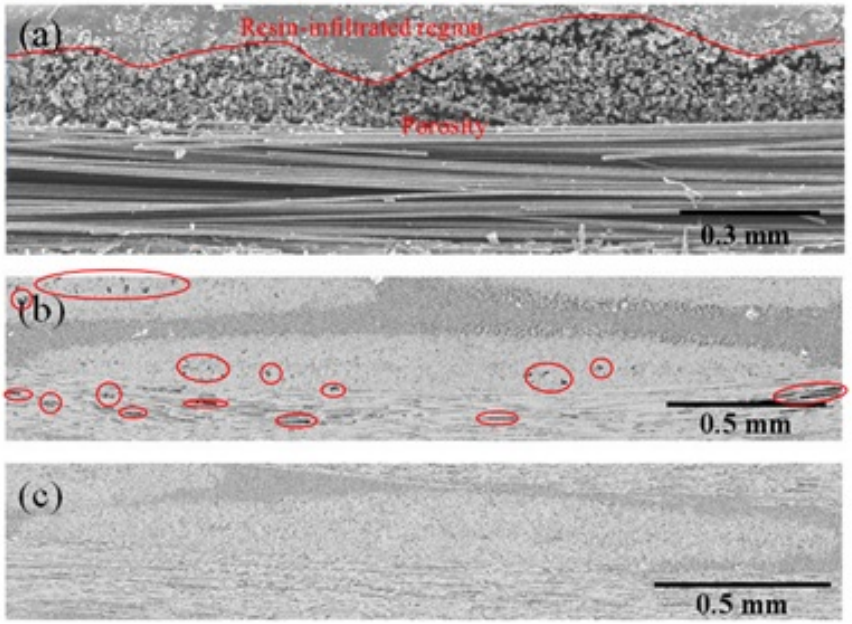

Figure 5.4: Micrographs (SEM images in backscatter mode) showing the cross-section of (a) the initial state of the prepreg, (b) a cured sample with 1.1% porosity, and (c) a porosity-free cured sample. Red lines are highlighting regions with porosity.

The results from the IAP experiments in Table 5.1 show that even with no debulk, $P_b = 1$ atm, porosity decreases from the initial 19.7% to about 0.5%, by increasing the applied pressure on the laminates to $P_a = 2$ atm during cure. This observation is further evidence that resin flow during heat-up and cure promotes gas transport out of the laminate, and that there is a coupling between these two transport mechanisms.

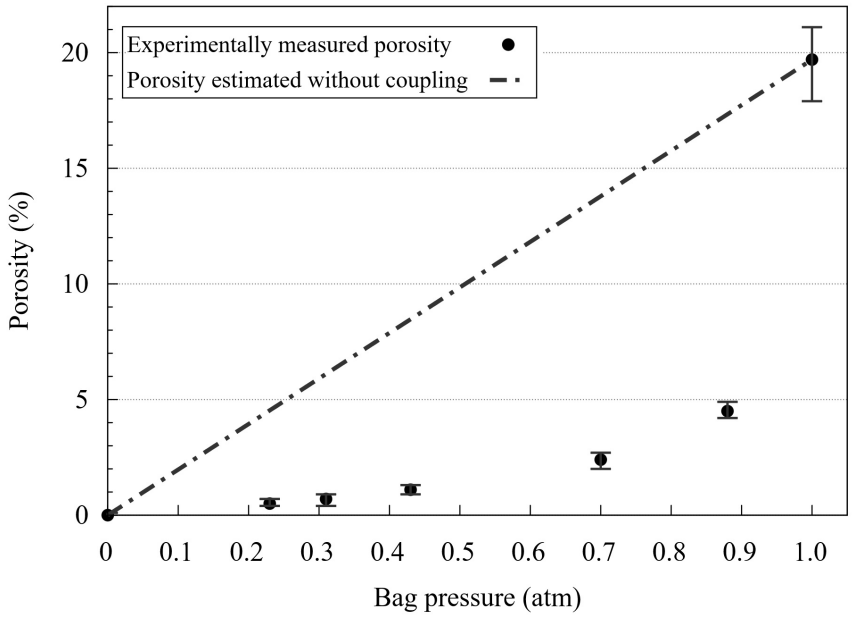

Figure 5.5: Comparison of experimental results and porosity estimated using Equation 5.3.

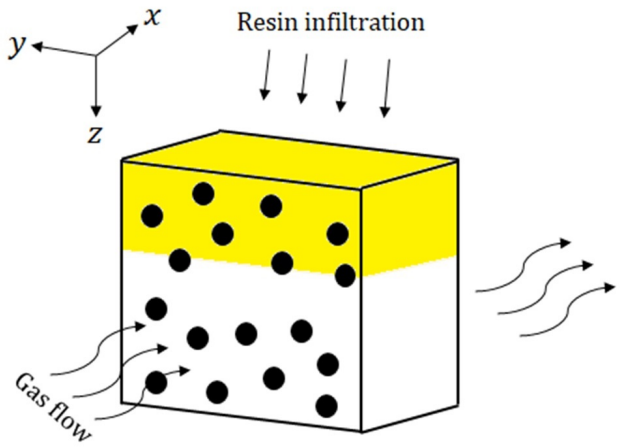

Figure 5.6: Representative volume element (RVE) for coupled transport model. The RVE represents 1D gas transport along the x axis and 1D resin infiltration along the z axis. The RVE refers to the red dashed line element in Figure 5.3.

5.3 Coupled gas/resin transport model

5.3.1 Model development

The Representative Volume Element (RVE) used in the present study is shown in Figure 5.6. This RVE simplifies a multi-ply layup of prepregs to a homogenized unit cell where both through-thickness permeability for resin and in-plane permeability for gas are average values. This approach has been employed in previous studies using the same material system [25, 50].

The continuity equation for the gas phase in the RVE is [91]:

$$\begin{aligned} &\frac{\partial}{\partial t}(\rho_g \varphi) + \nabla \cdot (\rho_g \nu_{g,\xi}) = \dot{m} \\ &\nu_{g,\xi} = (\nu_{g,x},\ \nu_{g,y},\ \nu_{g,z}) \end{aligned} \tag{5.4}$$

where ρ_g and $v_{g,\xi}$ are the density and superficial velocity vector of the gas, respectively. $\dot{m}$ $[\frac{kg}{m^3 s}]$ is a source term for gas generation (e.g. volatile release) and φ is the fiberbed porosity. Using the ideal gas law, the density of the gas phase is:

$$\rho_g = \frac{P_g M_g}{RT} \tag{5.5}$$

M_g is the molecular mass of the gas, T is temperature, and R is the ideal gas constant. The superficial velocity (volumetric flow rate/unit area) of the gas based on the Darcy flow model is:

$$\begin{aligned} v_{g,\xi} &= \frac{-K_\xi}{\mu_g}\frac{\partial P_g}{\partial \xi} \\ \xi &= x,\ y,\ z \end{aligned} \tag{5.6}$$

μ_g is the gas viscosity and K_ξ is fiberbed permeability in each principal direction. By incorporating Equations 5.5 and 5.6 into Equation 5.4:

$$\begin{aligned} \frac{\partial}{\partial t}(P_g\varphi) - \left[\frac{\partial}{\partial x}\left(\frac{K_x P_g}{\mu_g}\frac{\partial P_g}{\partial x}\right) + \frac{\partial}{\partial y}\left(\frac{K_y P_g}{\mu_g}\frac{\partial P_g}{\partial y}\right) + \right. \\ \left. \frac{\partial}{\partial z}\left(\frac{K_z P_g}{\mu_g}\frac{\partial P_g}{\partial z}\right)\right] = \dot{m}\left(\frac{RT}{M_g}\right) \end{aligned} \tag{5.7}$$

R, T, M_g, and μ_g are considered constants in the present model. This is a general form of the gas transport equation in a 3D RVE. However, considering the physical characteristics of the current prepreg, gas transport through-thickness is negligible due to the resin-rich layer on the prepreg surface. Furthermore, considering the 1D experimental gas flow setup in this study, gas transport can only occur along the length of the laminate. Therefore, the y and z components of the gas pressure gradients are effectively equal to zero. Furthermore, by eliminating the desorption of dissolved species, moisture in the present case, $\dot{m} \approx 0$. Resin infiltration changes the volume fractions in the RVE, thus porosity. By considering φ as a time-dependent variable and accounting for the above assumptions, Equation 5.7 becomes:

$$\varphi \frac{\partial P_g}{\partial t} + P_g \frac{\partial \varphi}{\partial t} = \frac{\partial}{\partial x}\left(\frac{K_x}{\mu_g} P_g \frac{\partial P_g}{\partial x}\right) \tag{5.8}$$

At low gas pressures, the average distance that a gas molecule travels before colliding with another gas molecule, or the mean free path, increases due to the reduced number of molecules in a constant volume of space. This increase continues until the mean-free-path becomes comparable with the diameter of the containing channel. In this condition, the no-slip boundary condition does not hold, and the flow is faster than the Darcy flow model would predict. This is know as Klinkenberg effect. The permeability term can be corrected for the Klinkenberg effect [63]:

$$K_x = K_{x,0}\left(1 + \frac{b}{P_g}\right) \tag{5.9}$$

where b is Klinkenberg parameter and $K_{x,0}$ is initial permeability or permeability under a constant applied pressure.

As for the gas transport equations, the continuity equation for the resin phase can be simplified based on the physical characteristics of the prepreg RVE. The components of resin velocity in x and y directions are negligible since the ratio of the width/length to thickness in a prepreg ply is normally about 10^4. Additionally, because of the location of the resin film on top of the gas-occupied fiberbed, only the z component is relevant to the resin/gas transport interaction. The resin velocity along z-axis can be estimated by Darcy flow model:

$$\hat{v}_{r,z} = \frac{-K_z}{\mu_r(1 - V_f)} \frac{dP_r}{dz} \tag{5.10}$$

with K_z fiberbed permeability in the z-direction, $\hat{v}_{r,z}$ is resin velocity, μ_r is resin viscosity, P_r is resin pressure, and V_f is fiber volume fraction. Fiberbed compaction, hence fiber volume fraction, is assumed constant. This simplifying assumption is discussed further at the end of this section.

The resin infiltration rate through the thickness corresponds to the porosity variation rate of the RVE. Moreover, the resin pressure gradient is the difference between the applied pressure, P_a, gas pressure, P_g, and the capillary pressure, P_c. Therefore, Equation 5.10 can be written as:

$$\begin{aligned} \hat{v}_{r,z} &= \frac{d\gamma}{dt} = -h\frac{d\varphi}{dt} \\ &= -\frac{-K_z}{\mu_r(1-V_f)}\frac{(P_g+P_c-P_a)}{h(1-\varphi)} \end{aligned} \tag{5.11}$$

where h is the fiberbed thickness as shown in Figure 5.3. Using the above equations, the coupled gas/resin transport model can be written as:

$$\begin{cases} \varphi\dfrac{\partial P_g}{\partial t} = \dfrac{K_{x,0}}{\mu_g}\dfrac{\partial}{\partial x}\left(\left(1+\dfrac{b}{P_g}\right)P_g\dfrac{\partial P_g}{\partial x}\right) \\ \qquad\qquad +\dfrac{K_z}{h^2\mu_r(1-V_f)}\dfrac{P_g(P_g+P_c-P_a)}{(1-\varphi)} \\ \dfrac{d\varphi}{dt} = -\dfrac{K_z}{h^2\mu_r(1-V_f)}\dfrac{P_g+P_c-P_a}{(1-\varphi)} \end{cases} \tag{5.12}$$

The non-dimensional form of Equation 5.12 is used for numerical implementation of the coupled resin/gas transport model:

$$\begin{cases} \varphi\dfrac{\partial P_g^*}{\partial \tau} = \dfrac{\partial}{\partial \xi}\left(\left(1+\dfrac{b^*}{P_g^*}\right)P_g^*\dfrac{\partial P_g^*}{\partial \xi}\right) \\ \qquad\qquad +\dfrac{\beta}{1-\varphi}P_g^*(P_g^*+P_c^*-P_a^*) \\ \dfrac{d\varphi}{d\tau} = -\dfrac{\beta}{1-\varphi}(P_g^*+P_c^*-P_a^*) \\ \xi = \dfrac{x}{L},\ P_{g,a,c}^* = \dfrac{P_{g,a,c}}{P_{g,0}},\ b^* = \dfrac{b}{P_{g,0}} \\ \tau = \dfrac{K_{x,0}P_{g,0}}{\mu_g L^2}t,\ \beta = \dfrac{K_z\mu_g L^2}{(1-V_f)K_{x,0}\mu_r h^2} \end{cases} \tag{5.13}$$

In this equation, L and $P_{g,0}$ are characteristic length and reference gas pressure, set to 1 m and 101.35 KPa, respectively. These parameters are solely added to remove physical length and pressure dimensions.

In previous studies, resin infiltration predictions are possible only while the edge close to the vacuum port is not fully infiltrated by resin and the gas paths to the vacuum system are open [87]. However, resin infiltration will continue until either the entrapped gas pressure is equal to the applied pressure, or the resin gels. To address this issue, a conditional boundary-condition assignment scheme is used in the developed model that enables resin infiltration into the regions disconnected from the vacuum source, but with reduced gas pressure.

The boundary conditions for in-plane gas flow are set to $P_g^* = P_b$ at the breathing edge of the laminate and $\frac{dP_g^*}{d\xi} = 0$ at the far, closed edge. When porosity at any location, including the breathing edge, reaches to zero, that location becomes impervious to gas flow. Therefore, a fully-developed boundary condition, i.e. $\frac{dP_g^*}{d\xi} = 0$, must be applied around the fully-impregnated location. Physically, this allows the model to predict resin infiltration into the locations disconnected from the vacuum source, i.e. regions of reduced-pressure entrapped gas. The conditional boundary condition assignment scheme for the i^{th} cell in the domain is:

$$\text{if } \ \varphi_i = 0, \ \ \frac{dP_{g,i}^*}{d\xi} = 0 \ \ at \ \ \Omega, \sigma \tag{5.14}$$

where φ_i and $P_{g,i}^*$ denote porosity and gas pressure of the i^{th} cell, respectively. Ω and σ stand for the domain field and the domain boundary, respectively.

The permeability terms, K_{x0} and K_z, are assumed constant in the present analysis, which is consistent with constant fiber volume fraction and fiberbed compaction during processing [17]. It has been shown by Farhang [14] that the fiberbed becomes compressed when vacuum is applied under the bag at room temperature, but that a steady state is reached after a few minutes with a constant fiberbed compaction and permeability. For applied pressures higher than one atmosphere,

empirical models that relate fiberbed compaction, fiber volume fraction, and permeability are well-established in the literature [55, 56] as well as the corresponding implementation methods [18]. These models can be incorporated in the present model to provide pressure-dependent permeability values.

5.3.2 Model implementation

The implementation of the coupled gas/resin transport model is based on gas transport in the transverse direction of the resin infiltration. Therefore, a 1D finite volume method is employed to simulate the gas flow.

The form of Equation 5.13 to be implemented is:

$$\begin{aligned} \varphi \frac{\partial P}{\partial \tau} &= \frac{\partial}{\partial \xi}\left(\left(1+\frac{b^*}{P}\right) P \frac{\partial P}{\partial \xi}\right) + f(p) \\ f(P) &= \frac{\beta}{1-\varphi} P_g^* (P + P_c^* - P_a^*) \end{aligned} \tag{5.15}$$

In this equation, P_g^* notation is replaced with P for the sake of clarity in the rest of the section. By integrating above equation over the ith control volume, and using Gauss theorem:

$$\varphi_i \frac{\partial P_i}{\partial \tau} = \frac{1}{\Delta \xi}\left(P_i \left(1+\frac{b^*}{P_i}\right) \frac{\partial P_i}{\partial \xi}\right)_{i-\frac{1}{2}}^{i+\frac{1}{2}} + f(P_i) \tag{5.16}$$

Then, a second-order centered scheme for space discretization, and Implicit Euler time advance scheme give:

$$\varphi_i \frac{P_i^{n+1} - P_i^n}{\Delta \tau} = P_i^{n+1}\left(1+\frac{b^*}{P_i^{n+1}}\right) \frac{P_{i+1}^{n+1} - 2P_i^{n+1} + P_{i-1}^{n+1}}{\Delta \xi^2} + f(P_i^{n+1}) \tag{5.17}$$

Moreover, the non-linear term ($f(P)$) can be linearized using Newton's method as:

$$\delta\varphi_i \frac{\delta P}{\Delta\tau} = P_i^n \left(1 + \frac{b^*}{P_i^n}\right) \frac{P_{i+1}^{n+1} - 2P_i^{n+1} + P_{i-1}^{n+1}}{\Delta\xi^2} + [f(P_i^n) + f'(P_i^n)\delta P]$$
$$\delta P = P_i^{n+1} - P_i^n \tag{5.18}$$

In this equation, the $P_i^n \left(1 + \frac{b^*}{P_i^n}\right)$ is also estimated based on the current time step, i.e. step n instead of $n+1$, to further linearize Equation 5.17.

A solver based on tri-diagonal matrix algorithm, the Thomas solver, is used to update gas pressure at each cell using Equation 5.18. Further, porosity is updated at each time step as:

$$\varphi_i^{n+1} = \varphi_i^n + \Delta\tau\beta_i(P_i^n + P_c^* - P_a^*) \tag{5.19}$$

The discretized model was then implemented using the open-source DevC++ 5.11 compiler, Appendix A. In the implemented model, the length of the domain, i.e. length of the transport channel is variable, L. Using an element size of 0.01, the number of elements varies with length as $L/0.01$. The time scale of resin infiltration is significantly slower than the timescale for gas transport. Therefore, a large time-step would lead to unstable results. It was found that a time-step of 0.0001s results in stable results. The criteria for stability was found as the largest time-step below which results, gas pressure and resin impregnation, remain time-step independent.

5.3.3 Numerical simulation

The material properties used in the numerical simulation are shown in Table 5.2. The cure kinetics and viscosity models developed by Shahkarami and Van Ee [21] and implemented in the commercial software RAVEN [22] were used in this study. The calculated resin viscosity profiles during the current cure cycle in Figures 5.7 and 5.8 show a drop in viscosity from 4.2×10^4 Pas at room temperature to about 11 Pas at minimum viscosity where the 120°C temperature-hold starts. The

Table 5.2: Material properties and parameters used in numerical test cases for the coupled gas/resin transport model.

Parameter	**Nomenclature**	**Value**	**Reference**
Uncured prepreg thickness	h	0.1 mm	Measured
Initial prepreg porosity	φ_0	19.7%	Measured
Initial gas pressure	$P_{g,0}$	101.3 kPa	–
Characteristic length	L	1 m	–
Through-thickness permeability	K_z	3.5×10^{-16} m^2	[17, 126, 127]
Initial in-plane permeability	$K_{x,0}$	5.0×10^{-15} m^2	[14, 25, 57]
Fiber volume fraction	V_f	54%	[32]
Klinkenberg parameter	b	13 kPa	[25]
Gas (air) viscosity	μ_g	1.8E-05 Pas	[128]
Resin viscosity	μ_r	Viscosity model	[22]

in-plane permeability for gas and through-thickness permeability for resin are found in the literature for similar prepregs [14, 17, 25, 57, 126, 127].

The capillary pressure in Equation 5.13 (P_c^*) is set to zero. The maximum capillary pressure for uniaxial infiltration of low viscosity (0.01 Pas) epoxy resin into a fiber tow has been reported to reach about 14 kPa [72]. This is about 14% of the expected pressure difference in out-of-autoclave processing, i.e. 101.3 kPa. In the present study, resin infiltration occurs through-thickness of a woven fiberbed that includes inter-tow regions with large spacing, in comparison to the small fiber spacing in unidirectional fiber tows. The minimum viscosity of the resin system used is 10 Pas. Therefore, the capillary pressure contribution is not significant for the resin system and fiberbed architecture in the present study.

Figure 5.7 shows the porosity evolution as a function of time during debulk and cure, as predicted numerically for an IAP test case. The bag and applied pressures were set to $P_b = P_a = 1$ atm during debulk, and the applied pressure was increased to $P_a = 2$ atm during cure. The coupled

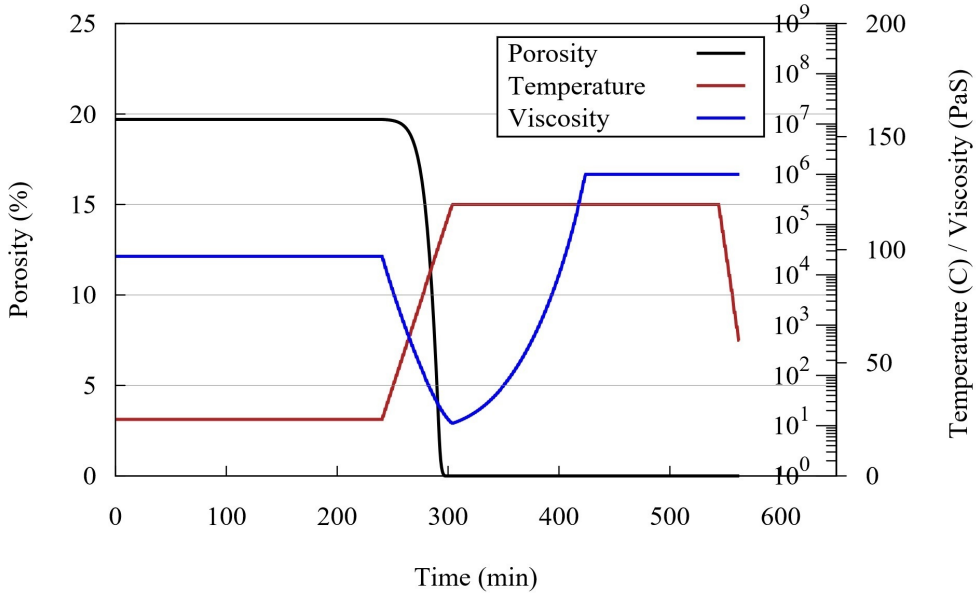

Figure 5.7: Predicted porosity evolution for an IAP test case with $P_b = P_a = 1$ atm during debulk, and $P_b = 1$ and $P_a = 2$ atm during cure. IAP: increased applied pressure; P_a: applied pressure; P_b: bag pressure.

gas/resin transport model prediction suggests that even with no debulk, final porosity reaches zero, given an increase in applied pressure. This observation is consistent with the experimental results for the IAP setup where regardless of the debulk condition the final porosity was found to be close to zero.

Figure 5.8 shows the porosity evolution as a function of time during debulk and cure, as predicted numerically for an RBP test case with $P_b = 0.43$ and $P_a = 1.0$ atm, during debulk and cure. A slight porosity reduction of about 0.35% during debulk is predicted. In this case, the difference between applied pressure and bag pressure during the room temperature debulk causes a minor infiltration of the high viscosity resin into the un-infiltrated fiberbed. However, the main porosity reduction occurs in the heat-up region where the resin viscosity drops. At around the minimum

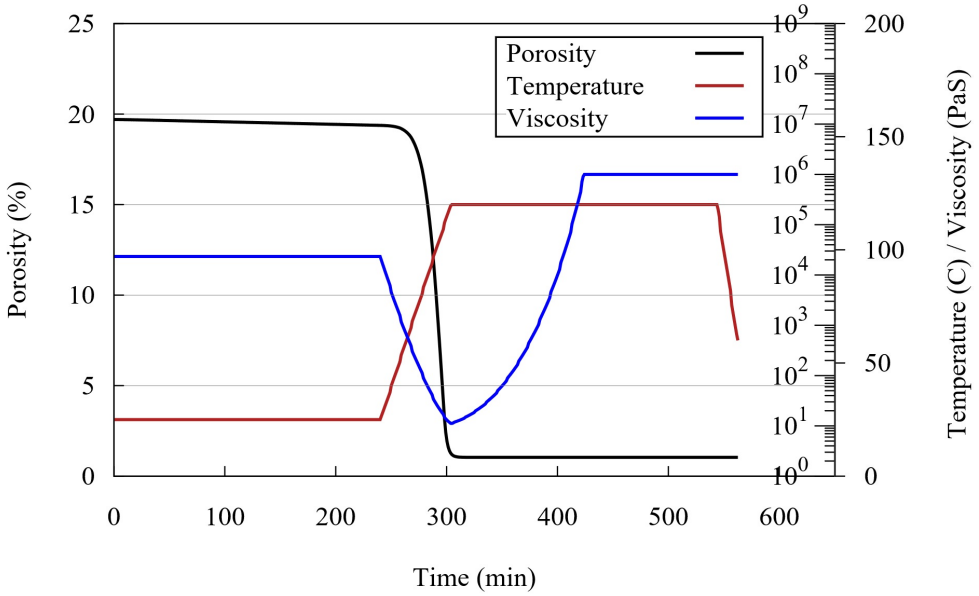

Figure 5.8: Predicted porosity evolution for a RBP test case with $P_b = 0.43$ and $P_a = 1$ atm during debulk and cure. RBP: reduced bag pressure; P_a: applied pressure; P_b: bag pressure.

resin viscosity, resin infiltration closes the breathing edge of the laminate and stops further gas evacuation. Moreover, the viscosity increase followed by gelation inhibits further resin infiltration.

5.3.4 Numerical results and discussion

The predicted porosity using the developed model are shown in Figure 5.9 for RBP experiments. Similar to average porosity calculations in the experimental part, the predicted porosity reported in this figure is the average of porosity throughout the length of the laminate. The comparison between measured and predicted porosity in this figure shows that the developed explicitly-coupled model explains the experimental data well, based on the model input parameters from the literature. It also shows that a simple estimation based solely on gas transport during debulk significantly over-estimates the porosity. In Figure 5.9, the porosity at $P_b = 1.0$ atm is the initial porosity of the fiberbed, 19.7%.

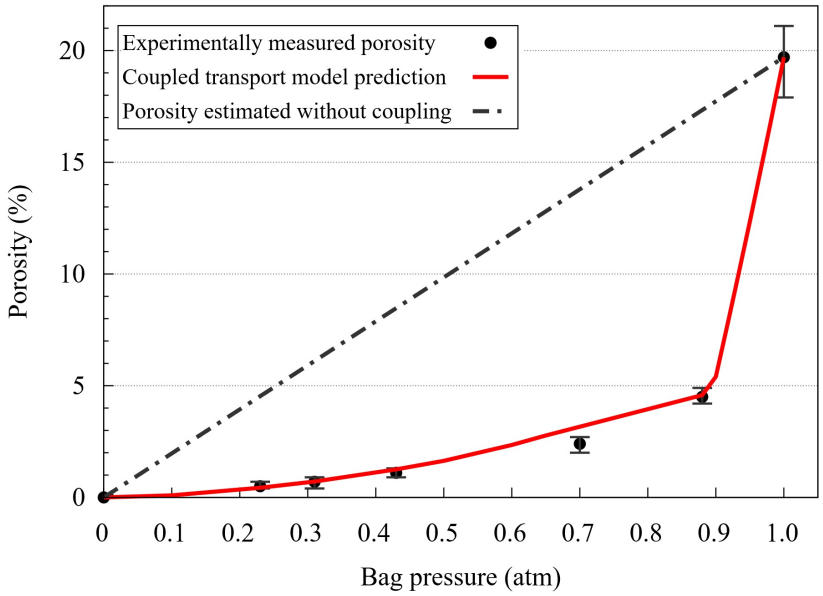

Figure 5.9: Comparison of experimental results, porosity estimated using Equation 5.1, and porosity predicted using the explicitly coupled transport model.

The material properties used in the coupled transport model, Table 5.2, are based on extensive material characterizations and robust modelling [21]. However, the reported fiberbed permeability for the same material system varies slightly in different studies [25]. Model predictions with a $\pm 20\%$ variation in permeability values were studied to evaluate the robustness of the coupled transport model against uncertainties in permeability characterizations. Figure 5.10 and Figure 5.11 present the results with through-thickness and in-plane permeability variation, respectively. According to the results, the model predictions do not change significantly by varying the permeability within the range explored. Furthermore, the model tends to be more sensitive to in-plane permeability for gas transport than through-thickness permeability for resin infiltration. Specifically, the maximum variation in predicted porosity is 15% with $\pm 20\%$ variation of the in-plane permeability. For the same range of variation in through-thickness permeability, the maximum porosity variation is 8%.

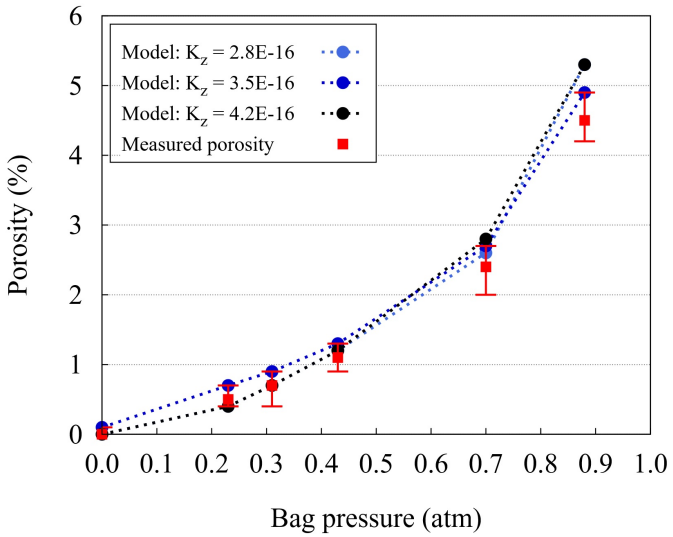

Figure 5.10: Variation of the porosity predicted using the coupled transport model with through-thickness permeability (K_z). The in-plane permeability is fixed at $K_{x,0} = 5.0 \times 10^{-15}$.

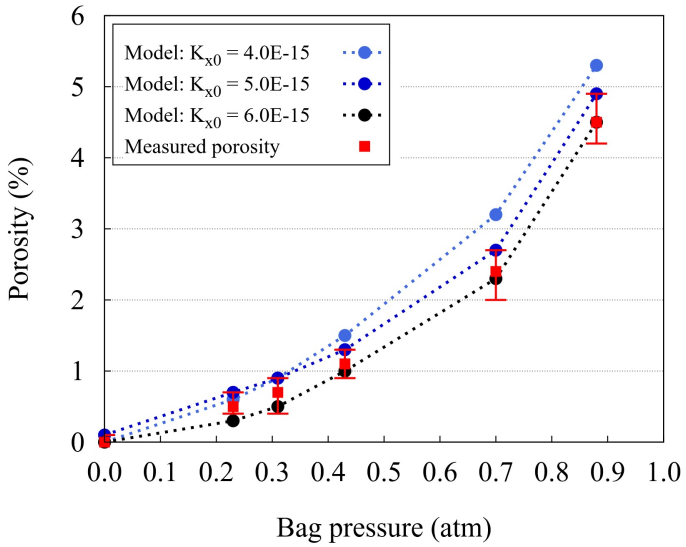

Figure 5.11: Variation of the porosity predicted using the coupled transport model with in-plane permeability ($K_{x,0}$). The through-thickness permeability is fixed at $K_z = 3.5 \times 10^{-16}$.

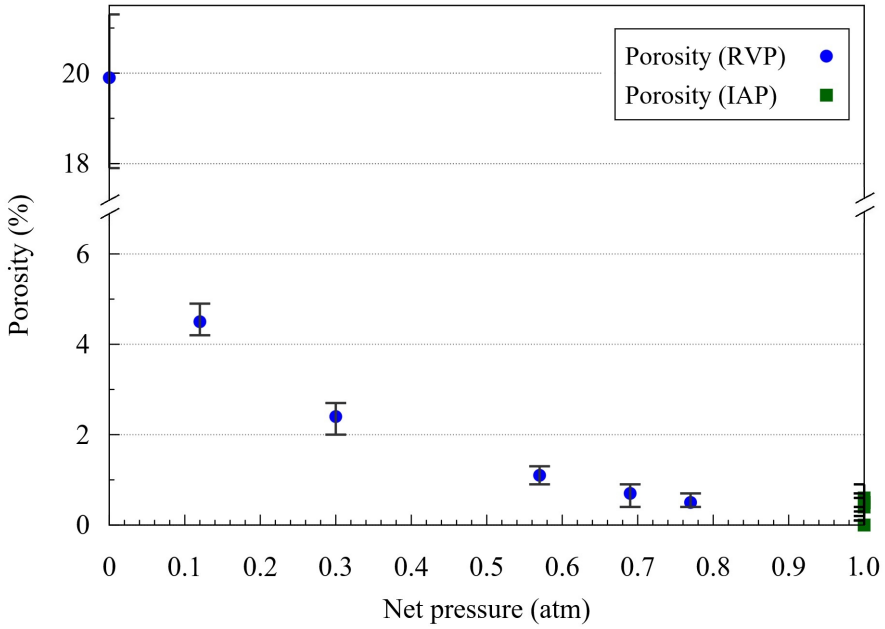

Figure 5.12: Measured porosity for all experiments (RBP and IAP) as a function of the net pressure, $P_n = P_a - P_b$.
IAP: increased applied pressure; RBP: reduced bag pressure; P_a: applied pressure; P_b: bag pressure.

The experimental and analytical work in this section further highlighted the importance of the net pressure on the laminate during cure. This can be understood by accumulating the results of both IAP and RBP tests in Figure 5.12. This figure shows that the measured porosity correlates well with the net pressure on the laminate for both RBP and IAP tests. It also shows that by maintaining a net pressure higher than 0.5 atm, the final porosity reduces below the 2%, for both RBP and IAP tests. This suggests that a room-temperature debulk is less important than what is typically believed. Nonetheless, the laminates used in the present study are comparatively small [61] which increases the ability for gas to escape the laminate during cure.

The effect of bag and applied pressures in the case of longer laminates were evaluated via a parametric study using the explicitly-coupled model. For this purpose, a cure cycle, like that in

Figure 5.7, was used, but with variable debulk time. The same model parameters as in the previous case, Table 5.2, were used.

Figure 5.13 shows the minimum debulk time required to achieve a part with average porosity below 1.0% as a function of bag pressure. In these parametric tests $P_a = 1$ atm and $P_b =$ varying, during debulk and cure. The figure shows that the required debulk time increases with the size of the laminate or the length of the gas transport channels. With the application of full-vacuum ($P_b = 0$ atm) during cure, no debulk is required for laminates with a length below 50 cm; however, a 98-hour debulk is needed to manufacture a 5-meter long laminate with an average porosity below 1.0%. Furthermore, reducing the bag pressure increases the required debulk time. A debulk time of 20 h is required to reduce the average porosity of a 2-meter laminate to below 1.0% with full vacuum. This increases to about 68 h with a 10% bag pressure reduction during debulk and cure.

Note that the current model simulates gas transport in one dimension, with a symmetric boundary at one end, $\frac{dP^*_{g,i}}{d\xi} = 0$. Therefore, the solution for an L-meter laminate corresponds to a 2L-meter long part that is connected to the vacuum at both ends.

The current implementation of the model is 1D. A 1D model gives a conservative estimate of porosity, since adding gas flow in a second perpendicular direction (i.e. a 2D solution) will increase the rate with which gas is removed and gives a porosity that is lower than predicted with a 1D solution. The 1D solution should be applied to the smallest in-plane dimension in a case where there is 2D flow.

The observed debulk time variation can be explained by considering the change in time scales for resin and gas transport with part size. Laminate thickness remains constant giving a constant time scale for resin transport through-thickness for a given cure cycle, whereas the time scale for gas evacuation varies with the length squared; see the equation for the dimensionless time in Equation 5.13.

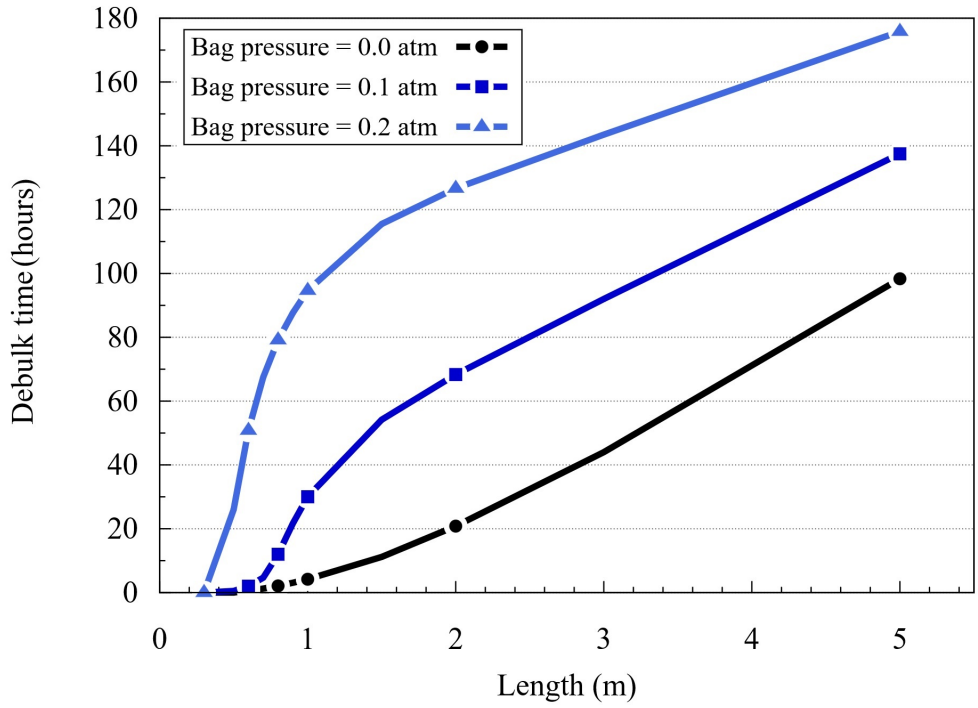

Figure 5.13: Minimum debulk time required to obtain an average porosity below 1.0% as a function of part length and bag pressure. $P_a = 1$ atm and P_b varying, during debulk and cure, i.e. RBP setup.
RBP: reduced bag pressure; P_a: applied pressure; P_b: bag pressure.

The discussion above was focused on out-of-autoclave process conditions, i.e. $P_a = 1.0$ atm. However, shorter required debulk times are expected if the applied pressure during cure is increased using an autoclave. Figure 5.14 shows the minimum debulk time required to achieve porosity below 1.0% for a 5-meter and a 2-meter laminate as a function of the applied pressure during cure. Debulk is conducted under regular conditions: $P_a = 1.0$ and $P_b = 0.0$ atm, and cure with $P_a =$ varying and $P_b = 0.0$. As expected, the required debulk time decreases significantly with an IAP setting during cure.

In the present parametric study, the applied pressure effect on porosity is due to the extent the entrapped gas can be compressed after the breathing edge of the laminate closes due to resin

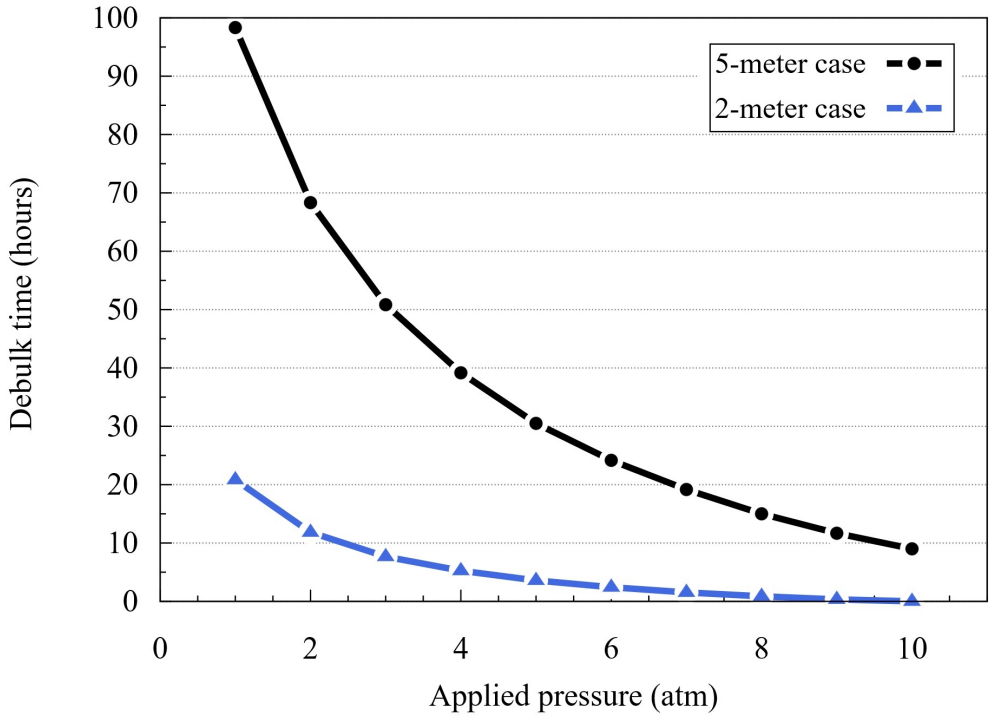

Figure 5.14: Minimum debulk time required to obtain average porosity below 1.0% as a function of applied pressure during cure. $P_a = 1$ atm and $P_b = 0$ atm during debulk, $P_a =$ varying, and $P_b = 0$ atm during cure.
P_a: applied pressure; P_b: bag pressure.

infiltration. Figure 5.15 shows an example of a 2-meter long laminate debulked for 52 min at $P_a = 1.0$ and $P_b = 0.0$ atm, and cured under $P_a = 8.0$ and $P_b = 0.0$ atm. The first line shows the porosity contour after 30 min into the cure when the average gas pressure inside the laminate is 1.1 atm. This increased gas pressure is due to resin infiltration and compression of the gas. After about 35 min into the cure, the edge connected to the vacuum source closes due to resin infiltration. The average gas pressure at this time has also increased further. After this point in time, the internal gas pressure increases until it reaches the applied pressure of 8 atm, which occurs 42 min after cure starts.

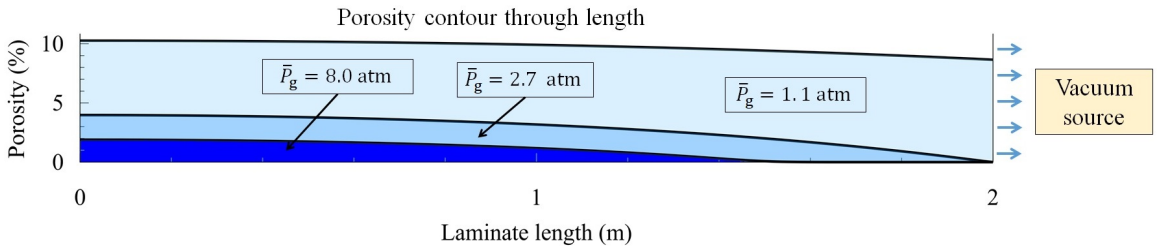

Figure 5.15: Predicted porosity evolution for a 2-meter long laminate, debulked for 52 min at $P_a = 1.0$, $P_b = 0.0$ atm and cured under $P_a = 8.0$, $P_b = 0.0$ atm. Top line: 30 min after beginning of heat-up; middle line: when the edge close to the vacuum source closes; bottom line: when the gas pressure inside the laminate reaches the applied pressure.

In the experimental and analytical parts of the present study, a single cure cycle was used for the sake of consistency. The resin infiltration rate can also be controlled via cure cycle manipulation, e.g. by manipulating heating rates and/or hold temperatures. Altering the cure cycle changes the timing for resin gelation or vacuum channel closure that can both lead to incomplete resin infiltration, thus porosity formation. The developed gas/resin transport model is a simple tool for optimizing processing parameters such as cure cycle, bag, and applied pressures, to minimize porosity formation due to entrapped gas or incomplete resin infiltration.

5.4 Summary

In this study, the effect of resin and gas transport on porosity during the processing of partially-impregnated prepreg was investigated. An experimental setup was developed to isolate the effect of the bag and applied pressure on final porosity. Porosity measurements suggest that resin infiltration causes a pressure increase in the remaining gas within the prepreg that is in direct contact with the resin flow-front. This is a driving factor for further gas transport out of the laminate and porosity reduction during heat-up and cure.

Informed by the experimental observations, an explicitly-coupled transport model was developed that includes the resin and gas interaction during the processing of partially-impregnated

prepregs. The model predicted the experimental data well based on material parameters from the literature.

It was shown that an increase of the applied pressure on the laminate could compensate for the effect of an RBP during debulk and cure. However, the effectiveness of gas transport and the resulting porosity reduction, due to both applied pressure on the laminate or imposed bag pressure, is highly size-dependent. Numerical case studies highlighted this dependency and showed that the developed model serves as a good tool to explore and better understand the coupled nature of resin and gas transport and their effect on porosity.

Chapter 6

Post-gelation internal stress defects

6.1 Introduction

Internal stress development due to constrained free strains is a poorly-understood source of defect formation during composites manufacturing. The present work investigates internal stress-induced defects within the processing window from gelation to glass transition. After gelation, the rubbery resin has formed a 3-dimensional structure that suppresses mechanisms such as bubble growth or infiltration. However, the resin's ability to withstand stress accompanied by free strain development cause internal stresses in the resin matrix. These stresses can lead to matrix defects upon reaching critical values.

The goal of this chapter is to investigate the mechanisms of defect formation after gelation, and use the developed knowledge for process design and optimization. This requires an experimental setup that allows observing the resin behavior during cure at the critical stage, post-gelation and before glass transition.

In the first part of this chapter, the experimental setup used is described along with the material characterization conducted. This is followed by an experimental study of the post-gelation defect

formation. Finally, an analytical approach for processing to avoid such defects is presented and experimentally validated.

Two main sources of free strain in the thermosetting resins are thermal strain and cure-induced volumetric shrinkage. Free strains lead to internal stress development only in the presence of the geometrical constraints. Therefore, the basic assumption in discussions about internal stress-induced defects is that free strains develop in a fully-constrained unit of volume. Free strains may be additive or subtractive depending on the temperature variation. Therefore, while examining the fundamentals of the defect formation, the thermal strain effect was isolated by conducting the experiments isothermally. Nonetheless, the analytical approach to suppress post-gelation defects captures both thermal strain and cure shrinkage effects.

6.2 Materials characterization

A resin-infusion-grade epoxy system is used in the present study, Rhino 1411 resin and Rhino 4111 hardener mixed with a 100:30 ratio by weight [129]. Low room-temperature viscosity, fast cure, and adhesion to glass surface are the main characteristics of this resin system that facilitate the shrinkage-defect experiments. Different material properties were characterized in order to develop a comprehensive material model.

In the case of properties such as coefficient of thermal expansion (CTE), the data from characterization was directly employed to find the desired properties. In other cases such as cure kinetics characterization that required extensive data preparation and model fitting, the commercial KERMODE software [130] was used. All material properties and developed models were then implemented in the commercial RAVEN software [22]. The material properties characterized and the related methodologies are described below in detail.

6.2.1 Cure kinetics and glass transition temperature

Material property evolution in the case of a thermosetting resin depend on its cure kinetics. Therefore, an extensive set of Dynamic Scanning Calorimetry (DSC) tests were conducted using TA 2500 equipment for detailed cure kinetics characterization.

Three types of DSC tests were conducted: isothermal, dynamic, and interrupted tests. Isothermal tests targeted complete cure by holding a sample at a set temperature for an extended time. Isothermal test temperatures were 25, 40, 60, and 80°C with hold-times of 900, 360, 240, and 120 min, respectively. During dynamic DSC tests, samples were heated from -80 to 200°C at 2, 3, 4, and 5°C/min. The goal of the dynamic tests is to measure the total heat generated due to the complete cure of the resin. The interrupted DSC tests helped with data augmentation to enhance the accuracy of the cure kinetics models. These tests consist of a hold at a set temperature for a certain

Table 6.1: Temperatures and hold times used for the interrupted DSC tests.

Temperature (°C)	Hold (min)	Temperature (°C)	Hold (min)
25	30	40	180
25	240	40	300
25	720	60	5
40	10	60	10
40	30	60	30
40	60	60	60
40	120	60	120

time, cooling the sample to -80°C, and measuring the residual heat using a temperature ramp to 200°C at 2°C/min. In total, 14 interrupted tests were conducted; details shown in Table 6.1.

Each DSC experiment used a small amount of neat resin, 8±2 mg, with mix-to-test time of 7±2 min, at room temperature. Experiments were conducted in a modulated temperature ramp mode which enabled the calculation of the reversible heat capacity. The glass transition temperature (T_g) was then determined graphically by a deflection that happens at this temperature in a plot of heat capacity versus temperature [94]. The Trios software built into the DSC system was used for analyzing the heat flow baseline and the deflection point of the heat capacity diagram. Figure 6.1 shows the residual heat flow and heat capacity measurements for an interrupted test with a sample pre-cured at 60°C for 60 min.

The data from DSC tests was fitted against a cure kinetics model with cure rate, $\dot{x}$, defined as [22]:

$$\begin{aligned} \dot{x} &= \left(\textstyle\sum_{i=1}^{n} 1/\dot{x}_i\right)^{-1} \\ \dot{x}_i &= A_i \exp\left(\frac{-B_i}{C_i T - D_i T_g + E_i}\right) \end{aligned} \tag{6.1}$$

Here, A_i, B_i, C_i, D_i, and E_i are fitting parameters defined as functions of degree of cure, n is the number of reactions, T is temperature, and T_g is glass transition temperature. Figure 6.2 shows

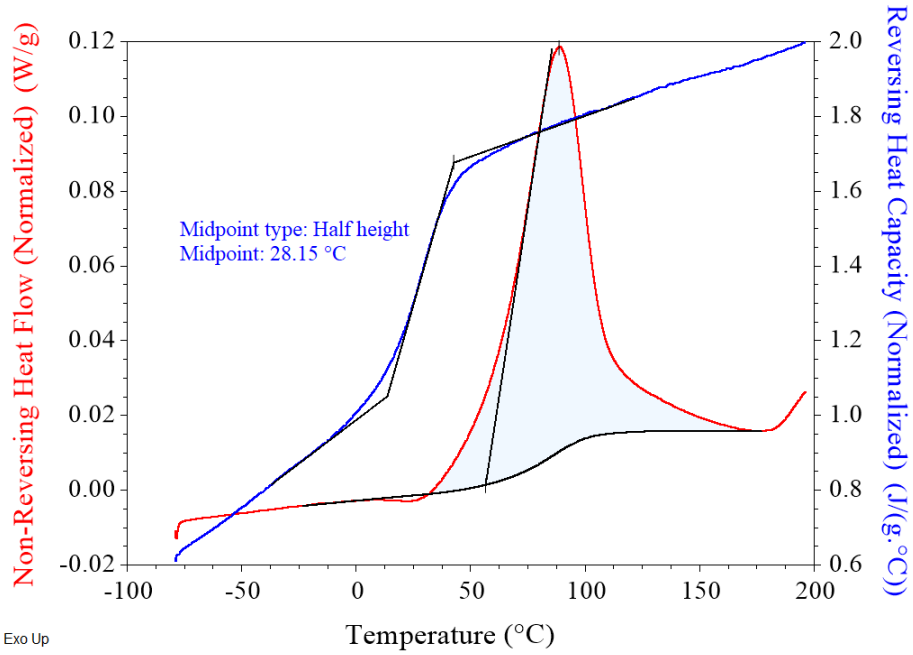

Figure 6.1: A sample analysis to find the baseline for heat-flow and the deflection point for the heat capacity diagram, using the Trios software. In this example, the sample was pre-cured at 60°C for 60 min.

the model prediction versus experimental data from interrupted DSC tests. Due to the resin's fast cure at 80°C, no interrupted test was conducted at this temperature, i.e. only isothermal test at this temperature was used for model fitting. Isothermal tests consisted of holding the uncured sample at a constant temperature until cure completion, in contrast with the interrupted tests where the cure cycle was cut before completion. The goodness of fit, R-square of measured and predicted degree of cure, for the isothermal tests was 72.2%, according to the KERMODE software.

The measured glass transition temperatures were fitted against the DeBenedetto equation:

$$T_g = T_{g0} + \frac{\lambda x (T_{g\infty} - T_{g0})}{1 - (1 - \lambda)x} \tag{6.2}$$

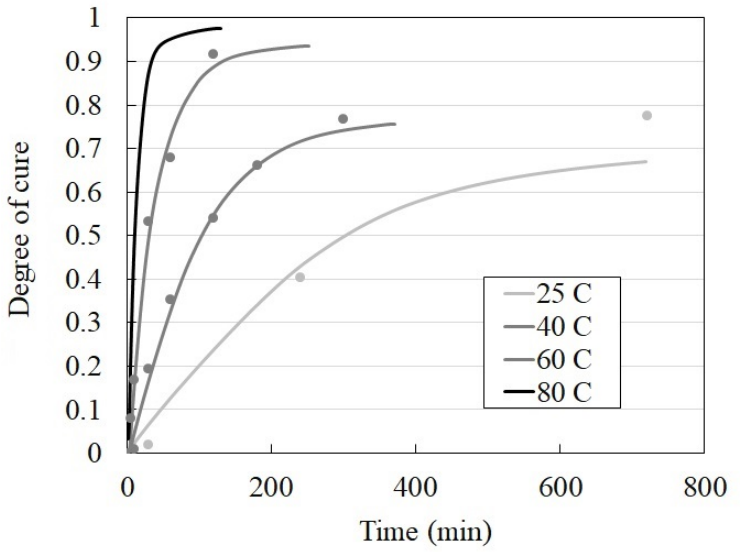

Figure 6.2: Cure kinetics modeling results. The solid lines show model predictions and dots show the experimental results of the interrupted DSC tests.

Table 6.2: DeBenedetto model parameters determined for Rhino 1411 fast cure.

Parameter	Value	Unit
T_{g0}	-49.5	°C
$T_{g\infty}$	90	°C
λ	0.5	–

where, x is the degree of cure, T_{g0} is the glass transition temperature of the uncured resin, $T_{g\infty}$ is the glass transition temperature of the fully-cured resin, and λ is the DeBenedetto parameter, a material constant. The parameters determined for Rhino 1411 fast cure are shown in Table 6.2. Figure 6.3 shows a comparison between the model predictions and the measured T_g. The goodness of fit, R-squared, between measured and predicted T_g is 98.3%.

6.2.2 Cure shrinkage

Volumetric cure shrinkage is one of the main sources of free strain development in the constrained curing resin. Therefore, an understanding of the cure shrinkage evolution during cure is critical.

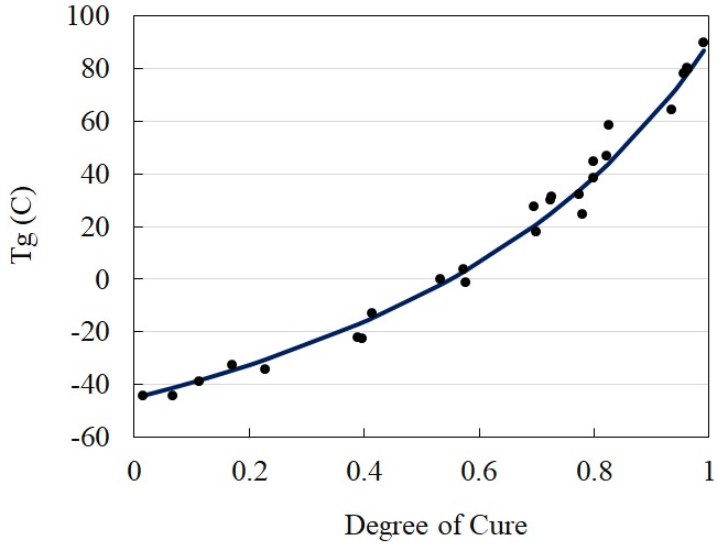

Figure 6.3: Glass transition temperature (T_g) model results. The solid line shows the DeBenedetto equation predictions and dots show experimental measurements using interrupted and isothermal DSC tests.

Cure shrinkage characterization for Rhino 1411 fast-cure was performed using the Drop Shape Analysis (DSA) method [103]. In this method, shape variation of a droplet of resin with cure is tracked by time-lapse imaging. Volumetric shrinkage as a function of cure time is then calculated using advanced image processing based on the recorded images.

For the resin system in the present study, cure shrinkage was characterized during isothermal cure at 25, 40, and 60°C. Given the developed cure kinetics model, the data was transformed to volumetric shrinkage versus degree of cure. As expected from the discussion in Section 2.4.2, the cure shrinkage was found to vary linearly with the degree of cure with a relatively constant slope, at all temperatures, Figure 6.4. In this figure, the average slope of the shrinkage diagrams is 0.1 ± 0.01. The shrinkage increase at high DOC in the 40 and 60°C tests is related to cool-down from testing temperature to the room-temperature, 25°C.

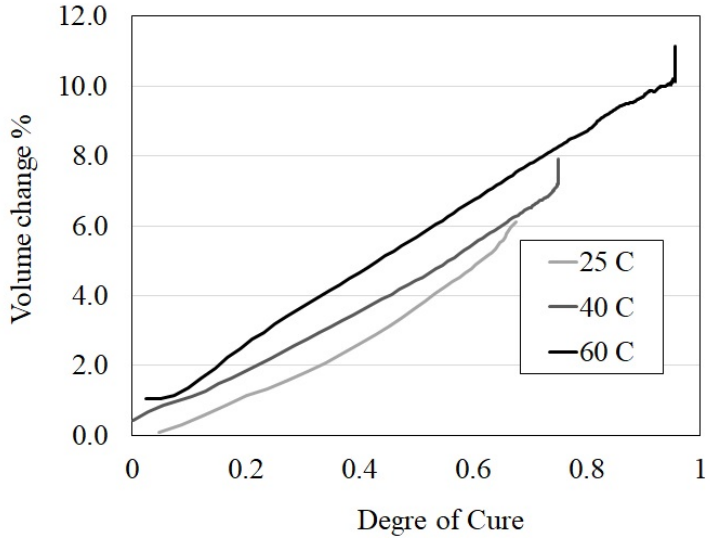

Figure 6.4: Experimental results of the DSA (Drop Shape Analysis) tests for cure shrinkage characterization. Shrinkage variation demonstrates linear variation relative to degree of cure with a relatively constant slope.

Considering the shrinkage characterization data, a linear model was implemented to explain the volumetric cure shrinkage, Δv_{cure}:

$$\Delta v_{cure} = kx \tag{6.3}$$

In this equation, x is degree of cure, and k is a constant calculated based on the maximum cure shrinkage, at DOC $= 1.0$. This constant was estimated to equal 0.1 for the resin system used. The cure shrinkage model prediction results are shown in Figure 6.5.

6.2.3 Coefficient of thermal expansion (CTE)

Thermal expansion is another source of free strain during cure. To account for this effect, the Coefficient of Thermal Expansion (CTE) was measured using Thermomechanical Analysis (TMA) with a TA Q400 instrument. Sample preparation and CTE calculation from the displacement versus temperature data followed the E831-14 ASTM standard [131].

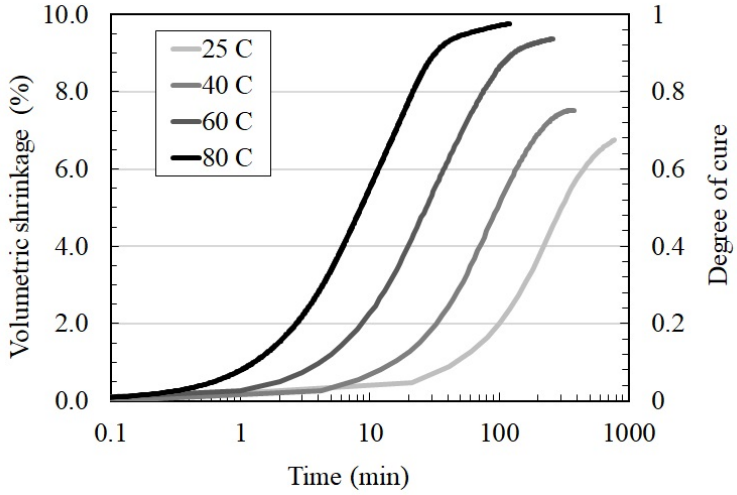

Figure 6.5: Model predictions of volumetric cure shrinkage and cure kinetics evolution at different isothermal cure temperatures.

Cubic samples with a volume of about 25 mm^3 were extracted from a block of fully-cured resin. The manufacturer-recommended cure cycle used for full-cure consisted of 4 h hold at 65°C followed by 2 h hold at 85°C [129].

The CTE measurement samples were heated from 0 to 110°C at 5°C/min and cooled back to 0°C at 5°C/min. This cycle was then repeated two more times. The results in Figure 6.6 show that except the inflection around the glass transition temperature the slope of the displacement versus temperature remains almost constant, hence constant coefficient of thermal expansion.

The first temperature cycle during each measurement was ignored due to the unwanted sample movement at the beginning of the test. The CTE was measured based on the second and third cycles, consistently giving a CTE of 208×10^{-6} and 58×10^{-6} C^{-1} for the rubbery and glassy resin, respectively, with a standard deviation of 0.54×10^{-6}

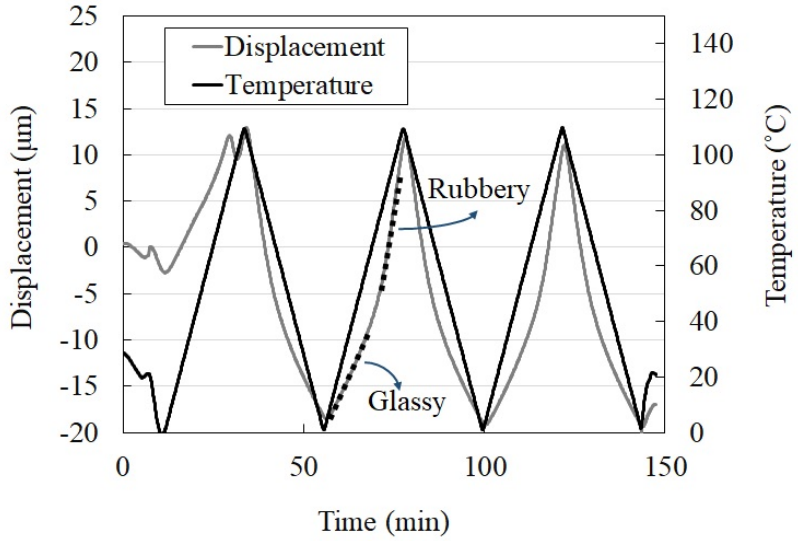

Figure 6.6: Results of CTE measurements using Thermomechanical Analysis (TMA).

6.2.4 Shear modulus and gelation point

Characterization of the shear modulus serves two main goals. A standard approach for gelation point measurement is based on examining the shear modulus evolution during cure using dynamic rheometry tests. The cross over between the storage shear modulus and the loss shear modulus is an indication of gelation. Since, the present study aims to study the post-gelation defects, a reliable estimation of the gelation point is necessary. Another application of the shear modulus characterization is to track stress development inside the resin during cure.

In the present study, the shear modulus was characterized using an Anton Paar MCR 502 rheometer. The uncured liquid resin was placed between parallel plates and an oscillatory torque was applied with a declining rotation amplitude of 7 to 0.3%, at a constant frequency of 1.0 or 0.1 Hz. Isothermal tests were conducted at 25, 40, 60, and 80°C with a repeat at each temperature while changing the oscillation frequency to ensure results are frequency independent.

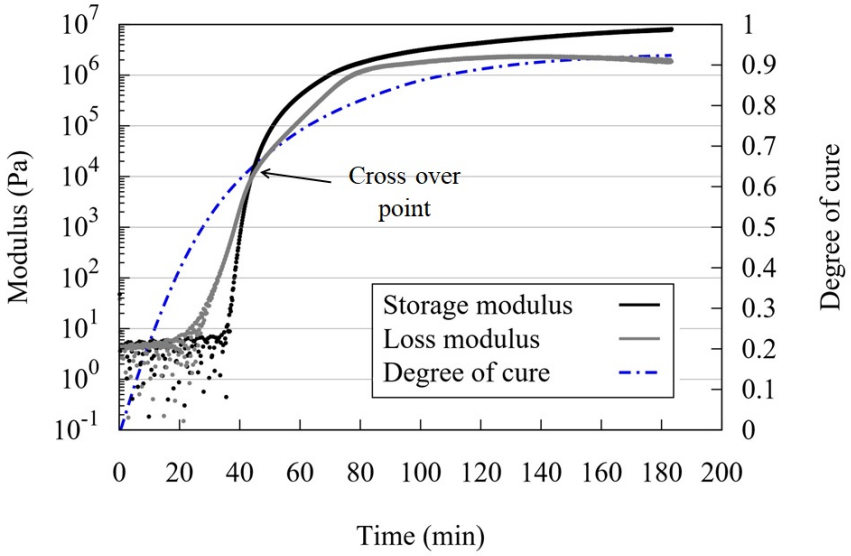

Figure 6.7: A sample rheometry test result for the isothermal cure at 60°C. The crossover between storage and loss shear modulus occurs at DOC $\approx$ 0.64. The cross over point is an indication of gelation. Degree of cure is calculated based on the cure kinetic model developed in Section 6.2.1.

An example of the rheometry result in the case of testing at 60°C is shown in Figure 6.7. Using the cure kinetics model, the degree of cure at each stage was calculated. It was found that the resin consistently reaches gelation at a 0.65$\pm$0.02 degree of cure at all temperatures.

Another observation is that in all tests, the shear modulus before gelation is below 1 MPa. This is expected given to the viscous liquid nature of the resin before gelation, Section 2.4.1.

6.2.5 Young's modulus

Due to the maximum force limitation of the rheometry equipment, shear modulus characterization was possible until slightly after gelation. Therefore, additional Dynamic Mechanical Analysis (DMA) tests were conducted to provide data for the mechanical properties of the resin after gelation. The measurements used the TA Q800 1616 equipment and fully-cured $50\times10\times3$ mm^3 samples. The cure cycle was similar to the one used to prepare CTE measurement samples, Section 6.2.3. Dy-

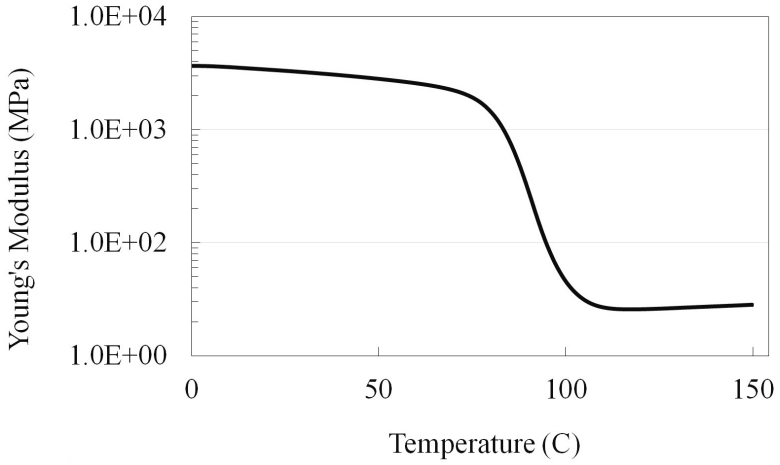

Figure 6.8: Result of a temperature-sweep Dynamic Mechanical Analysis (DMA) test. The glass transition temperature of the fully-cured sample used is ≈90°C.

namic tests were conducted in a three-point-bending configuration with amplitude and frequency equal to 100 μm and 1.0 Hz, respectively. The DMA test was repeated one more time, using a new sample, to ensure data accuracy. The root mean square deviation between two repeats was 69 MPa, with a maximum modulus of 3.6 GPa at 0°C.

The glass transition temperature of the fully-cured sample is 90°C. According to the DMA test results in Figure 6.8, above this temperature, the modulus drops significantly while the material transitions from a glassy state to a rubbery state.

Common material models describe modulus (shear, bulk, or Young's) as a function of $T - T_g$ to simultaneously account for temperature and cure dependencies. With the application of a fully-cured sample for DMA testing, T_g remains constant throughout the test. However, a temperature sweep provides modulus data in a range of $T - T_g$. Consequently, this data can be fitted against a modulus model to find the corresponding material constants. This approach, in addition to the data from rheometry and DMA test, was used to find material parameters for a calibrated CHILE (cure hardening instantaneously linear elastic) model [132] for both shear and bulk modulus. CHILE

models behave similar to pure elastic models with respect to time, i.e. modulus remains constant at each instant of time. However, the modulus in CHILE models is a function of temperature and degree of cure:

$$G' = \begin{cases} G_r + (G_g - G_r)\sigma_{fit} & x > X_{gel} \\ G_{min} & x \leq X_{gel} \end{cases}$$
$$K' = \begin{cases} K_r + (K_g - K_r)\sigma_{fit} & x > X_{gel} \\ K_{min} & x \leq X_{gel} \end{cases} \tag{6.4}$$
$$E = \frac{9K'G'}{3K' + G'}$$

E, K, and G are Young's modulus, bulk modulus, and shear modulus, respectively. The subscripts "r" and "g" refer to rubbery and glassy states, respectively. σ_{fit} is a fitting parameter and a function of degree of cure, x. x_{gel} refers to the degree of cure at gelation.

The bulk modulus was not independently characterized in the present thesis. K_r and K_g were found to be 1.67 and 4.74 GPa, respectively, by manually fitting the Young's modulus and shear modulus data against the material model.

6.2.6 Summary of materials characterization

In the present study, internal stress-induced defects are investigated through characterization and calculation of the free strains during cure. Therefore, the development of the high fidelity material models for cure kinetics, T_g, CTE, gelation point, and cure shrinkage was an important part of the study. The mechanical property characterization also provided fairly accurate models for a qualitative study of the stress state at the time of defect formation.

Figure 6.9 summarizes the resin property evolution during isothermal cure at 60°C. The implemented bulk modulus model assumes a zero value before gelation. This is not physically correct since the viscous liquid has a bulk modulus comparable with the rubbery resin. However, the present

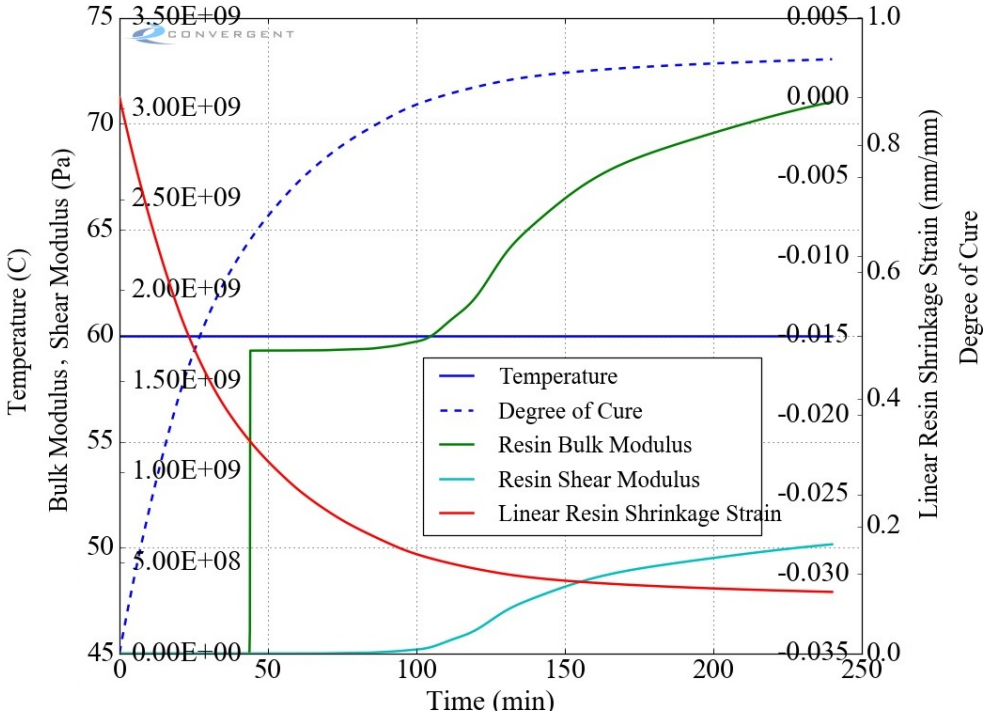

Figure 6.9: An example showing resin property evolution during isothermal cure at 60°C, based on material models developed and implemented in the RAVEN software [22].

section studies post-gelation resin behavior, hence the value before gelation is not relevant in this context.

In general, a direct correlation between degree of cure and cure shrinkage can be found. Furthermore, the shear modulus is significantly lower than the bulk modulus throughout the isothermal cure.

6.3 Experimental setup

The experimental setup used for studying the cure-shrinkage effect in a constrained geometry is shown in Figure 6.10. The setup consisted of a 25 cm long glass tube with inner and outer diameters of 3.0 and 3.5 mm, respectively. Each glass tube was washed with water, rinsed with alcohol, and finally dried with pressurized air.

Carbon-fiber tracers, 1.0 ± 0.5 mm long, with a low volume fraction of $< 0.02\%$, were added to the resin while mixing it with the hardener. At such low volume fraction, the change in properties, e.g. strength and rheology, of the resin is negligible. The purpose of the fiber-tracers inside the resin was to trace the movement of the transparent resin inside the glass tube, and quantify this movement via image processing.

The mix of resin/hardener + tracers was degassed for 10 min, then injected into the glass tube. Vacuum grease was applied to two ends of the tube to avoid resin flow-out without constraining the resin inside the tube. The mix-to-test time was consistently 20 ± 2 min at room temperature, 22 ± 1°C, in all experiments.

A heating pad was placed under the glass tube in the case of experiments at elevated temperatures. In these cases, an aluminum plate was also located on the heating pad, below the glass tube for even temperature distribution along the tube. A glass shield on top of the tube further minimized the airflow, hence temperature variation. Four thermocouples were used to record temperature at center-top and center-bottom, and 3 cm from the two ends of the test tube. The temperature variation between readings from thermocouples was ±1.0°C showing that the temperature was consistent along the length and at the surface of the test tubes.

Time-lapse imaging using a Nikon Stereo microscope captured images with a 2×2 cm^2 window at 50X magnification and at 15-second intervals.

In two control experiments at 60 and 80°C, an extra tube injected with resin was heated simultaneously alongside the main test sample. These control samples included thermocouples inside the

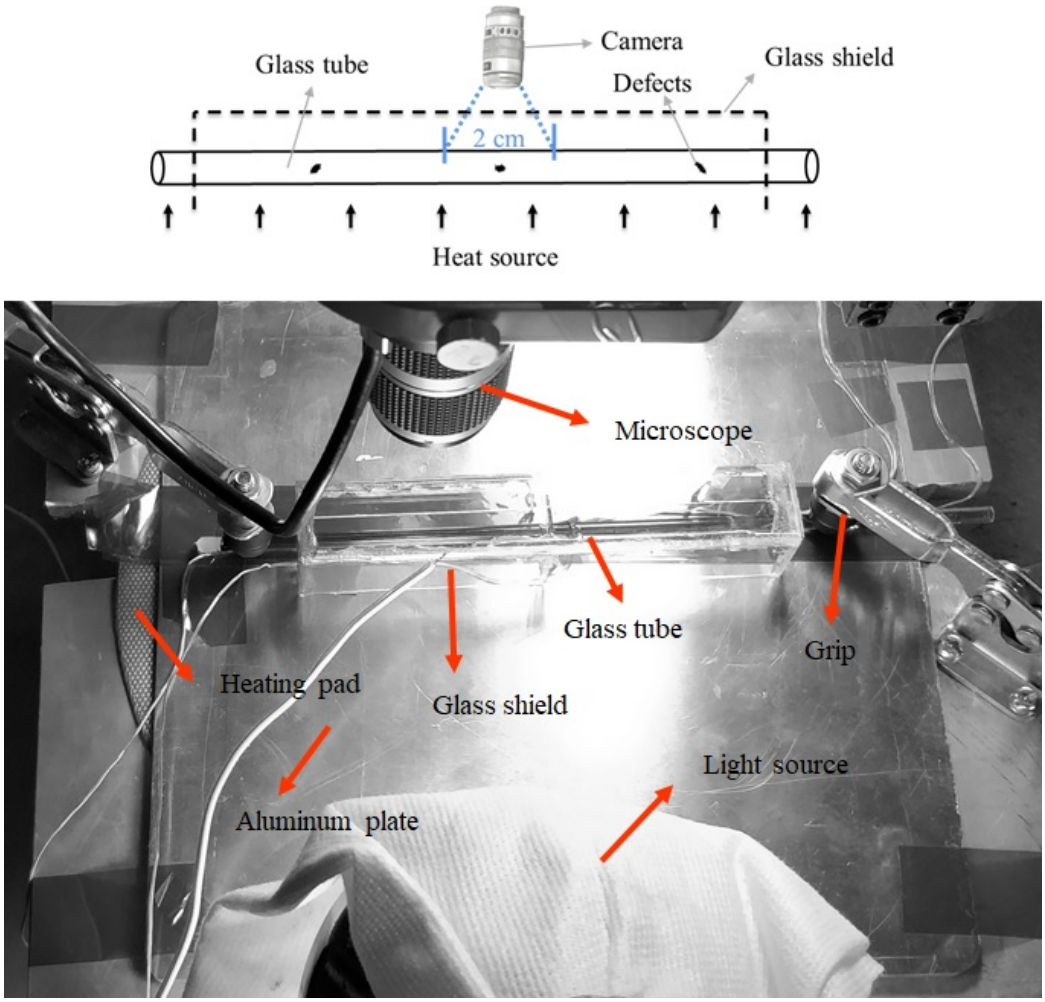

Figure 6.10: The experimental setup used for the constrained resin cure shrinkage experiments.

tube close to the center to evaluate the possible effect of exothermic cure reactions. Results showed temperature variation between the core and surface of the tube remained below 2°C throughout cure. The geometry of the tube (3mm-diameter) contributes to this low temperature-variation, since the generated heat can rapidly be transferred to the surface.

6.4 Analytical methods

6.4.1 Data analysis

The experimental setup used in the present study provided synchronized temperature recordings and time-lapse imaging. The time-lapse imaging enabled tracking of the resin behavior and defect formation/propagation. The corresponding observations were then associated with the resin's cure progress and properties evolution from the temperature recordings.

The manual feature-tracking in the ImageJ software (Fiji) [133] was used to track and quantify the movement of the tracers added to the resin. Due to the high length/radius ratio, radial movement of the tracers was insignificant. Therefore, the data discussed in the following sections is related to tracers movement along the length of the test tube.

In addition to capturing the moment of formation, the propagation rate of any defect was tracked based on size measurements using the ImageJ software. Post gelation defect morphology was further assessed based on circularity defined as the ratio between the minor and major diameter of a defect. Circularity is equal to 1.0 for a spherical defect, and equal to zero for a planar defect.

6.4.2 Numerical simulation

Numerical simulation was employed to evaluate the post-gelation stress evolution during cure. For this purpose, the ABAQUS software and the COMPRO plugin [134] were used. The implemented geometry resembled the experimental glass tubes. The element type for meshing the geometry was C3D20, a 3D 20-node quadratic element for stress analysis. The element size in the mesh was set to 5 mm along the length of the tube and 0.3 mm along the radial direction, Figure 6.11.

Prior to gelation, the resin is not geometrically constrained; the experimental evidence in support of this hypothesis is discussed in the following section. Consequently, the stress development before gelation is negligible. With this consideration, the starting point of the simulations was set to a

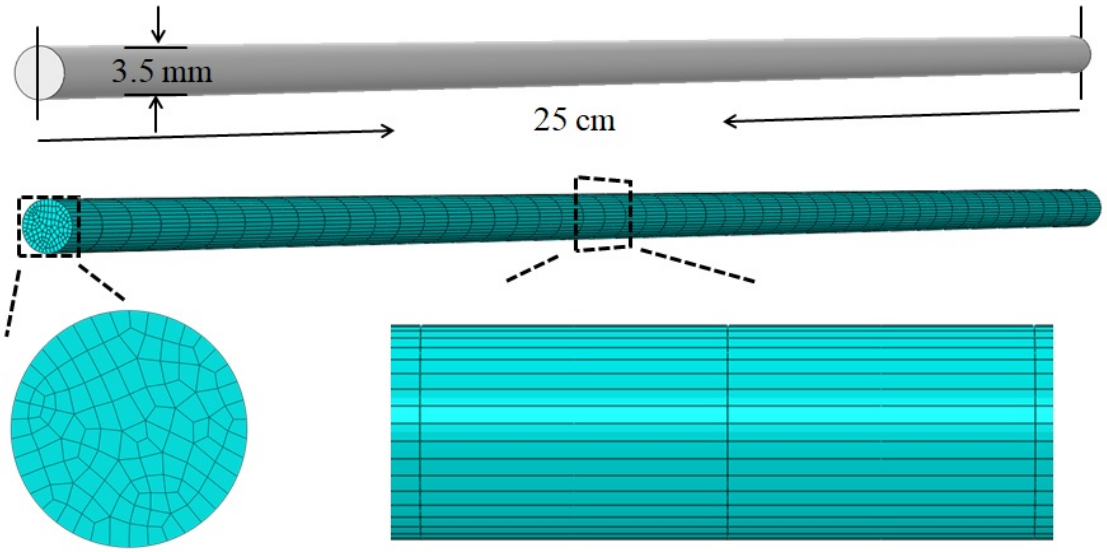

Figure 6.11: Geometry and mesh used for the numerical simulation of the cure shrinkage experiments using COMPRO plugin. Element size is set to 5 mm along the length and 0.3 mm along the radius.

degree of cure of 0.65. According to the material characterization discussed in Section 6.2.4, the resin reaches gelation at this degree of cure.

A fixed boundary condition was applied at the perimeter of the tube, to simulate perfect bonding of the resin to the tube. The two ends of the tube were not constrained throughout the simulations. The goal of the study is to study the effect of cure shrinkage, i.e. free strain, therefore no external loading was applied during simulations. This means that stress development throughout the simulation is solely due to free strain development in a constrained geometry. As part of the problem setup in the ABAQUS software, the minimum and maximum time steps during the analysis are set to 0.1 and 60 s, respectively.

6.5 Results and discussion

6.5.1 Post-gelation resin behavior

The constrained resin's behavior during cure was initially studied using isothermal conditions to eliminate the effect of thermal strain. Isothermal experiments included tests at 25, 40, 60, and 80°C, with repeats at each temperature. Figure 6.12 shows the time-lapse imaging results for an experiment conducted at 25°C. In these images, the added tracers, a preexisting bubble, and formation and growth of the new defects are observed. In the case of the experiment at 25°C, a planar light source was placed under the tubes for better visualization. In all other experiments, the light source remained above the samples due to the heating pads located underneath. Figure 6.13 shows the results from the experiment conducted at 60°C.

Prior to gelation, the resin is a viscous liquid and moves inside the test tube due to the volumetric cure shrinkage. The red dashed lines in Figures 6.12 and 6.13 highlight this movement by the relocation of the tracers. It is noted that due to the location of the tube being observed under the microscope, tracers in the 25°C case move to the left. In the case of the test at 60°C, tracers move in the opposite direction. Additionally, the initial bubbles are in contact with the surface of the glass tube. The resulting surface tension appears to have stopped their movement with respect to the local resin flow.

In all experiments tracers became steady when the resin reached gelation, demonstrating initiation of a geometrical constraint. To further evaluate this, the tracers' movement and the size variation of the preexisting bubbles were tracked using image processing with results shown in Figures 6.15 and 6.14, respectively. A preexisting bubble was not observed in tests conducted at 80°C.

The superimposition of the timescales of fiber movement and bubble growth on the cure kinetics diagrams is shown in Figure 6.16. According to this figure, resin movement initiates and continues with cure. Fiber movement ends around gelation, when the preexisting bubbles start growing.

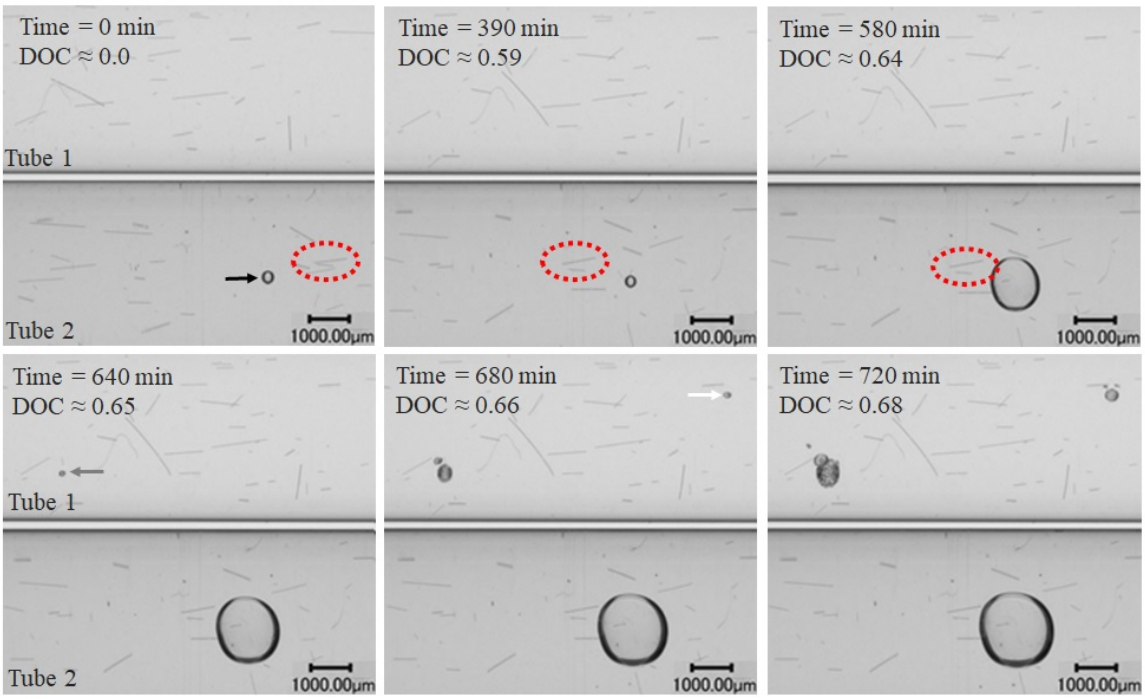

Figure 6.12: Time-lapse images of cure shrinkage-induced growth of a preexisting bubble and formation/growth of new defects during isothermal cure at 25°C. Two tubes are shown in the figure, containing the same resin mixture and curing simultaneously; only tube #2 contains a preexisting bubble.

A displacement of $< 5\mu$m in two consequent time-steps was considered as the criteria for fiber steadiness. The observations related to fibers movement and preexisting bubble growth manifest the geometrical constraint imposed on the resin after gelation and justify the fixed boundary condition setup used in the numerical analysis. In all experiments, the initiation of the geometrical constraint correlates with the gelation time. However, in the case of the test at 25°C, the resin became constrained shortly before gelation, DOC ≈ 0.59.

The expansion of the preexisting bubbles was not due to moisture diffusion. First, experiments were conducted isothermally. Therefore, volatile solubility remained constant before and after gelation. Second, the degassing step during sample preparation ensured that minimal amounts of volatiles were dissolved in the matrix. Additionally, control experiments at 25°C were conducted

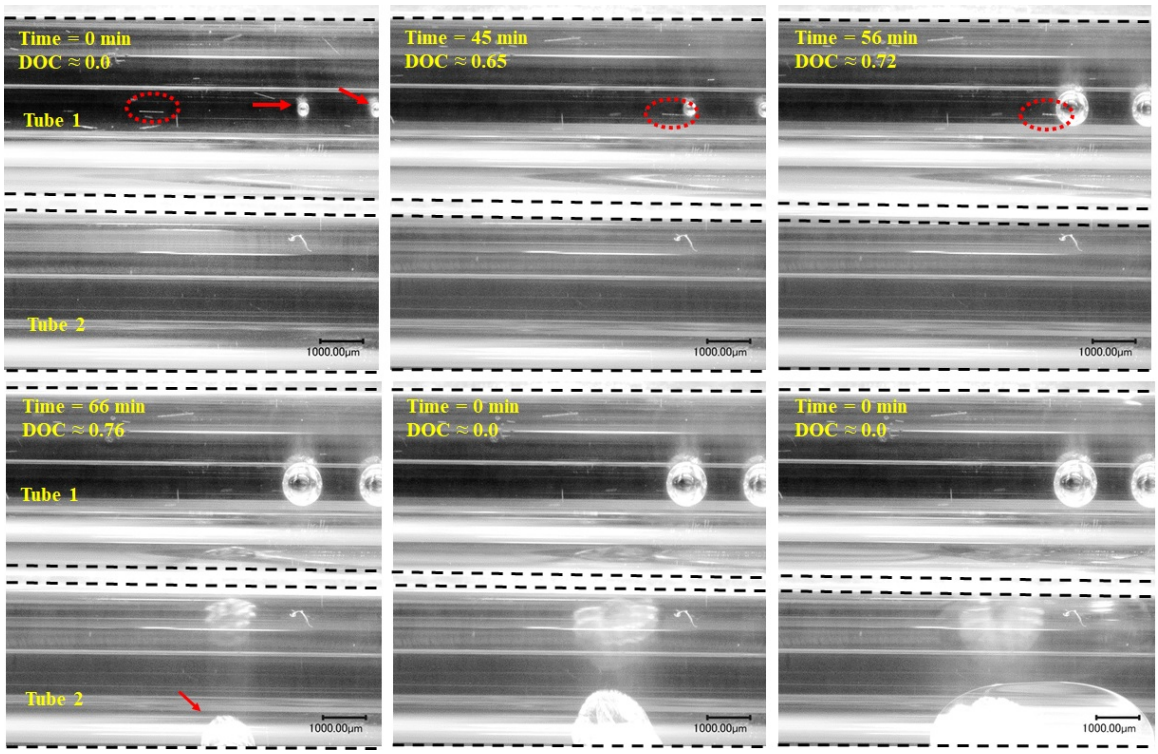

Figure 6.13: Time-lapse images of cure shrinkage-induced growth of a preexisting bubble and formation/growth of new defects during isothermal cure at 60°C. The black dashed lines indicate the surface of the tubes.

with resin desiccated in a silica-gel environment for three days, prior to mixing with hardener. No difference was detected in comparison to other experiments, suggesting that volatiles are not the cause of the observed bubble expansion. As cure shrinkage leads to development of hydrostatic tensile stresses, volatile solubility inside the resin may change. This effect has not been studied in the present work.

6.5.2 Numerical simulation of constrained resin

The COMPRO plugin built into the ABAQUS software was used to investigate the stress development inside the resin during cure and after gelation, Section 6.4.2. Simulation trials were run for

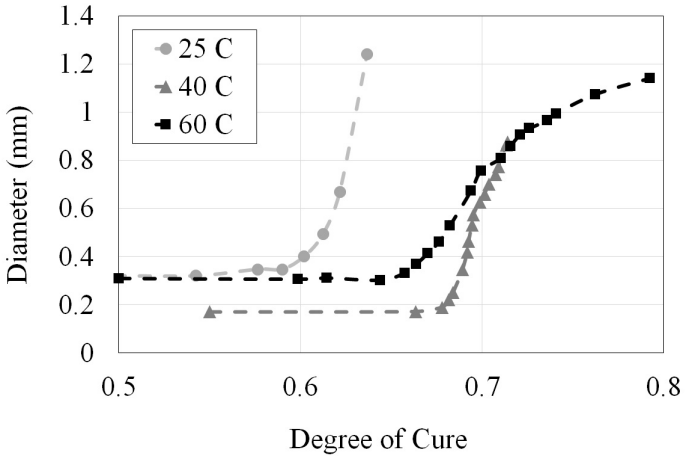

Figure 6.14: Preexisting bubble size variation during isothermal cure at different temperatures. Every point represents one size measurement. At each temperature one bubble was tracked.

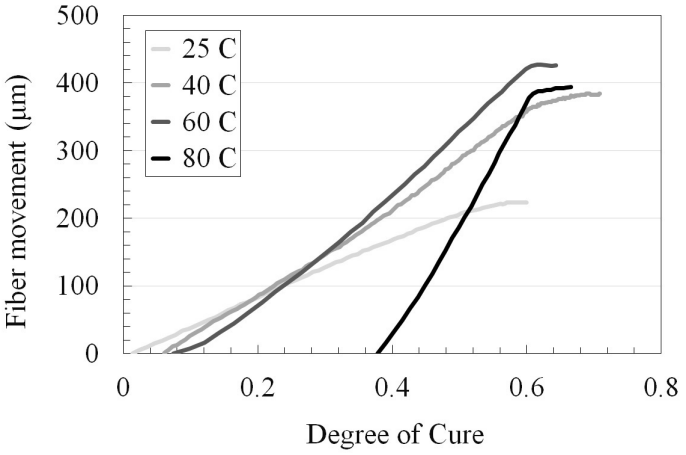

Figure 6.15: Movement of a representative tracer inside the resin during cure at different temperatures. Movement tracking in the case of the test at 80°C started when DOC $\approx$ 0.37.

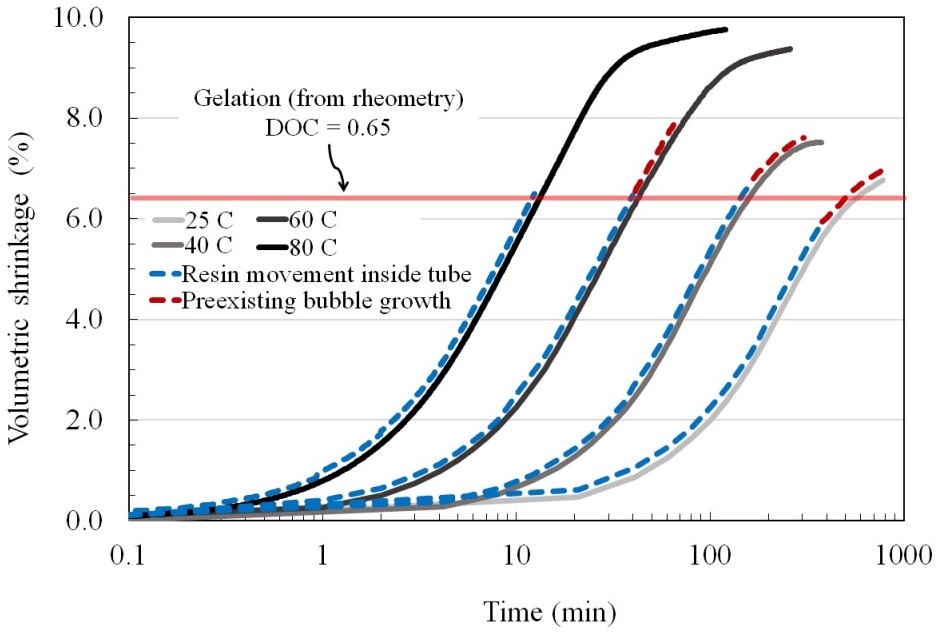

Figure 6.16: Timescale of the tracer movement and growth of preexisting bubbles, superimposed on the volumetric cure shrinkage graphs. Volumetric cure shrinkage was found to be a linear function of cure progress, refer to Section 6.2.2.

isothermal cure tests conducted at 40, 60, and 80°C. Due to the very long cure at 25°C, numerical simulation at this temperature was not performed.

The numerical results of hydrostatic and shear stress development in the resin due to cure at 40°C until DOC = 0.75 are shown in Figure 6.17. The two ends of the tubes were not constrained during simulations, as in the experimental test. The results show that the hydrostatic tensile stress is maximum at the central regions of the tube. Shear stress is maximum at the surface of the tube and at regions very close to the edge of the tube. Figure 6.18 shows the shear stress results extracted along the length and on the surface of the tube. The results in this figure are also related to DOC =0.75.

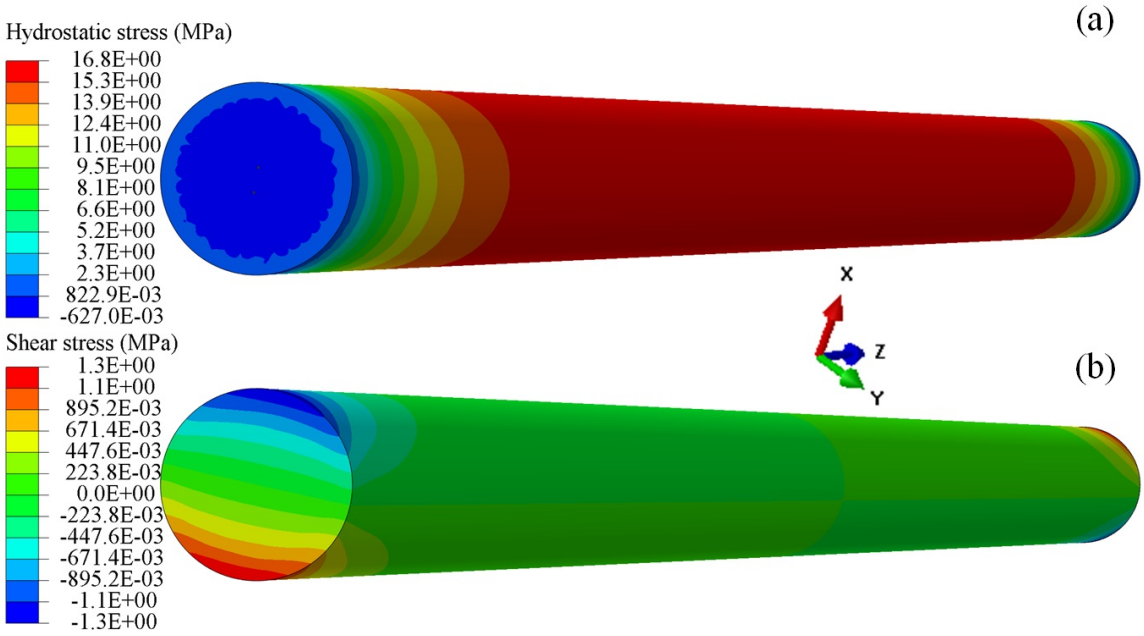

Figure 6.17: Numerical simulation results of (a) hydrostatic and (b) shear stresses (τ_{xz}) for the constrained resin curing isothermally at 40°C. Results related to DOC = 0.75.

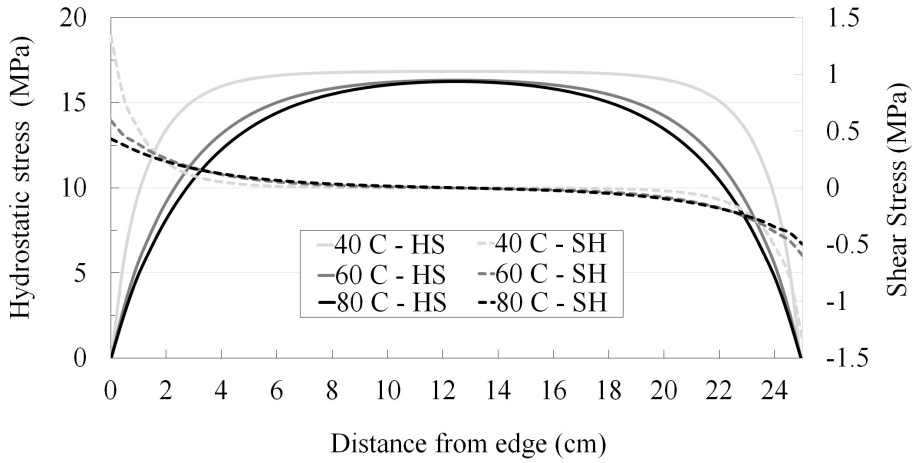

Figure 6.18: Numerical simulation results of hydrostatic and shear stresses for the constrained resin cured isothermally until DOC = 0.75. Shear stress results are extracted along the length and on the surface of the tube (τ_{xz}). Hydrostatic stress (σ) in the graph corresponds to the results along an axis at the center of the tube.

6.5.3 Internal stress-induced defects

According to the time-lapse images in Figures 6.12 and 6.13, new defects form as cure progresses after gelation and before glass transition, where the resin is still rubbery. These defects are manifestations of internal stress development in a geometry constrained after gelation.

A comparison between the internal surface of a preexisting bubble and a spherical post-gelation defect, Figure 6.19, further highlights the fracture characteristic of defects forming after gelation. The internal surface of the spherical defect forming after gelation is jagged with features demonstrating matrix rupture. In contrast, the internal surface of preexisting bubbles is smooth. The smooth surface is a characteristic of bubbles in a liquid matrix, which is the state of the resin before gelation.

Given the observed characteristics, the formation of post-gelation defect creates volume. This is evidence of cavitation and resembles the initiation of the crazing deformation mechanism [135]. This mechanism is in contrast with the shear yielding that occurs approximately at a constant volume. Cavitation initiates with the formation of microvoids that nucleate at high stress points in the polymer created by scratches, flaws, cracks, dust particles, and molecular heterogeneities [136]. Furthermore, volume creation due to cavitation requires the presence of hydrostatic stresses. The stress state at the location of defect formation is discussed later in this chapter.

The formation of initial defects during isothermal cure at different temperatures and their associated degree of cure are presented in Figure 6.20. A DOC of ≈ 0.76 in this figure tends to be the critical point for defect formation. Defect formation also tends to occur earlier during the tests at 25°C, DOC ≈ 0.65. Room temperature variation is a possible source of the observed deviation. In all cases defect formation occurs before the resin vitrifies.

A notable finding was that the morphology of the post-gelation defects varies with cure temperature, Figure 6.21. As the cure temperature increased, a transition from spherical defect shape to planar defect morphology was observed.

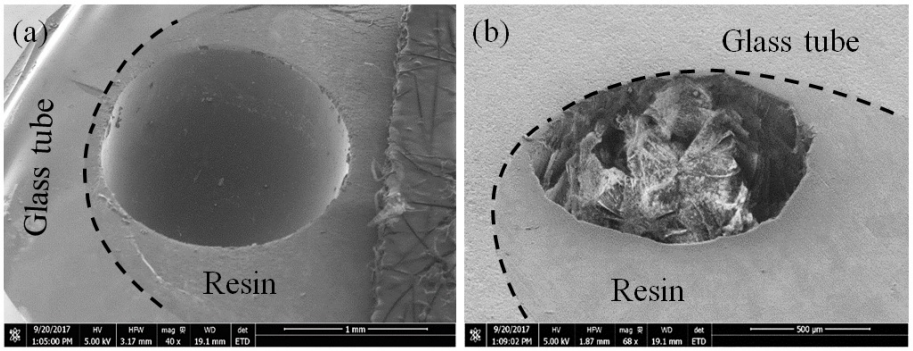

Figure 6.19: Cross sections of the resin cured inside the tube showing internal surfaces of (a) a preexisting bubble expanding after gelation, and (b) a spherical defect forming after gelation; both tubes are related to the isothermal cure at 25°C.

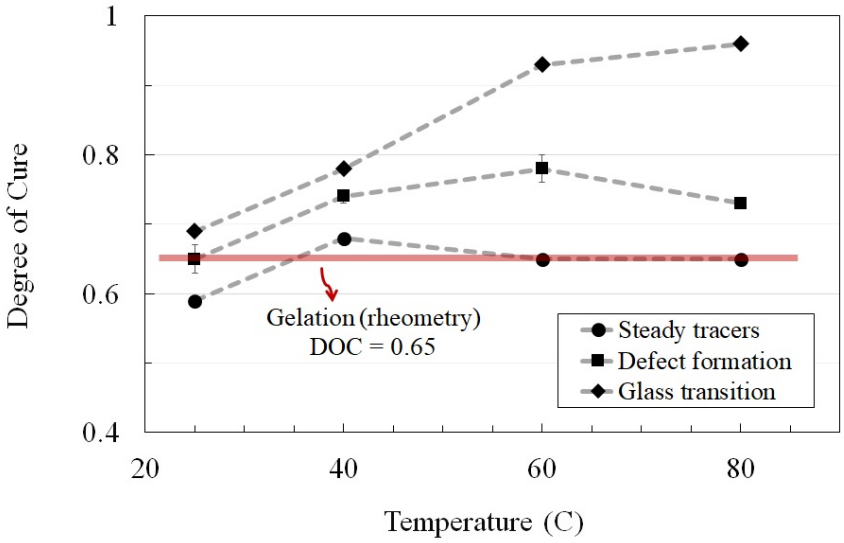

Figure 6.20: Graphs showing degree of cure when the first defect was detected, the tracers became steady (stopped moving), and glass transition occurred, at different isothermal cure temperatures. The accuracy of the DOC reported is ±0.01.

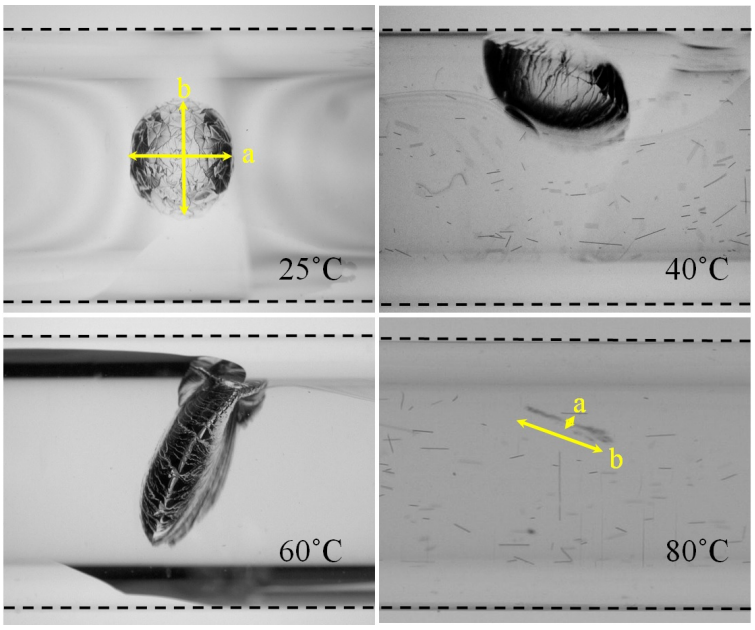

Figure 6.21: Common defect morphologies observed at different isothermal cure temperatures. Black dashed lines highlight the glass tube surface. Circularity was calculated as a/b shown in this figure.

The planar defects formed after gelation and before glass transition had a ragged surface, demonstrating a radial propagation pattern. This characteristic distinguished these defects from cracks formed after vitrification, which had a smooth surface, Figure 6.22. Matrix cracking after vitrification happens due to thermal stresses forming during cool-down. Post glass transition crack formation was rarely observed in the present experiments, and was not included in the experimental data analysis.

The bar chart in Figure 6.23 shows the spatial distribution of the defects along the length of the test tubes. In this graph, each test tube was divided into 5 sections of equal length and the total number of defects in each of these sections was counted. Generally, defects were found in all regions, however, a higher concentration was observed at the central regions of the tube. No apparent correlation was observed between cure temperature and the spatial distribution of defects.

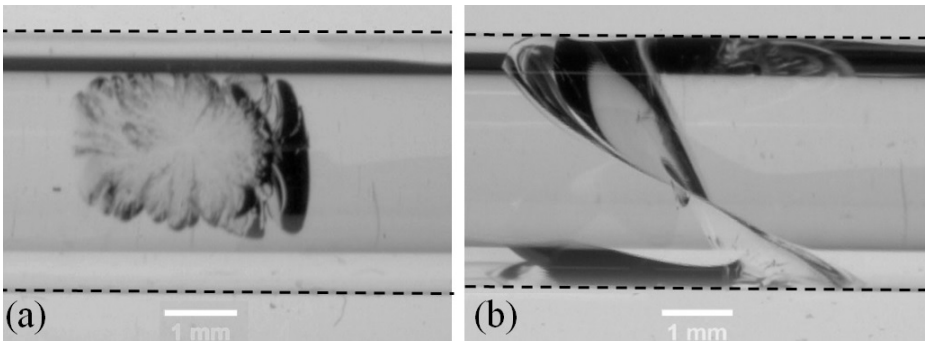

Figure 6.22: Surface of the (a) planar defects forming after gelation and before glass transition, and (b) a crack formed after glass transition.

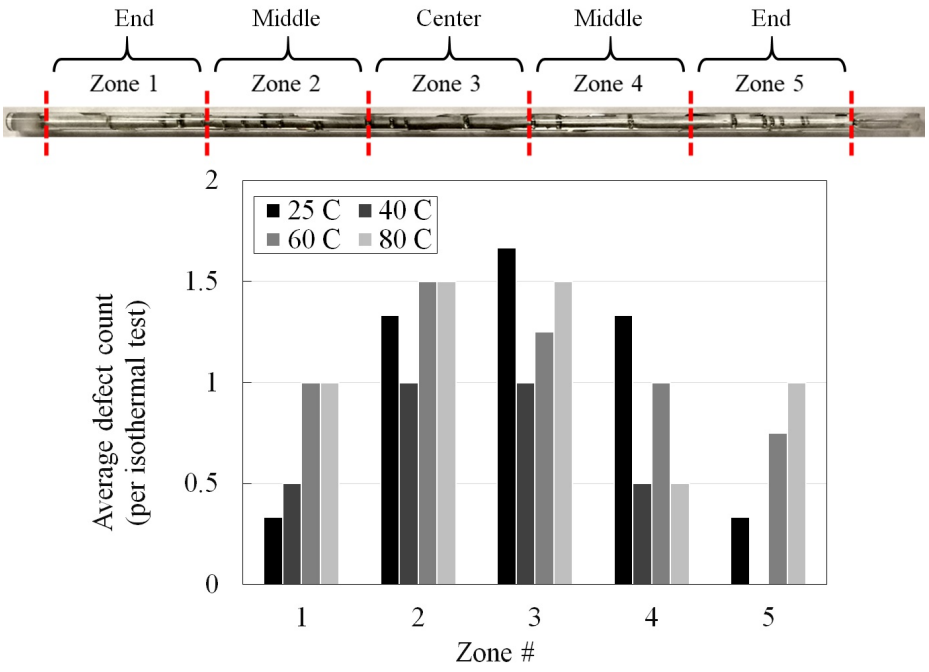

Figure 6.23: Spatial distribution of all shrinkage-induced defects detected in isothermal cure tests. Preexisting bubbles are not included in this chart.

The higher defect concentration in the central regions can be explained by the stress variation along the tube as shown in Figure 6.24. In this figure, hydrostatic and shear stresses are based on the numerical results presented in Section 6.5.2. Specifically, the average stress values in every 5 cm of the numerically simulated test tubes, Figure 6.18, were calculated. Then, stress values were normalized with respect to the maximum hydrostatic and shear stresses, and finally averaged over all cure temperatures. The error bars in this figure represent the stress value variation at different isothermal cure temperatures.

A direct correlation was found between the defect concentration and hydrostatic stress. Specifically, the highest defect count was observed in the central regions of the tubes where hydrostatic stress is at its maximum. In contrast, the shear stress in this region is negligible. Shear stress increases at regions of the tube close to two ends where defect count was the lowest. It is worth noting that in these regions hydrostatic stress is not negligible. In conclusion, shear stress does not correlate with post-gelation defect count.

Another important conclusion is that the nature of the internal stress, hydrostatic versus shear, is not a source of change in defect morphology. The shear stress in the central zone where most defects, including planar ones, were detected is effectively equal to zero, Figure 6.18.

Defect morphology was quantified using circularity defined as the ratio between the minor diameter over major diameter of a defect, 'a' and 'b' in Figure 6.21. For example, in the case of a spherical defect, circularity is equal to 1.0 and it is equal to zero for a planar defect.

A comparison between the average defect circularity, defect propagation rate, and shrinkage rate in Figure 6.25 suggests that the variation of cure rate with temperature influences defect morphology. Specifically, at higher temperatures where the defect propagation rate is higher, lower circularity is observed. In this figure, shrinkage rate was calculated at the degree of cure of 0.65. A quantitative study of the rate dependency of the defect morphology is out of the scope of the present study.

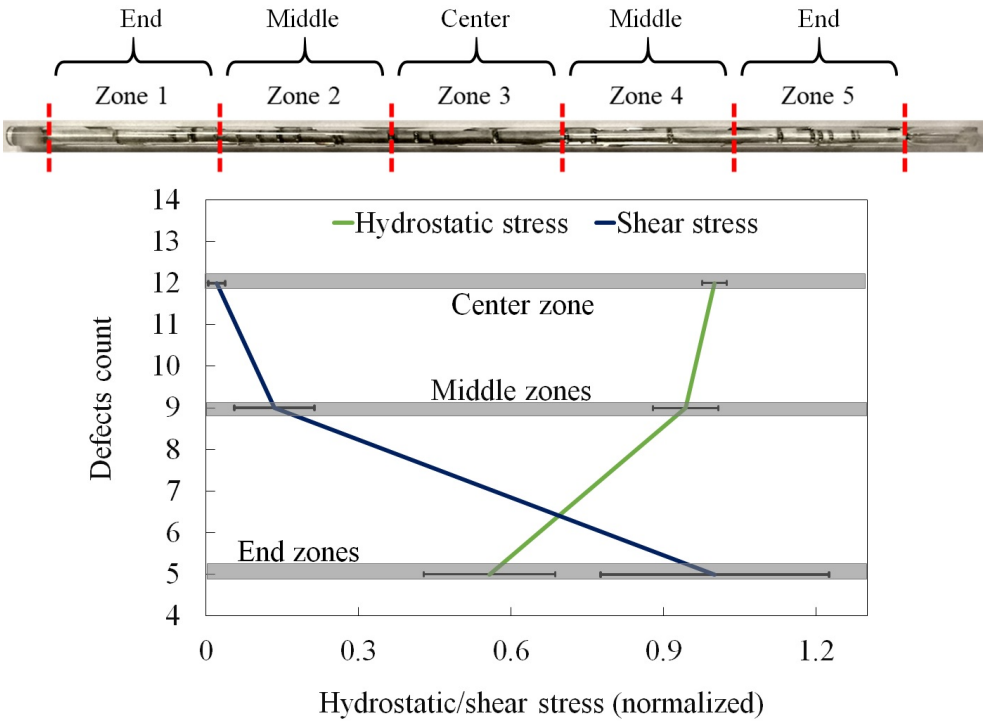

Figure 6.24: Variation of the shear and hydrostatic stresses along the length of the tube, and their effect on total defect counts. Preexisting bubbles are not included in the counts. Stress values are averaged over zones along the length and cure temperatures, based on the results in Figure 6.18. The error bars show stress variation with cure temperature.

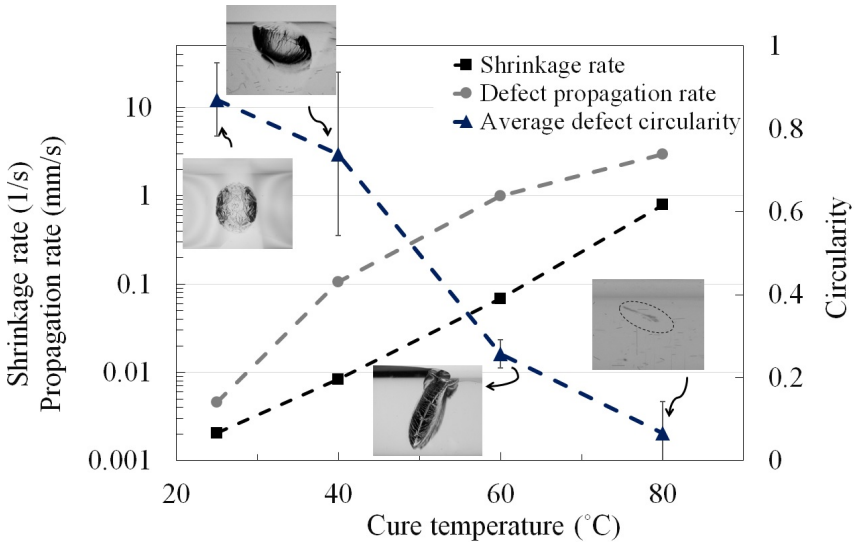

Figure 6.25: Cure temperature effect on post-gelation defect morphology, shrinkage rate, and defect propagation rate. Shrinkage rate was calculated at DOC = 0.65.

6.6 Cure cycle design

6.6.1 Stress at defect formation

The constrained resin behavior during cure and after gelation was studied using isothermal-cure experiments at different temperatures. The key findings with regards to defect formation were that defects form after the resin is completely constrained due to gelation, and that post-gelation defect formation is hydrostatic stress-driven. The hydrostatic stress needed for defect formation must be sufficient to provide the surface free-energy to nucleate cavitation and must also be sufficient for the nucleated center to grow. Different studies in the literature investigated criteria for cavitation, and crazing initiation, as a function of intrinsic material properties as well as hydrostatic stress component [137]. In the present study, only the hydrostatic stress component is considered as a criterion for defect formation. This approach was justified given the statistical nature of the cavitation formation that depends on matrix and molecular inhomogeneities rather than sole material properties.

The stiffness tensor was considered solely a function of the bulk modulus in the case of the rubbery resin, Equation 2.27. With this consideration, the hydrostatic stress developing during cure was calculated as:

$$\begin{aligned} \sigma &= \int_0^t K \frac{dV}{3d\tau} d\tau \\ dV &= 3(d\varepsilon + d\varepsilon_{free}) \\ d\varepsilon_{free} &= d\varepsilon_{cure} + d\varepsilon_{thermal} \end{aligned} \tag{6.5}$$

where, K is the resin bulk modulus, dV is the volumetric change, $\varepsilon_{thermal}$ is thermal free strain, and ε_{cure} is cure shrinkage free strain. Due to the geometrical constraint, $d\varepsilon \approx 0$, and in the case of the isothermal cure $d\varepsilon_{thermal} = 0$. Given time-lapse images from microscopy, the hydrostatic stress at the time of the first defect formation can be calculated.

Table 6.3: Hydrostatic tensile stress at defect formation observed during cure, and calculated based on Equation 6.5.

Temperature (°C)	25	40	60	80
Stress value (MPa)	3.0±2.0	15.0±2.0	22.0±4.0	12.0±1.0

An example is shown in Figure 6.26 for the isothermal test at 60°C. In this figure, the hydrostatic stress is equal to the cure shrinkage-induced stress, since the thermal free strain is equal to zero. As shown in the graph, the first defect formation was detected when the degree of cure is about 0.76 (Figure 6.20) and the hydrostatic tensile stress is about 19.5 MPa.

Similarly, the stress values at other temperatures were calculated with values ranging from 12-22 MPa, Table 6.3. This wide range of critical stresses is due to the statistical nature of the cavitation that depends on matrix and molecular inhomogeneities. The critical stress value for the test at 25°C is very low which corresponds to defect formation at the low degree of cure at this temperature. It is worth mentioning that the ultimate tensile strength of the fully-cured Rhino 1411 fast-cure (DOC = 1.0) is about 71 MPa, according to the manufacturer [129]. Notably, the variability of the stress values, maximum 20%, is higher than the variability of the calculated degree of cure, maximum 3%, at the time of defect formation. This is expected from the fast development of the mechanical properties of the resin during cure after gelation, Figure 6.9.

6.6.2 Cure cycle design approach

The understanding developed based on the isothermal tests was used to design cure cycles to suppress internal stress-induced defect formation after gelation and before glass transition. The primary idea behind the approach is to avoid hydrostatic tensile stress development above the critical strength found through isothermal experiments, i.e. 12-22 MPa. Since, this is a relatively wide range of stress, a conservative approach would consider the minimum value of the range for design purposes.

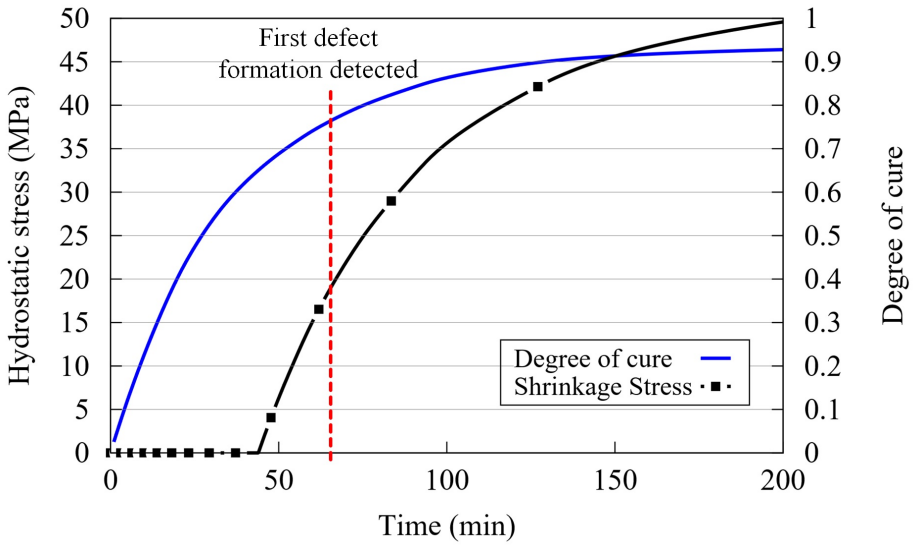

Figure 6.26: Calculated hydrostatic stress development during isothermal cure at 60°C. The red dashed line shows the timing of the first defect formation detected via time-lapse imaging.

The methodology to avoid excessive stress development starts with curing the resin at a relatively low temperature until gelation. At this state, the resin becomes constrained, therefore a subsequent temperature ramp causes development of compressive stresses due to the thermal free strain. These stresses counterbalance the cure shrinkage-induced tensile stress and eliminate the driver for defect formation. The balance between compressive and tensile stresses can be controlled by cure cycle adjustments based on characterized material properties and stress calculations, Equation 6.5.

Figure 6.27 shows an optimized cure cycle in which the hydrostatic tensile stress remains below critical values until glass transition occurs. The thermal free strain caused by the thermal expansion of the resin generates compressive stresses, hence the negative values. This compressive stress dominates the tensile, cure-induced stresses. The initial hold temperature, temperature ramp rate, and the second hold temperature are important parameters with regards to cure cycle optimization. These parameters were found using a trial-and-error approach in the case of the optimal cure cycle.

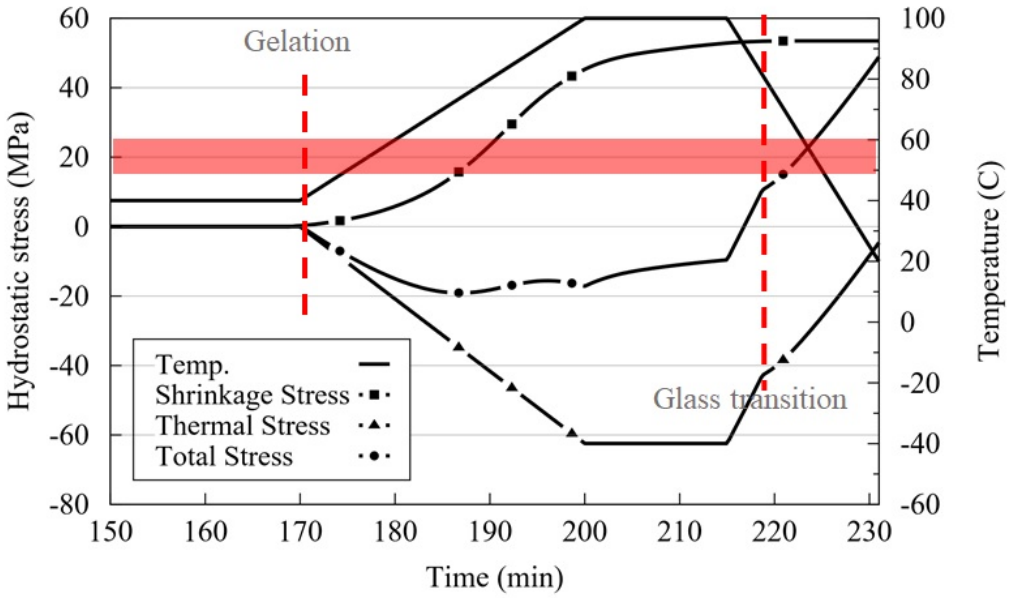

Figure 6.27: Variation of the cure shrinkage, thermal and total stresses during cure for an optimized cure cycle that suppressed defect formation. Regions highlighted in red represent the critical hydrostatic tensile stress region, 12-22 MPa.

The glass tube containing the resin cured using the optimal cycle is compared with a glass tube containing cured resin including defects in Figure 6.28.

To confirm that post-gelation defects were suppressed solely due to cure cycle optimization, five different non-optimal cycles were experimentally examined. All these cycles led to cure defects with the stress level at the time of defect formation shown in Table 6.4. Defect formation in all cases happened at the post-gelation state, before glass transition. In the case of trials 3, 4, and 5, defects formed during second temperature hold. In other cases, the critical stress values were reached during temperature ramp.

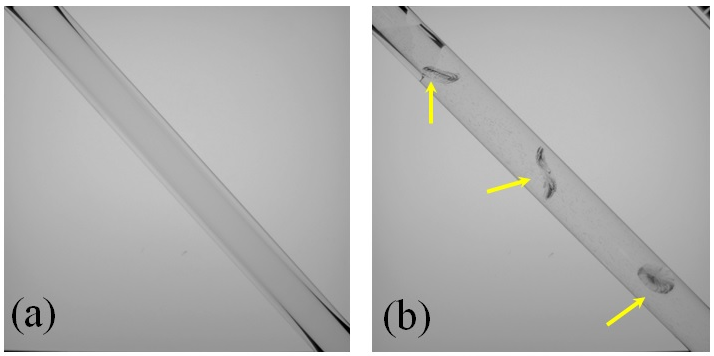

Figure 6.28: The result of curing the constrained resin using (a) the optimal cycle in Figure 6.27, and (b) a non-optimized cycle leading to defect formation. Arrows mark the location of defects.

Table 6.4: Experimental trials conducted to evaluate the cure cycle optimization approach. The cycles vary in initial hold temperature (T_1), temperature ramp rate (R_1), and the second hold temperature (T_2). Critical stress demonstrates the calculated stress at the time of defect formation.

Trial	T_1 (°C)	R_1 (°C/min)	T_2 (°C)	Critical stress (MPa)
Defect-free reference	40	2.0	100	–
1	No hold	1.0	90	14.3
2	No hold	3.0	80	19.5
3	60	2.0	80	12.5
4	60	10.0	80	14.4
5	60	2.0	90	12.5

6.7 Summary

In this study, defect formation in constrained resin after gelation and before glass transition was investigated. The experimental setup allowed direct observation of the resin behavior as well as defect formation/propagation. It was observed that the resin becomes geometrically constrained after gelation. Cure continuation and the resulting internal stress development led to defect formation.

Moreover, stress development inside the resin was investigated via numerical simulation. The results confirmed that defect initiation is hydrostatic stress driven. Furthermore, it was found that defect morphology is cure temperature-dependent. More importantly, this dependency is related to the variation of the cure rate with temperature.

The findings based on the isothermal experiments were used to systematically optimize the cure cycle and avoid shrinkage-induced defects. The presented approach relies on a comprehensive material characterization and tracking of the hydrostatic tensile stress throughout cure. The goal is to avoid tensile stress development above the strength limit of the rubbery resin. This approach takes advantage of the thermal expansion of the gelled resin to counterbalance the cure shrinkage-induced tensile stresses.

Chapter 7

Conclusions, contributions and future work

7.1 Conclusions

Defects forming in the resin matrix of fiber-reinforced polymeric composites during processing dramatically reduce the in-service performance of manufactured parts. Therefore, process engineers spend significant time and resources to find the optimal manufacturing conditions to avoid matrix defects. In this area, trial-and-error is still the dominant approach for process design and optimization. The main reason is that matrix defect formation is a complex problem with several sources and mechanisms. Although a decade of research has already uncovered the main sources of such defects, the developed knowledge has not been adequately translated to real-world manufacturing practices. For this purpose, the source of the defect, the underlying physics, the corresponding analytical model, and its application in process design should be addressed.

The present study investigated different sources of matrix defects throughout the whole processing spectrum, from the liquid resin state to its rubbery state just before glass transition. For this purpose, the bulk of the work was divided into two regions before and after gelation. Before

gelation the resin is liquid-like, i.e. it flows upon applying a shearing force. At this stage, any matrix defects are in the form of porosity, regions of the fiberbed that are devoid of resin. Volatile release, entrapped air, and incomplete resin infiltration are the main sources of porosity. Volatile release is controlled by diffusion mechanisms. However, the dynamics of air entrapment and incomplete resin infiltration are explained by transport mechanisms. Therefore, the sources of porosity before gelation were studied in two sections. The three-dimensional structure of the resin after gelation suppresses bubble growth and resin infiltration mechanisms, hence these sources of porosity. However, free strains in a constrained geometry can lead to internal stress development and post-gelation defects. Therefore, the research work in the present study was conducted in three parts.

The application of existing bubble dynamics theories to predict stable and unstable moisture-driven bubble growth with cure temperature and resin pressure was examined. A simple analysis concluded that stable bubble growth is negligible in the context of composite manufacturing. The criterion for unstable bubble growth predicted the observed temperature for bubble growth within 5°C for a range of moisture conditions. The criterion used for unstable growth was derived based on an equilibrium condition, therefore, time-dependent effects are not explicitly included. This is consistent with the present work's objective to predict the onset of growth but not the time-dependent evolution. Moreover, it was shown that a temperature hold below the critical temperature until resin gelation can suppress moisture-induced bubble growth. This validates an analytical approach to avoid bubble growth and porosity by cure cycle design for any moisture condition, even for ambient pressure processes such as out-of-autoclave prepreg processing.

The presented bubble growth criteria assumes that moisture can only be transported within the RVE between the resin and the air–water bubble. Experiments were designed to mimic this condition by suppressing water vapor escaping the test sample. In real composite structures, there are transport paths for water dissolved in the resin within partially impregnated plies. Examples are laps and gaps in the lay-up that allow moisture to be transported away from the resin towards the

vacuum system during debulk. However, these gas and moisture transport pathways will close off when resin flow progresses due to the increase in temperature early in the cure cycle. This means that the moisture level in the resin when the transport pathways are closed off and moisture diffusion to enclosed bubbles becomes important will always be less than expected based on the initial relative humidity. This makes the presented bubble growth suppression approach conservative and useful for practical applications.

The porosity formation due to gas entrapment and resin infiltration was investigated through the underlying transport mechanisms. Gas transport in composite manufacturing relies on the application of vacuum pressure, and the applied pressure is the main driving force for resin transport. The experimental setup used isolated the effect of vacuum and applied pressure on final porosity. The results showed that resin infiltration directly influences gas transport by reducing the available pathways for gas transport, i.e. initial porosity. Subsequently, a fully coupled transport model was developed to explicitly include the resin and gas interaction during processing of partially-impregnated prepregs. The model predicted the observed trends in the experimental data based on material parameters from the literature.

In addition to offering a physics-based model, the present study demonstrated that the typical assumption of constant porosity in the continuity equation for the non-saturating phase (i.e. gas) is not plausible in the context of composites manufacturing. Moreover, by including general physics, the developed model is not limited to a specific processing method. For example, the model can capture resin flow under applied pressures ranging from below-atmospheric pressure (causing desaturation) up to high ambient pressures in an autoclave. Another feature to be noted is the application of a conditional boundary-condition assignment scheme. This allows for the prediction of resin infiltration into regions disconnected from the vacuum channels prior to cure or regions isolated due to resin infiltration during cure.

The transition from a liquid to a rubbery state of the resin complicates studies on the resin behavior after gelation. Furthermore, since the rubbery resin is difficult to handle, process-induced defects after gelation are typically studied based on the cured and solidified resin after glass transition. The experimental setup used in this study allowed direct observation of the resin behavior as well as defect formation/propagation within the critical processing window from gelation to glass transition. Results showed that the resin becomes geometrically constrained after gelation and the resulting internal stress development leads to defect formation.

By studying the distribution of the defects and using a numerical simulation of the experiments, it was found that post-gelation defect formation is hydrostatic stress-driven, and that the morphology of the defects varied from spherical to planar shapes with isothermal cure temperature. Through further analysis, it was concluded that the variation of the post-gelation defect morphology is related to the variation of the cure kinetics, hence shrinkage rate, with cure temperature.

More importantly, this study examined an analytical approach to avoid post-gelation defects based on a comprehensive material characterization and stress evolution tracking during cure in a constrained geometry. In a real composite structure, the resin may not be completely constrained or resin-rich regions may not be abundant. However, the setup and analytical approach used in this study can be used as a conservative analytical approach for cure cycle design to keep the internal stress evolution in critical zones in check and avoid defects. Considering the emphasis in the literature on controlling stresses at the matrix level, the present study also reduces the internal stress level at regions where defect formation is not anticipated such as regions with a high volume fraction of fiber.

7.2 Contributions

The primary contributions of this study include:

- As a result of the representative experiments, the underlying physics of different mechanisms for defect formation have been examined and better understood. This can guide future endeavors for detailed process simulation by providing insights about the key mechanisms for defect formation during processing of the resin matrix.

- In addition to knowledge development, analytical models and approaches have been introduced and validated for process optimization to avoid defects. The application of these models can reduce the manufacturing cost by replacing the conventional trial-and-error approaches for process design and trouble-shooting.

- The most important contribution of the work is to provide evidence for the hypothesis that cure cycle design is an effective mean for defect-free manufacturing. This becomes highly valuable in cases were changing the matrix resin to reduce defects is not a viable option.

Specific contributions of the present study include:

- The experimental work on moisture-induced porosity shows that the conventional bubble dynamics model is applicable in the case of composites manufacturing using thermosetting resins.

- In the context of composites manufacturing, moisture-induced bubble growth in the gelled resin may not be as important as some studies in the literature have emphasized. Resin gelation was used as a criterion for stopping the moisture-induced bubble growth, in this study. However, internal stress-induced bubble growth in the rubbery resin should be accounted for to accurately track porosity evolution during manufacturing.

- The assumption of constant porosity or that the porous geometry only deforms due to compaction is not plausible in the context of prepreg-based composites manufacturing. The contribution of resin infiltration in changing the geometry of the porous media with respect to gas transport should be considered using a fully coupled transport model.

- Experimental evidence show that crack-like defects can form in a hydrostatic mode and inside the rubbery resin. Moreover, a distinction has been made between these defects and matrix cracking after glass transition.

7.3 Future work

This study investigated the underlying physics of three different sources for process-induced matrix defects. Through the developed knowledge, analytical models were developed for process design, and a foundation has been provided for further fundamental studies. Suggestions for studies and tasks that would expand the utility of the proposed approaches in composites manufacturing are presented below.

- The focus of the study considering moisture-induced porosity was to suppress any bubble growth. It would be valuable to study the extent of bubble growth and the effect of processing parameters on the growth rate. Such analysis would add a level of accuracy to the process design by providing a tool to identify bubbles formed before resin reaches gelation.

- Moisture desorption in the presence of open transport channels is considered as a source term in the gas transport problem. This study used desiccated prepregs for transport studies, hence the corresponding source term was set to zero. A valuable extension to the experimental work related to the coupled transport would be to examine the effect of dissolved moisture on gas extraction and porosity evolution.

- The scalability of the proposed coupled transport model has been examined through analytical analysis. An experimental evaluation using laminates of different sizes would add a higher level of confidence to the application of the coupled transport model.

- An investigation on the mechanism behind the cure rate-dependency of the post-gelation defect morphology may reveal currently unknown approaches for a more advanced cure cycle design. Such analysis on rate-dependent resin behavior would require characterization of the viscoelastic properties of the resin. Having such a model readily available would allow a deeper analysis of the existing experimental results.

- For the sake of consistency, the present study used a fixed geometry for investigating the internal stress-induced defects, wherein shear stress was negligible. An extension to this study would examine the effect of different constrained geometries and possibly shear stresses on the post-gelation behavior of the resin and defect formation.

- Another extension to this study could evaluate the behavior of the gelled resin in the presence of continuous fibers inside the glass tube. This could potentially reveal interesting results about the interaction between the fiber and the gelled resin such as strengthening of the resin or deformation of the fibers in the form of wrinkles due to the longitudinal compressive forces.

- This study provided different components of a comprehensive analytical approach for cure cycle design to avoid matrix defects. An integrated multi-objective optimization approach would be valuable by automating the search for an optimal cure cycle based on the developed models.

Bibliography

[1] Janna Fabris, Dan Lussier, Navid Zobeiry, Christophe Mobuchon, and Anoush Poursartip. Development of standardized approaches to thermal management in composites manufacturing. In *Society for the Advancement of Material and Process Engineering (SAMPE)*, Seattle, WA, USA, 2014. → page 1

[2] Dominic Gates. Boeing celebrates 787 delivery as program's costs top $32 billion. *The Seattle Times*, 2011. URL http://old.seattletimes.com/html/businesstechnology/2016310102_boeing25.html. → page 1

[3] Theo Leggett. A350: The aircraft that airbus did not want to build. *BBC*, 2013. URL https://www.bbc.com/news/business-22803218. → page 1

[4] G Fernlund, J Wells, L Fahrang, J Kay, and A Poursartip. Causes and remedies for porosity in composite manufacturing. In *IOP Conference Series: Materials Science and Engineering*, volume 139, page 12002. IOP Publishing, 2016. → page 2

[5] Kenneth J Bowles and Stephen Frimpong. Void effects on the interlaminar shear strength of unidirectional graphite-fiber-reinforced composites. *Journal of composite materials*, 26(10): 1487–1509, 1992. → page 2

[6] Mahoor Mehdikhani, Nikolay A Petrov, Ilya Straumit, António R Melro, Stepan V Lomov, and Larissa Gorbatikh. The effect of voids on matrix cracking in composite laminates as revealed by combined computations at the micro-and meso-scales. *Composites Part A: Applied Science and Manufacturing*, 117:180–192, 2019. → page 2

[7] C Li, N Zobeiry, S Chatterjee, and A Poursartip. Advances in the characterization of residual stress in composite structures. In *Society for the Advancement of Material and Process Engineering (SAMPE)*, Seattle, WA, USA, 2014. → pages xiii, 3, 35

[8] R S Trask, S R Hallett, F M M Helenon, and M R Wisnom. Influence of process induced defects on the failure of composite T-joint specimens. *Composites Part A: Applied Science and Manufacturing*, 43(4):748–757, 2012. → pages xiii, 3, 35

[9] Mahoor Mehdikhani, Eline Steensels, Axelle Standaert, Katleen AM Vallons, Larissa Gorbatikh, and Stepan V Lomov. Multi-scale digital image correlation for detection and quantification of matrix cracks in carbon fiber composite laminates in the absence and presence of voids controlled by the cure cycle. *Composites Part B: Engineering*, 154: 138–147, 2018. → page 2

[10] Chen Song Dong and Tze Chiun Tsai. Formation of resin-rich zones in composites processing. In *Advanced Materials Research*, volume 123, pages 543–546. Trans Tech Publ, 2010. → pages 3, 35

[11] Scott R White and HT Hahn. Cure cycle optimization for the reduction of processing-induced residual stresses in composite materials. *Journal of Composite Materials*, 27(14):1352–1378, 1993. → pages 3, 35

[12] Andrew L Stewart and Anoush Poursartip. Characterization of fibre alignment in as-received aerospace grade unidirectional prepreg. *Composites Part A: Applied Science and Manufacturing*, 112:239–249, 2018. → page 5

[13] Autar K Kaw. *Mechanics of composite materials*. CRC press, 2005. → page 5

[14] Leyla Farhang. *Void evolution during processing of out-of-autoclave prepreg laminates*. PhD thesis, University of British Columbia, 2014. → pages 6, 11, 52, 70, 82, 85

[15] Timotei Centea, Lessa K Grunenfelder, and Steven R Nutt. A review of out-of-autoclave prepregs–Material properties, process phenomena, and manufacturing considerations. *Composites Part A: Applied Science and Manufacturing*, 70:132–154, 2015. → page 15

[16] T Centea and P Hubert. Measuring the impregnation of an out-of-autoclave prepreg by micro-CT. *Composites Science and Technology*, 71(5):593–599, 2011. → page 6

[17] Pascal Hubert and Anoush Poursartip. A review of flow and compaction modelling relevant to thermoset matrix laminate processing. *Journal of Reinforced Plastics and Composites*, 17 (4):286–318, 1998. → pages 6, 25, 82, 85

[18] Sina Amini Niaki, Alireza Forghani, Reza Vaziri, and Anoush Poursartip. An Orthotropic Integrated Flow-Stress Model for Process Simulation of Composite Materials Part II: Three-Phase Systems. *Journal of Manufacturing Science and Engineering*, 141(3):31011, 2019. → pages 6, 83

[19] LW Jelinski, JJ Dumais, AL Cholli, TS Ellis, and FE Karasz. Nature of the water-epoxy interaction. *Macromolecules*, 18(6):1091–1095, 1985. → pages 7, 11

[20] Martin Roy. Porosity in configured structures: effect of ply drops and caul sheets in the processing of composite parts. Master's thesis, The University of British Columbia, 2015. → pages 7, 15

[21] A Shahkarami and D Van Ee. Material characterization for processing: ACG MTM45-1. Technical report, National center for advanced materials performance (NCAMP), Vancouver, Canada, 2009. → pages 7, 52, 84, 88

[22] RAVEN v3.7.4. Convergent manufacturing technologies, 2013. URL http://www.convergent.ca/products/raven-simulationsoftware. → pages xiii, xix, 7, 8, 52, 55, 84, 85, 98, 99, 109

[23] J L Kardos, M P Duduković, and R Dave. Void growth and resin transport during processing of thermosetting-matrix composites. In *Epoxy resins and composites IV*, pages 101–123. Springer, 1986. → pages 8, 11, 12, 44

[24] John J Gangloff Jr, Wook R Hwang, and Suresh G Advani. Characterization of bubble mobility in channel flow with fibrous porous media walls. *International Journal of Multiphase Flow*, 60:76–86, 2014. → pages 9, 15, 18

[25] James Kay. *Gas transport and void evolution in composite prepregs*. PhD thesis, The University of British Columbia, 2017. → pages xiii, 9, 11, 12, 16, 17, 18, 21, 44, 70, 78, 85, 88

[26] R Byron Bird, Warren E Stewart, and Edwin N Lightfoot. *Transport phenomena*. John Wiley & Sons, second edition, 2007. → page 9

[27] Navid Zobeiry, Alireza Forghani, Chao Li, Kamyar Gordnian, Ryan Thorpe, Reza Vaziri, Goran Fernlund, and Anoush Poursartip. Multiscale characterization and representation of composite materials during processing. *Phil. Trans. R. Soc. A*, 374(2071):20150278, 2016. → pages 9, 10

[28] MR Vanlandingham, RF Eduljee, and JW Gillespie Jr. Moisture diffusion in epoxy systems. *Journal of applied polymer science*, 71(5):787–798, 1999. → pages 9, 11

[29] J R Wood and M G Bader. Modelling the behaviour of gas bubbles in an epoxy resin: Evaluating the input parameters for a diffusion model using a free-volume approach. *Journal of materials science*, 30(4):916–922, 1995. → page 9

[30] L K Grunenfelder and S R Nutt. Void formation in composite prepregs - Effect of dissolved moisture. *Composites Science and Technology*, 70(16):2304–2309, 2010. → pages 11, 15

[31] Jonathan R Wood and Michael G Bader. Void control for polymer-matrix composites (2): experimental evaluation of a diffusion model for the growth and collapse of gas bubbles. *Composites manufacturing*, 5(3):149–158, 1994. → pages 11, 15

[32] Advanced Composites Group (ACG). MTM45-1 Matrix Resin Product Data Sheet. Technical report, Advanced Composites Group (ACG), 2012. URL https://www.solvay.com/en/product/mtm45-1. → pages 11, 17, 51, 85

[33] Christopher L Soles and Albert F Yee. A discussion of the molecular mechanisms of moisture transport in epoxy resins. *Journal of Polymer Science Part B: Polymer Physics*, 38 (5):792–802, 2000. → page 11

[34] RA Brand, GG Brown, and EL McKague. Processing science of epoxy resin composites. Technical report, General Dynamics San Diego CA Convair Div, 1984. → page 11

[35] Jeremy Wells. *Behaviour of resin voids in out-of-autoclave prepreg processing*. PhD thesis, The University of British Columbia, 2015. → pages 12, 15, 44, 48, 51

[36] Paul S Epstein and Milton S Plesset. On the stability of gas bubbles in liquid-gas solutions. *The Journal of Chemical Physics*, 18(11):1505–1509, 1950. → page 12

[37] Jonathan R Wood and Michael G Bader. Void control for polymer-matrix composites (1): theoretical and experimental methods for determining the growth and collapse of gas bubbles. *Composites Manufacturing*, 5(3):139–147, 1994. → page 13

[38] Y Ledru, G Bernhart, R Piquet, F Schmidt, and L Michel. Coupled visco-mechanical and diffusion void growth modelling during composite curing. *Composites Science and Technology*, 70(15):2139–2145, 2010. → page 14

[39] A Arefmanesh and S G Advani. Diffusion-induced growth of a gas bubble in a viscoelastic fluid. *Rheologica Acta*, 30(3):274–283, 1991. → pages 14, 67

[40] Ali Arefmanesh, Suresh G Advani, and Efstathios E Michaelides. An accurate numerical solution for mass diffusion-induced bubble growth in viscous liquids containing limited dissolved gas. *International Journal of Heat and Mass Transfer*, 35(7):1711–1722, 1992. → page 14

[41] B de Parscau du Plessix, S Le Corre, F Jacquemin, P Lefebure, and V Sobotka. Improved simplified approach for the prediction of porosity growth during the curing of composites parts. *Composites Part A: Applied Science and Manufacturing*, 90:549–558, 2016. → page 14

[42] Cédric Pupin, Annie Ross, Charles Dubois, Jean-Christophe Rietsch, Nicolas Vernet, and Edu Ruiz. Formation and suppression of volatile-induced porosities in an RTM epoxy resin. *Composites Part A: Applied Science and Manufacturing*, 94:146–157, 2017. → page 15

[43] M Anders, J Lo, T Centea, and S R Nutt. Eliminating volatile-induced surface porosity during resin transfer molding of a benzoxazine/epoxy blend. *Composites Part A: Applied Science and Manufacturing*, 84:442–454, 2016. → page 15

[44] Basile de Parscau du Plessix, Frédéric Jacquemin, Patrice Lefébure, and Steven Le Corre. Characterization and modeling of the polymerization-dependent moisture absorption behavior of an epoxy-carbon fiber-reinforced composite material. *Journal of Composite Materials*, 50(18):2495–2505, 2016. → page 16

[45] K Hsiao, J Kay, and G Fernlund. Gas transport and water evaporation in out-of-autoclave prepregs. In *The 26th annual technical conference of the American Society for Composites/The 2nd Joint US-Canada conference on composites*, 2011. → pages 16, 70

[46] J Kay, L Fahrang, K Hsiao, and G Fernlund. Effect of process conditions on porosity in out-of-autoclave prepreg laminates. In *18th International conference on composite materials, the korean society of composite materials*, pages 21–26, Jeju Island, Korea, 2011. → page 16

[47] C Ridgard. Process Selection and Optimization for Out-of-Autoclave Prepreg Structures. In *Society for the Advancement of Material and Process Engineering (SAMPE)*, pages 7–15, Long Beach, California, USA, 2016. → pages 16, 24

[48] C Ridgard. Out of autoclave composite technology for aerospace, defense and space structures. In *Society for the Advancement of Material and Process Engineering (SAMPE)*, Baltimore, MD, USA, 2009. → page 16

[49] T Staffan Lundström. Bubble transport through constricted capillary tubes with application to resin transfer molding. *Polymer Composites*, 17(6):770–779, 1996. → pages 18, 19

[50] L Farhang and G Fernlund. Void evolution and gas transport during cure in out-of-autoclave prepreg laminates. In *The society for the advancement of materials and process engineering (SAMPE)*, Long Beach, California, USA, 2011. → pages 19, 51, 78

[51] John J Gangloff Jr, Claire Daniel, and Suresh G Advani. A model of two-phase resin and void flow during composites processing. *International Journal of Multiphase Flow*, 65: 51–60, 2014. → page 19

[52] Chung Hae Park and Lee Woo. Modeling void formation and unsaturated flow in liquid composite molding processes: a survey and review. *Journal of reinforced plastics and composites*, 30(11):957–977, 2011. → pages 19, 20, 22

[53] Henry Darcy. *Les fontaines publiques de la ville de Dijon: exposition et application...* Victor Dalmont, 1856. → page 19

[54] Fuping Zhou, Nina Kuentzer, Pavel Simacek, Suresh G Advani, and Shawn Walsh. Analytic characterization of the permeability of dual-scale fibrous porous media. *Composites Science and Technology*, 66(15):2795–2803, 2006. → pages 19, 22

[55] Timothy G Gutowski, Tadahiko Morigaki, and Zhong Cai. The consolidation of laminate composites. *Journal of Composite Materials*, 21(2):172–188, 1987. → page 83

[56] B Rikard Gebart. Permeability of unidirectional reinforcements for RTM. *Journal of composite materials*, 26(8):1100–1133, 1992. → pages 19, 83

[57] B M Louis, K Hsiao, and G Fernlund. Gas permeability measurements of out of autoclave prepreg MTM45-1/CF2426A. In *The society for the advancement of materials and process engineering (SAMPE)*, pages 1–16, Long Seattle, WA, USA, 2010. → pages 19, 21, 85

[58] James Kratz and Pascal Hubert. Anisotropic air permeability in out-of-autoclave prepregs : Effect on honeycomb panel evacuation prior to cure. *Composites Part A*, 49:179–191, 2013.

[59] V Michaud, R Törnqvist, and J-AE Månson. Impregnation of compressible fiber mats with a thermoplastic resin. Part II: Experiments. *Journal of Composite Materials*, 35(13): 1174–1200, 2001. → page 19

[60] S Sequeira Tavares, V Michaud, and J E Månson. Through thickness air permeability of prepregs during cure. *Composites Part A*, 40(10):1587–1596, 2009. → page 19

[61] A R A Arafath, G Fernlund, and A Poursartip. Gas transport in prepregs: model and permeability experiments. In *Proceedings of International Conference on Composite Materials*, 2009. → pages 19, 25, 70, 90

[62] Clifford K Ho and Stephen W Webb. *Gas transport in porous media*, volume 20. Springer, 2006. → pages 20, 21

[63] L J Klinkenberg. The permeability of porous media to liquids and gases. In *Drilling and production practice*. American Petroleum Institute, 1941. → pages 20, 80

[64] JG Heid, JJ McMahon, RF Nielsen, ST Yuster, et al. Study of the permeability of rocks to homogeneous fluids. In *Drilling and production practice*. American Petroleum Institute, 1950. → page 21

[65] Thomas A Cender, Pavel Simacek, Steven Davis, and Suresh G Advani. Gas evacuation from partially saturated woven fiber laminates. *Transport in Porous Media*, 115(3):541–562, 2016. → pages 21, 24

[66] S Majid Hassanizadeh and William G Gray. High velocity flow in porous media. *Transport in porous media*, 2(6):521–531, 1987. → page 21

[67] Véronique Michaud. A review of non-saturated resin flow in liquid composite moulding processes. *Transport in porous media*, 115(3):581–601, 2016. → page 22

[68] R Helmus, R Hinterhölzl, and P Hubert. A stochastic approach to model material variation determining tow impregnation in out-of-autoclave prepreg consolidation. *Composites Part A: Applied Science and Manufacturing*, 77:293–300, 2015.

[69] S Thomas, C Bongiovanni, and S R Nutt. In situ estimation of through-thickness resin flow using ultrasound. *Composites Science and Technology*, 68(15-16):3093–3098, 2008. → page 22

[70] Navid Zobeiry and Caitlin Duffner. Measuring the Negative Pressure during Processing of Advanced Composites. *Composite Structures*, 203:11–17, 2018. → page 22

[71] A Mortensen and T Wong. Infiltration of fibrous preforms by a pure metal: Part III. Capillary phenomena. *Metallurgical transactions A*, 21(8):2257–2263, 1990. → page 22

[72] J Verrey, V Michaud, and J-AE Månson. Dynamic capillary effects in liquid composite moulding with non-crimp fabrics. *Composites Part A: Applied Science and Manufacturing*, 37(1):92–102, 2006. → pages 22, 85

[73] V Michaud and A Mortensen. Infiltration processing of fibre reinforced composites: governing phenomena. *Composites Part A: applied science and manufacturing*, 32(8): 981–996, 2001. → page 22

[74] Nina Kuentzer, Pavel Simacek, Suresh G. Advani, and Shawn Walsh. Permeability characterization of dual scale fibrous porous media. *Composites Part A: Applied Science and Manufacturing*, 37(11):2057–2068, 2006. → page 22

[75] Baiju Z Babu and Krishna M Pillai. Experimental investigation of the effect of fiber-mat architecture on the unsaturated flow in liquid composite molding. *Journal of Composite Materials*, 38(1):57–79, 2004. → page 23

[76] Krishna M Pillai. Modeling the unsaturated flow in liquid composite molding processes: a review and some thoughts. *Journal of Composite materials*, 38(23):2097–2118, 2004. → pages 23, 28

[77] Yung-Tin Chen, Christopher W Macosko, and H Ted Davis. Wetting of fiber mats for composites manufacturing: II. Air entrapment model. *AIChE Journal*, 41(10):2274–2281, 1995. → page 23

[78] V Rohatgi, N Patel, and L James Lee. Experimental investigation of flow-induced microvoids during impregnation of unidirectional stitched fiberglass mat. *Polymer Composites*, 17(2):161–170, 1996. → page 23

[79] Anant D Mahale, Robert K Prud'Homme, and Ludwig Rebenfeld. Quantitative measurement of voids formed during liquid impregnation of nonwoven multifilament glass networks using an optical visualization technique. *Polymer Engineering & Science*, 32(5): 319–326, 1992. → page 23

[80] Moon Koo Kang, Woo Il Lee, and H Thomas Hahn. Formation of microvoids during resin-transfer molding process. *Composites Science and Technology*, 60(12-13):2427–2434, 2000.

[81] N Patel and L.J. Lee. Modeling of void formation and removal in liquid composite molding. Part II: Model development and implementation. *Polymer Composites*, 17(1):104–114, 1996. → page 23

[82] Jeffrey M Lawrence, Valentin Neacsu, and Suresh G Advani. Modeling the impact of capillary pressure and air entrapment on fiber tow saturation during resin infusion in LCM. *Composites Part A: Applied Science and Manufacturing*, 40(8):1053–1064, 2009. → page 24

[83] Michael Yeager, Pavel Simacek, and Suresh G Advani. Role of fiber distribution and air evacuation time on capillary driven flow into fiber tows. *Composites Part A: Applied Science and Manufacturing*, 93:144–152, 2017. → page 24

[84] Rhena Helmus, Timotei Centea, Pascal Hubert, and Roland Hinterhölzl. Out-of-autoclave prepreg consolidation: Coupled air evacuation and prepreg impregnation modeling. *Journal of Composite Materials*, 50(10):1403–1413, 2016. → pages 25, 26

[85] Sina Amini Niaki, Alireza Forghani, Reza Vaziri, and Anoush Poursartip. A two-phase integrated flow-stress process model for composites with application to highly compressible phases. *Mechanics of Materials*, 109:51–66, 2017. → page 25

[86] V Michaud and J-AE Månson. Impregnation of compressible fiber mats with a thermoplastic resin. Part I: theory. *Journal of composite materials*, 35(13):1150–1173, 2001. → page 25

[87] Theodosia Kourkoutsaki, Sébastien Comas-Cardona, Christophe Binetruy, R K Upadhyay, and R Hinterhoelzl. The impact of air evacuation on the impregnation time of Out-of-Autoclave prepregs. *Composites Part A: Applied Science and Manufacturing*, 79: 30–42, 2015. → pages xiii, 26, 27, 28, 82

[88] F Y C Boey and S W Lye. Void reduction in autoclave processing of thermoset composites: Part 1: High pressure effects on void reduction. *Composites*, 23(4):261–265, 1992. → page 27

[89] T Centea and P Hubert. Out-of-autoclave prepreg consolidation under deficient pressure conditions. *Journal of Composite Materials*, 48(16):2033–2045, 2014. → page 27

[90] M Honarpour, L Koederitz, and A H Harvey. Relative Permeability of Petroleum Reservoirs CRC Press. *Inc. Boca Raton, Florida*, 1986. → page 27

[91] Jacob Bear. *Dynamics of fluids in porous media*. Courier Corporation, 2013. → pages 27, 78

[92] Hossein M. Shodja and Joseph R. Feldkamp. Analysis of two-phase flow of compressible immiscible fluids through nondeformable porous media using moving finite elements. *Transport in Porous Media*, 10(3):203–219, 1993. → pages 28, 29

[93] N Zobeiry and A Poursartip. The origins of residual stress and its evaluation in composite materials. In P.W.R. Beaumont, S. Soutis, and A. Hodzic, editors, *Structural integrity and durability of advanced composites*, pages 43–72. Woodhead Publishing, 2015. → pages xiv, 30, 33, 35

[94] Ryan J Thorpe. Experimental characterization of the viscoelastic behavior of a curing epoxy matrix composite from pre-gelation to full cure. Master's thesis, The University of British Columbia, 2013. → pages xiv, 30, 31, 99

[95] Yasir Nawab, Pascal Casari, Nicolas Boyard, and Frédéric Jacquemin. Characterization of the cure shrinkage, reaction kinetics, bulk modulus and thermal conductivity of thermoset resin from a single experiment. *Journal of Materials Science*, 48(6):2394–2403, 2013. → pages xiv, 30, 31

[96] Ryusuke Kono. The dynamic bulk viscosity of polystyrene and polymethyl methacrylate. *Journal of the Physical Society of Japan*, 15(4):718–725, 1960. → page 30

[97] Dao-Guo Yang, Kaspar M B Jansen, Leo J Ernst, G Q Zhang, H J L Bressers, and J H J Janssen. Effect of filler concentration of rubbery shear and bulk modulus of molding compounds. *Microelectronics reliability*, 47(2-3):233–239, 2007.

[98] Albert M Lindrose. Ultrasonic wave and moduli changes in a curing epoxy resin. *Experimental Mechanics*, 18(6):227–232, 1978.

[99] A R Plepys and R J Farris. Evolution of residual stresses in three-dimensionally constrained epoxy resins. *Polymer*, 31(10):1932–1936, 1990. → pages 30, 39, 40

[100] Nuri Ersoy, Tomasz Garstka, Kevin Potter, Michael R Wisnom, David Porter, Martin Clegg, and Graeme Stringer. Development of the properties of a carbon fibre reinforced thermosetting composite through cure. *Composites Part A: Applied Science and Manufacturing*, 41(3):401–409, 2010. → page 32

[101] Graham Twigg, Anoush Poursartip, and Göran Fernlund. An experimental method for quantifying tool–part shear interaction during composites processing. *Composites Science and Technology*, 63(13):1985–2002, 2003. → page 32

[102] G Fernlund, N Rahman, R Courdji, M Bresslauer, A Poursartip, K Willden, and K Nelson. Experimental and numerical study of the effect of cure cycle, tool surface, geometry, and lay-up on the dimensional fidelity of autoclave-processed composite parts. *Composites part A: applied science and manufacturing*, 33(3):341–351, 2002. → page 32

[103] Christophe Mobuchon and Anoush Poursartip. Linear dependences of the cure shrinkage and thermal expansion of thermoset polymers on degree of cure. *To be submitted*, 2019. → pages 32, 34, 102

[104] Paul J Flory. *Principles of polymer chemistry*. Cornell University Press, 1953. → page 33

[105] Yasir Nawab, Xavier Tardif, Nicolas Boyard, Vincent Sobotka, Pascal Casari, and Frédéric Jacquemin. Determination and modelling of the cure shrinkage of epoxy vinylester resin and associated composites by considering thermal gradients. *Composites Science and Technology*, 73:81–87, 2012. → page 33

[106] Marco Holst, Katharina Schänzlin, Mirko Wenzel, Jianjun Xu, Dirk Lellinger, and Ingo Alig. Time-resolved method for the measurement of volume changes during polymerization. *Journal of Polymer Science Part B: Polymer Physics*, 43(17):2314–2325, 2005. → pages xiv, 34

[107] N Boyard, M Vayer, Ch Sinturel, R Erre, and D Delaunay. Modeling PVTX diagrams: Application to various blends based on unsaturated polyester: Influence of thermoplastic additive, fillers, and reinforcements. *Journal of applied polymer science*, 92(5):2976–2988, 2004. → page 34

[108] Carolyne Albert and Göran Fernlund. Spring-in and warpage of angled composite laminates. *Composites Science and Technology*, 62(14):1895–1912, 2002. → page 35

[109] K D Potter. Understanding the origins of defects and variability in composites manufacture. In *International Conference on Composite Materials (ICCM)-17*, Edinburgh, UK, 2009. → page 35

[110] T S Mesogitis, A A Skordos, and A C Long. Uncertainty in the manufacturing of fibrous thermosetting composites: A review. *Composites Part A: Applied Science and Manufacturing*, 57:67–75, 2014. → page 35

[111] Larry B Ilcewicz, Ernest F Dost, Jo Wo McCool, and D H Grande. Matrix cracking in composite laminates with resin-rich interlaminar layers. In *Composite Materials: Fatigue and Fracture (Third Volume)*. ASTM International, 1991. → page 35

[112] Chensong Dong. Model development for the formation of resin-rich zones in composites processing. *Composites Part A: Applied Science and Manufacturing*, 42(4):419–424, 2011. → page 35

[113] V N Korotkov and B A Rozenberg. Experimental and theoretical modeling of shrinkage damage formation in fiber composites. *Mechanics of composite materials*, 34(2):194–202, 1998. → page 35

[114] Mikhail Merzlyakov, Sindee L Simon, and Gregory B McKenna. Instrumented thick-walled tube method for measuring thermal pressure in fluids and isotropic stresses in thermosetting resins. *Review of scientific instruments*, 76(6):63904, 2005. → pages xiv, 36, 40

[115] Margit Harsch, József Karger-Kocsis, and Florian Herzog. Influence of cure regime on the strain development in an epoxy resin as monitored by a fiber Bragg grating sensor. *Macromolecular Materials and Engineering*, 292(4):474–483, 2007. → page 37

[116] Yoji Okabe, Shigeki Yashiro, Ryohei Tsuji, Tadahito Mizutani, and Nobuo Takeda. Effect of thermal residual stress on the reflection spectrum from fiber Bragg grating sensors embedded in CFRP laminates. *Composites Part A: Applied Science and Manufacturing*, 33 (7):991–999, 2002. → page 37

[117] Mikhail Merzlyakov, Yan Meng, Sindee L Simon, and Gregory B McKenna. Instrumented sphere method for measuring thermal pressure in fluids and isotropic stresses and reaction kinetics in thermosetting resins. *Review of scientific instruments*, 75(10):3327–3334, 2004. → page 37

[118] Yongsung Eom, Louis Boogh, Véronique Michaud, Paul Sunderland, and Jan-Anders Månson. Stress-initiated void formation during cure of a three-dimensionally constrained thermoset resin. *Polymer Engineering & Science*, 41(3):492–503, 2001. → pages xiv, 38, 39

[119] Patricia Prasatya, Gregory B McKenna, and Sindee L Simon. A viscoelastic model for predicting isotropic residual stresses in thermosetting materials: effects of processing parameters. *Journal of Composite Materials*, 35(10):826–848, 2001. → page 40

[120] Douglas Adolf and James E Martin. Calculation of stresses in crosslinking polymers. *Journal of Composite Materials*, 30(1):13–34, 1996. → page 40

[121] ASTM E104-02. Standard practice for maintaining constant relative humidity by means of aqueous solutions. Standard, The American Society for Testing and Materials, Geneva, CH, 2012. → page 52

[122] Jianxun Feng, KR Berger, and EP Douglas. Water vapor transport in liquid crystalline and non-liquid crystalline epoxies. *Journal of materials science*, 39(10):3413–3423, 2004. → page 66

[123] S Sequeira Tavares, Véronique Michaud, and J-AE Månson. Through thickness air permeability of prepregs during cure. *Composites Part A: Applied Science and Manufacturing*, 40(10):1587–1596, 2009. → page 66

[124] Dana A Powers. Interaction of water with epoxy. *Sandia Report SAND2009-4405, Albuquerque, New Mexico*, 2009. → page 66

[125] D ASTM. Standard test methods for void content of reinforced plastics. *ASTM designation D 2734-94*, pages 790–795, 2009. → page 71

[126] Peter R Ciriscioli, Qiuling Wang, and George S Springer. Autoclave curing - comparisons of model and test results. *Journal of composite materials*, 26(1):90–102, 1992. → page 85

[127] Alfred C Loos and George S Springer. Curing of epoxy matrix composites. *Journal of composite materials*, 17(2):135–169, 1983. → page 85

[128] Theodore L Bergman, Frank P Incropera, David P DeWitt, and Adrienne S Lavine. *Fundamentals of heat and mass transfer*. John Wiley & Sons, 7 edition, 2011. → page 85

[129] Rhino Epoxy. Rhino 1411 / 4111 Epoxy System for Infusion product data sheet. URL http://fiberglasssupply.com/pdf/RHL1411-4111InfusionResinTDS1.pdf. → pages 98, 104, 128

[130] KERMODE v1.2.8. Convergent manufacturing technologies, 2018. URL https://www.convergent.ca/products. → page 98

[131] E ASTM. Standard test method for linear thermal expansion of solid materials by thermomechanical analysis. *ASTM designation E 831-14*, 2014. → page 103

[132] Nima Zobeiry, Reza Vaziri, and Anoush Poursartip. Computationally efficient pseudo-viscoelastic models for evaluation of residual stresses in thermoset polymer composites during cure. *Composites Part A: Applied Science and Manufacturing*, 41(2): 247–256, 2010. → page 107

[133] Caroline A Schneider, Wayne S Rasband, and Kevin W Eliceiri. NIH Image to ImageJ: 25 years of image analysis. *Nature methods*, 9(7):671, 2012. → page 112

[134] COMPRO Simulation Software V1.15.16303. Convergent manufacturing technologies, 2018. URL https://www.convergent.ca/products/compro-simulation-software. → page 112

[135] Stephen Wellinghoff and Eric Baer. The mechanism of crazing in polystyrene. *Journal of Macromolecular Science, Part B: Physics*, 11(3):367–387, 1975. → page 120

[136] Anthony James Kinloch. Fracture behaviour of polymers. *Springer Science & Business Media*, page 147, 2013. → page 120

[137] Anthony James Kinloch. Fracture behaviour of polymers. *Springer Science & Business Media*, pages 158–164, 2013. → page 127

Appendix A

Coupled transport model implementation code

The code developed to implement the coupled transport model is included in this section. The code was used to generate the numerical results in Chapter 5. The code is written in C++ and is divided into two files. The file *prelim.h* includes the preliminary package initialization and material properties definitions. The file *coupled.cpp* includes all the functions and model implementations.

prelim.h

```
#ifndef _prelim_h_included_
#define _prelim_h_included_

#include <fstream>
#include <iostream>
#include <stdio.h>
#include <cmath>
#include <vector>
#include <cstdlib>
#include <sstream>
#include <stdlib.h>
```

```
using namespace std;

        // *** Processing parameters *** //
        // material constants needed to update the betha variable
        // units are length[m] ; viscosity[Pa.S]; permeability[m^2];
        const double size = 2.0; // Size of the laminate; unit: [m]
        const double d_time = 240.0; // debulk time [min]
        const double ac_press = 1.0; // Autoclave pressure [atm] NOTE: this pressue is
        // Vacuum pressure is set to 1.0 if AC pressure > 1.0 // applied after debulk time (d_time)
        double p_v   = 0.0; // pressrue at vacuum vavle or right boundary
        const double p_0 = 1.0; // initial pressure
        const double L  = 1.0; // dimentional length (NOTE: do not change)
        const double K_yy = 1.0e-16; // through-thickness permeability; resin transport
        const double K_xx = 3.2e-15; // in-plane permeability; resin transport
        const double mu_g = 1.81e-05; // gas (air) viscosity
        const double h  = 0.1e-03; //thickness of the fiber-bed
        const double p0  = 101320; // normal atmospheric pressure [Pa]
        const double phi0 = 0.46; // fiber-bed porosity (phi0 = 1.0 - fiber_volume_fraction)
        const double p_c = 0.00; // capillary pressure
        const double init_imp = 0.803; // initial impregnation
        const double klin = 0.1283/p_0; // this should be nondimentionalized
        // Klinkenberg constant suggested by James Kay for MTM45-1
        // impregnation coeff or betta = betta_cst / (mu_r)
        const double betta_cst = mu_g*K_yy*(L*L)/K_xx/(h*h)/phi0;
        // time-constant; dimensional_time = time-constant * tau
        const double time_cst = mu_g*(L*L)/K_xx/p0;
        // ******************************** //

        // ****** Model parameters ****** //
        const double dx  = 0.01;   // set space discritization
        const int nx  = size/dx;  // cell number
        const double t_max = 1000.;  // time limit
        const double dt  = 0.0001;  // time step
        const double p_a_0 = 1.0;   // atmospheric pressure
        // ******************************** //
```

```
        // update field variable
        void update_f(double aux_f[nx+2], const double ap_a[nx+1], const double aomega[nx+1],
        const double a_beta[nx+1], double time);
        // update flux at faces
        void update_fi(const double auxf[nx+2], double auxfi[nx+1], const double ap_a[nx+1],
        const double aomega[nx+1], const double abetta[nx+1]);
        // update cell impregnation
        void update_omega (const double aux_f[nx+2], const double ap_a[nx+1],
        double omega_aux[nx+1], const double abetta[nx+1]);
        // update impregnation coeff accor. viscosity data
        void update_beta(const double time, const double debulk_time, double abetta[nx+1],
        double data [1000][3], const int auxnumb);
        // update ghost cells
        void set_gcells (double aux[nx+2], double time);
        // Thomas solver for a tri−diagonal system
        void SolveThomas(double LHS[nx+2][3], double RHS[nx+2],
        const int iSize);
        void generate_csv(const double auxf[nx+2], const double aux_omega[nx+1],
        const double aux_res[nx+1],int s);
        // reads data from a file and stores in array;
        int read_data(double aux_data[][3]);
        // aux_data[][0]:Temp; aux_data[][1]:DOC; aux_data[][2]:viscosity
        // returns l2 error of solution convegence
        double error_anly(const double aux1[nx+2],const double aux2[nx+2]);
#endif
```

coupled.cpp

```
/** defaul format for material data file:
− every line represents 1 minute time progress
− evey row contains 4 columns:
"Time(min)" "Temperature[c]" "Degree of Cure" "Resin Viscosity (Pas)"
**/
#include "prelim.h"   // definition of all constants, global variables and functions
////////////////***** M A I N *****////////////////
int main ()
{
```

```
FILE *out2, *out3, *out4;
out2 = fopen ("Report.txt", "wt");
fprintf (out2,"%s\t\t %s\t %s\t %s\t %s\t %s\t %s \n\n","time", \
"Di−time(min)","Porosity(%)", "Average press.", "Vac.Pres(Pa)" , "Atm.Pres(Pa)"\
, "Betha_coeff", "Convergence");

out3 = fopen ("Pressure.txt", "wt");
out4 = fopen ("Porosity.txt", "wt");

double t = 0.;     // time variable
// assign and initialize global variables
double f[nx+2];  std::fill_n(f, nx+2, p_0);   // set domain variables+2 ghost cells
double p_a[nx+1]; std::fill_n(p_a, nx+1, p_a_0);  // set atmospheric pressure field
double omega[nx+1]; std::fill_n(omega, nx+1, init_imp); // impregnation coefficient
//## 1 cell is added just to count from 1 to nx
double betaa[nx+1];          // source term (squeeze flow) coefficient
// defined as vector in case spacial variation exists

//*// comment this part if material file available
//*// otherwise viscosity is set to a constant
double const_viscosity = 10000.0;
std::fill_n(betaa, nx+1, betta_cst/const_viscosity);
double data [1000][3];
int lnumb;   // records the number of lines in the input data file (equivalent to time in min)
int q =0;    // counter of step number
lnumb = read_data(data);

while (t < t_max)    /////**** IMPLICIT EULER ****/////
{
        if (int((t*time_cst)/60.) > d_time)
        {
                if (ac_press > 1.0) // if autoclave pressure (hgiher that 1 atm)
                p_v = 1.0;  // disconnect vacuum, i.e. Pv = 1 atm
                std::fill_n(p_a, nx+1, ac_press);
        }
        //*// uncomment if material file available
```

```
//*// otherwise visocisty and betha paramater remain constant
//update_beta (t,d_time,betaa,data,lnumb);
double pre_f [nx+2] = { };
for (int i=1; i < nx+1; i++) pre_f [i] = f[i]; // record previous solution for error analysis
update_f (f,p_a,omega,betaa,t);    // update field variable - advance 1 time step
update_omega (f,p_a,omega,betaa);    // updates impregnation of the cell at the current times step
// inputs are resin viscosity and pressure distribution
double phi = 0.0;       // stores average impregnation
double ave_pressure = 0.0 ;     // stores average pressure
for (int i=1; i < nx+1; i++){
        phi += omega[i]/(nx); // calcualtes the average poroisyt throughout the length of the laminate
        ave_pressure += f[i]/nx;
}

fprintf (out2,"%f\t %f\t %f\t %f\t %f\t %f\t %2.5e \n",t, \
(t*time_cst)/60., (1.-phi)*100, ave_pressure, p_v, p_a[20], betaa[20], error_anly (pre_f,f));  // Print report
t += dt ; // update time
q++;
if (q%100 == 0)
{
        fprintf (out3,"%f\t ", ((t*time_cst)/60.));
        fprintf (out4,"%f\t ", ((t*time_cst)/60.));
        double gas_resid [nx+1];
        for (int i=1; i < nx+1; i++)
        {
                double aux = f[i];
                double aux1 = (1.0- omega[i])*100;
                fprintf (out3,"%f\t ", aux);
                fprintf (out4,"%f\t ", aux1);
        }
        fprintf (out3,"\n ");
        fprintf (out4,"\n ");
}

if ((int((t * time_cst)/60.) - d_time) > lnumb){
        if (error_anly (pre_f,f) < 1.0e-8) cout << "Convergence reached ..." << endl;
```

```
                        phi=0;
                        for (int i=1; i < nx+1; i++) phi += omega[i]/(nx);
                        cout << (1-phi)*100 << endl;
                        break;
                }
        }
        double gas_resid [nx+1];
        for (int i=1; i < nx+1; i++) gas_resid[i] = (1.- omega[i])*f[i];
        generate_csv(f,omega,gas_resid,t);
        fclose (out2);
        fclose (out3);
        fclose (out4);
        return 0;
}
///////////////***** UPDATE VARIABLES IN TIME ******///////////////CCCCCC
void update_f (double aux_f[nx+2], const double ap_a[nx+1], const double aomega[nx+1],
const double a_beta[nx+1], double time)
{
        double fi[nx+1] = { };      // variable to record f flux integral
        set_gcells(aux_f,time);     // update ghost cells
        update_fi (aux_f,fi,ap_a, aomega,a_beta); // update flux intergal
        double mrhs [nx+2] ;     // b (in Ax=b) as a vector
        mrhs [0] = mrhs [nx+1] = 0.;   // impose bdc (ghost cells)
        double mlhs [nx+2][3];     // update tridiagonal matrix A (in Ax=b) as 3 vetors
        mlhs[0][1] = -1. ; mlhs[0][2] = 1.;   // impose Neumaan bdc on left bdr
        mlhs[nx+1][0] = 1.; mlhs[nx+1][1] = 1.;  // impose Dirichlet bdc on right bdr

        for (int i=1; i < nx+1; i++)
        {
                double n_term = aux_f[i]*(1.0+(klin/aux_f[i])); // non-linear term including the Klinkenberg term
                mrhs [i] = fi[i]; //### source term is added when updating flux integral
                mlhs [i][0] = -(n_term/dx/dx);
                mlhs [i][1] = ((1. - aomega[i])/dt) + (2.*n_term/dx/dx) - (a_beta[i]*(ap_a[i] - (2.*aux_f[i])+p_c)/aomega[i]);
                mlhs [i][2] = -(n_term/dx/dx);
        }
```

```
        SolveThomas(mlhs, mrhs,nx+2);    // Thomas solver
        for (int i=1; i < nx+1; i++){
                aux_f[i] += mrhs [i];
        }
}

////////////////****** UPDATE GHOST CELLS *****////////////////
void set_gcells(double aux[nx+2], double time)
{
        aux[0] = aux[1];    // left bdc = Newmann - fully-developed
        aux[nx+1] = (2.*p_v) - aux[nx];  // right bdc = Dirichlt - constant
}

////////////////****** UPDATE FLUX *****////////////////
void update_fi (const double auxf[nx+2], double auxfi[nx+1], const double ap_a[nx+1],
const double aomega[nx+1], const double abetta[nx+1])
{
        for (int i=1; i < nx+1; i++)
        {
                double upper = auxf [i+1];     // auxf is defined as constant in this function
                double lower = auxf [i-1];
                if (aomega[i+1] == 1.0) upper = auxf[i];  // impose Newmann bdc if right cell is fully-impregnated
                if (aomega[i-1] == 1.0) lower = auxf[i];  // impose Newmann bdc if left cell is fully-impregnated
                double n_term = auxf[i]*(1.0+(klin/auxf[i])); // non-linear term including the Klinkenberg term
                auxfi[i] = (n_term*((upper - 2.*auxf[i] + lower)/dx/dx))
                + (abetta[i]*auxf[i]*(ap_a[i] - auxf[i])/aomega[i]);

                if (aomega[i] == 1.0) auxfi[i] = 0.0;   // flux is equal to zero if the cell is fully-impregnated
        }
}

////////////////****** UPDATE CELL IMPREGNATION *****////////////////
void update_omega (const double aux_f[nx+2], const double ap_a[nx+1],
double omega_aux[nx+1], const double abetta[nx+1])
{
        for (int i=1; i < nx+1; i++)
```

```
        {
                omega_aux[i] += dt*abetta[i]*(ap_a[i] - aux_f[i]+p_c)/omega_aux[i];
                if (omega_aux[i] > 1.) omega_aux[i] = 1.;
        }
}

////////////////****** UPDATE IMPREGNATION COEFFICIENT *****/////////////////
void update_beta(const double time, const double debulk_time, double abetta[nx+1],
double data [1000][3], const int auxnumb)
{
        // Assumption: data in material data file
        // is recorded one line per minute, starting with the time = 0 min

        double di_t = (time * time_cst) / 60.;  // dimentional time - unit : minute
        double aux_beta = 0.0;

        if (di_t < debulk_time){ // assign room_temp viscosity (first line of the material file) if debulk is running
                aux_beta = betta_cst / data [0][2];
        }
        else{
                double aux_time = di_t - debulk_time;
                aux_beta = betta_cst / data [int(aux_time)][2];
        }
        // if simulation time exceeds recorded time in data_input file
        if (int(di_t-debulk_time) > auxnumb-1) aux_beta = betta_cst / data [auxnumb-1][2];
        std::fill_n(abetta, nx+1, aux_beta);  // assuming squeeze flow coeff is spatially constant
}

////////////////***** THOMAS SOLVER ******** /////////////////
void SolveThomas(double LHS[nx+2][3], double RHS[nx+2], const int iSize)
{
        int i;
        // This next line actually has no effect, but it -does- make clear that
        // the values in those locations have no impact.
        LHS[0][0] = LHS[iSize-1][2] = 0;
        // Forward elimination //
```

```
	for (i = 0; i < iSize-1; i++)
	{
		LHS[i][2] /= LHS[i][1];
		RHS[i] /= LHS[i][1];
		LHS[i+1][1] -= LHS[i][2]*LHS[i+1][0];
		RHS[i+1] -= LHS[i+1][0]*RHS[i];
	}
	RHS[iSize-1] /= LHS[iSize-1][1];// Last line of elimination //
	// Back-substitution //
	for (i = iSize-2; i >= 0; i--) RHS[i] -= RHS[i+1]*LHS[i][2];
}

////////////////***** OUTPU CSV FILE ********/////////////////
void generate_csv(const double auxf[nx+2], const double aux_omega[nx+1],const double aux_res[nx+1],int s)
{
	FILE *out1;
	char name[50];
	int m = 0;
	m = (int) (s);

	sprintf (name, "Results_%d.dat",m);
	out1 = fopen(name, "wt");
	for (int i = 1; i < nx+1; i++){
		fprintf (out1,"%d\t %2.10e\t %2.10e\n",i, auxf[i], aux_omega[i]);
	}
	fclose (out1);
}

////////////////***** READ DATA FORM FILE, STORE IN ARRAY ********/////////////////
int read_data(double aux_data[1000][3])
{
	ifstream data;
	data.open("data_nodebulk.txt");
	int x = 0;
	std::string line;
	while (std::getline(data, line))
```

```
        {
                istringstream ss(line);
                double a, b, c, d;
                while( ss >> a >> b >> c >>d)
                {
                        aux_data [x][0] = b;
                        aux_data [x][1] = c;
                        aux_data [x][2] = d;
                        ++x;
                }
        }
        return x;
}

////////////////***** SOLUTION CONVERGENCE – L2 ERROR ********////////////////
double error_anly(const double aux1[nx+2],const double aux2[nx+2])
{
        double l2 = 0.;
        for (int i = 1; i<nx+1; ++i)
        l2 += (aux1[i] – aux2[i])*(aux1[i] – aux2[i]);
        return sqrt(l2);
}ines (231 sloc) 9.57 KB
/** Please cite: Mohseni M, Zobeiry N, Fernlund G. Journal of Reinforced Plastics
and Composites. 2019 Jul 19:0731684419865783.**/
/** coupled gas/resin flow simulation using FVM and Implicit Euler **/
/** V3: Klinkenberg effect has been added **/

/** defaul format for material data file:
– every line represents 1 minute time progress
– evey row contains 4 columns:
"Time(min)" "Temperature[c]" "Degree of Cure" "Resin Viscosity (Pas)"
**/

#include "prelim.h"   // definition of all constants, global variables and functions

///////////////***** M A I N *****///////////////
```

```
int main ()
{
FILE *out2, *out3, *out4;
out2 = fopen ("Report.txt", "wt");
fprintf (out2,"%s\t\t %s\t %s\t %s\t %s\t %s\t %s \n\n","time", \
"Di−time(min)","Porosity(%)", "Average press.", "Vac.Pres(Pa)" , "Atm.Pres(Pa)"\
, "Betha_coeff", "Convergence");

out3 = fopen ("Pressure.txt", "wt");
out4 = fopen ("Porosity.txt", "wt");

double t = 0.;     // time variable
// assign and initialize global variables
double f[nx+2];  std::fill_n(f, nx+2, p_0);   // set domain variables+2 ghost cells
double p_a[nx+1]; std::fill_n(p_a, nx+1, p_a_0);  // set atmospheric pressure field
double omega[nx+1]; std::fill_n(omega, nx+1, init_imp); // impregnation coefficient
//## 1 cell is added just to count from 1 to nx
double betaa[nx+1];         // source term (squeeze flow) coefficient
// defined as vector in case spacial variation exists

//*// comment this part if material file available
//*// otherwise viscosity is set to a constant
double const_viscosity = 10000.0;
std::fill_n(betaa, nx+1, betta_cst/const_viscosity);



double data [1000][3];
int lnumb;   // records the number of lines in the input data file (equivalent to time in min)
int q =0;    // counter of step number
lnumb = read_data(data);

while (t < t_max)    /////**** IMPLICIT EULER ****/////
{
        if (int((t*time_cst)/60.) > d_time)
        {
                if (ac_press > 1.0) // if autoclave pressure (hgiher that 1 atm)
```

```
            p_v = 1.0;  // disconnect vacuum, i.e. Pv = 1 atm
            std::fill_n(p_a, nx+1, ac_press);
}
//*// uncomment if material file available
//*// otherwise visocisty and betha paramater remain constant
//update_beta (t,d_time,betaa,data,lnumb);
double pre_f [nx+2] = { };
for (int i=1; i < nx+1; i++) pre_f [i] = f[i]; // record previous solution for error analysis
update_f (f,p_a,omega,betaa,t);     // update field variable - advance 1 time step
update_omega (f,p_a,omega,betaa);    // updates impregnation of the cell at the current times step
// inputs are resin viscosity and pressure distribution
double phi = 0.0;        // stores average impregnation
double ave_pressure = 0.0 ;      // stores average pressure
for (int i=1; i < nx+1; i++){
            phi += omega[i]/(nx); // calcualtes the average poroisyt throughout the length of the laminate
            ave_pressure += f[i]/nx;
}

fprintf (out2,"%f\t %f\t %f\t %f\t %f\t %f\t %2.5e \n",t, \
(t*time_cst)/60., (1.-phi)*100, ave_pressure, p_v, p_a[20], betaa[20], error_anly (pre_f,f));  // Print report

t += dt ; // update time

q++;
if (q%100 == 0)
{
            fprintf (out3,"%f\t ", ((t*time_cst)/60.));
            fprintf (out4,"%f\t ", ((t*time_cst)/60.));
            double gas_resid [nx+1];
            for (int i=1; i < nx+1; i++)
            {
                        double aux = f[i];
                        double aux1 = (1.0- omega[i])*100;
                        fprintf (out3,"%f\t ", aux);
                        fprintf (out4,"%f\t ", aux1);
            }
```

```
                fprintf (out3,"\n ");
                fprintf (out4,"\n ");
        }

        if ((int((t * time_cst)/60.) − d_time) > lnumb){
                if (error_anly (pre_f,f) < 1.0e−8) cout << "Convergence reached ..." << endl;
                phi=0;
                for (int i=1; i < nx+1; i++) phi += omega[i]/(nx);
                cout << (1−phi)*100 << endl;
                break;
        }
}
double gas_resid [nx+1];
for (int i=1; i < nx+1; i++) gas_resid[i] = (1.− omega[i])*f[i];
generate_csv(f,omega,gas_resid,t);

fclose (out2);
fclose (out3);
fclose (out4);
return 0;
}

////////////////***** UPDATE VARIABLES IN TIME ******////////////////CCCCCC
void update_f (double aux_f[nx+2], const double ap_a[nx+1], const double aomega[nx+1],
const double a_beta[nx+1], double time)
{
double fi[nx+1] = { };      // variable to record f flux integral
set_gcells(aux_f,time);     // update ghost cells
update_fi (aux_f,fi,ap_a, aomega,a_beta); // update flux intergal
double mrhs [nx+2] ;     // b (in Ax=b) as a vector
mrhs [0] = mrhs [nx+1] = 0.;    // impose bdc (ghost cells)
double mlhs [nx+2][3];     // update tridiagonal matrix A (in Ax=b) as 3 vetors
mlhs[0][1] = −1. ; mlhs[0][2] = 1.;   // impose Neumaan bdc on left bdr
mlhs[nx+1][0] = 1.; mlhs[nx+1][1] = 1.;  // impose Dirichlet bdc on right bdr

for (int i=1; i < nx+1; i++)
```

```
{
        double n_term = aux_f[i]*(1.0+(klin/aux_f[i])); // non-linear term including the Klinkenberg term
        mrhs [i] = fi[i]; //### source term is added when updating flux integral
        mlhs [i][0] = -(n_term/dx/dx);
        mlhs [i][1] = ((1. - aomega[i])/dt) + (2.*n_term/dx/dx) - (a_beta[i]*(ap_a[i] - (2.*aux_f[i])+p_c)/aomega[i]);
        mlhs [i][2] = -(n_term/dx/dx);
}

SolveThomas(mlhs, mrhs,nx+2);    // Thomas solver
for (int i=1; i < nx+1; i++){
        aux_f[i] += mrhs [i];
}
}

////////////////****** UPDATE GHOST CELLS *****////////////////
void set_gcells(double aux[nx+2], double time)
{
aux[0] = aux[1];    // left bdc = Newmann - fully-developed
aux[nx+1] = (2.*p_v) - aux[nx];  // right bdc = DirichIt - constant
}

////////////////****** UPDATE FLUX *****////////////////
void update_fi (const double auxf[nx+2], double auxfi[nx+1], const double ap_a[nx+1],
const double aomega[nx+1], const double abetta[nx+1])
{
for (int i=1; i < nx+1; i++)
{
        double upper = auxf [i+1];     // auxf is defined as constant in this function
        double lower = auxf [i-1];
        if (aomega[i+1] == 1.0) upper = auxf[i];  // impose Newmann bdc if right cell is fully-impregnated
        if (aomega[i-1] == 1.0) lower = auxf[i];  // impose Newmann bdc if left cell is fully-impregnated
        double n_term = auxf[i]*(1.0+(klin/auxf[i])); // non-linear term including the Klinkenberg term
        auxfi[i] = (n_term*((upper - 2.*auxf[i] + lower)/dx/dx))
        + (abetta[i]*auxf[i]*(ap_a[i] - auxf[i])/aomega[i]);

        if (aomega[i] == 1.0) auxfi[i] = 0.0;   // flux is equal to zero if the cell is fully-impregnated
```

```
}
}

////////////////****** UPDATE CELL IMPREGNATION *****/////////////////
void update_omega (const double aux_f[nx+2], const double ap_a[nx+1],
double omega_aux[nx+1], const double abetta[nx+1])
{
for (int i=1; i < nx+1; i++)
{
        omega_aux[i] += dt*abetta[i]*(ap_a[i] - aux_f[i]+p_c)/omega_aux[i];
        if (omega_aux[i] > 1.) omega_aux[i] = 1.;
}
}

////////////////****** UPDATE IMPREGNATION COEFFICIENT *****/////////////////
void update_beta(const double time, const double debulk_time, double abetta[nx+1],
double data [1000][3], const int auxnumb)
{
// Assumption: data in material data file
// is recorded one line per minute, starting with the time = 0 min

double di_t = (time * time_cst) / 60.;  // dimentional time - unit : minute
double aux_beta = 0.0;

if (di_t < debulk_time){ // assign room_temp viscosity (first line of the material file) if debulk is running
        aux_beta = betta_cst / data [0][2];
}
else{
        double aux_time = di_t - debulk_time;
        aux_beta = betta_cst / data [int(aux_time)][2];
}
// if simulation time exceeds recorded time in data_input file
if (int(di_t-debulk_time) > auxnumb-1) aux_beta = betta_cst / data [auxnumb-1][2];
std::fill_n(abetta, nx+1, aux_beta);  // assuming squeeze flow coeff is spatially constant
}
```

```
////////////////***** THOMAS SOLVER ******** /////////////////
void SolveThomas(double LHS[nx+2][3], double RHS[nx+2], const int iSize)
{
int i;
// This next line actually has no effect, but it --does-- make clear that
// the values in those locations have no impact.
LHS[0][0] = LHS[iSize-1][2] = 0;
// Forward elimination //
for (i = 0; i < iSize-1; i++)
{
        LHS[i][2] /= LHS[i][1];
        RHS[i] /= LHS[i][1];
        LHS[i+1][1] -= LHS[i][2]*LHS[i+1][0];
        RHS[i+1] -= LHS[i+1][0]*RHS[i];
}
RHS[iSize-1] /= LHS[iSize-1][1];// Last line of elimination //
// Back-substitution //
for (i = iSize-2; i >= 0; i--) RHS[i] -= RHS[i+1]*LHS[i][2];
}

////////////////***** OUTPU CSV FILE ********/////////////////
void generate_csv(const double auxf[nx+2], const double aux_omega[nx+1],const double aux_res[nx+1],int s)
{
FILE *out1;
char name[50];
int m = 0;
m = (int) (s);

sprintf (name, "Results_%d.dat",m);
out1 = fopen(name, "wt");
for (int i = 1; i < nx+1; i++){
        fprintf (out1,"%d\t %2.10e\t %2.10e\n",i, auxf[i], aux_omega[i]);
}
fclose (out1);
}
```

```
////////////////***** READ DATA FORM FILE, STORE IN ARRAY ********//////////////////
int read_data(double aux_data[1000][3])
{
ifstream data;
data.open("data_nodebulk.txt");
int x = 0;
std::string line;
while (std::getline(data, line))
{
        istringstream ss(line);
        double a, b, c, d;
        while( ss >> a >> b >> c >>d)
        {
                aux_data [x][0] = b;
                aux_data [x][1] = c;
                aux_data [x][2] = d;
                ++x;
        }
}
return x;
}

////////////////***** SOLUTION CONVERGENCE – L2 ERROR ********//////////////////
double error_anly(const double aux1[nx+2],const double aux2[nx+2])
{
double l2 = 0.;
for (int i = 1; i<nx+1; ++i)
l2 += (aux1[i] – aux2[i])*(aux1[i] – aux2[i]);
return sqrt(l2);
}
```